Photophysical studies of conjugates of upconversion nanoparticles with aluminium phthalocyanines

A thesis submitted in fulfilment of the requirements

for the degree

Of

MASTERS OF SCIENCE

Of

RHODES UNIVERSITY

By

Zane Watkins

February 2016

Abstract

$NaYF_4$:Yb/Er/Gd upconversion nanoparticles (UCNP) were synthesised and their photoemission stabilised by embedding these nanoparticles in electrospun fibres. The photophysical behaviour of chloro aluminium tetrasulfo-phthalocyanine chloride (ClAlTSPc) was studied in the presence of UCNPs on mixing the two species in solution. The fluorescence lifetimes for UCNPs were shortened at 658 nm in the presence of ClAlTSPc when the former was embedded in fibre and suspended in a dimethyl sulfoxide solution of the latter. A clear singlet oxygen generation by ClAlTSPc through Förster resonance energy transfer (FRET) was demonstrated using a singlet oxygen quencher, 1,3-diphenylisobenzofuran. UCNP capped with amino groups were then covalently attached to chloro aluminium tetrasulphonated phthalocyanine (ClAlTSPc) and chloro aluminium tetracarboxy phthalocyanine (ClAlTCPc). The conjugates were characterized using different techniques such as infrared spectroscopy (IR), X-ray photoelectron spectroscopy (XPS) and Transmission electron microscopy (TEM). There was a decrease in fluorescence emission spectra of the UCNPs at 658 nm in the presence of the phthalocyanines. This decrease indicates an energy transfer between the donor UCNP and conjugated accepting phthalocyanine (Pc), due to FRET. Low FRET efficiencies of 18 and 21 % for ClAlTSPc and ClAlTCPc, respectively, were obtained.

Table of Contents

List of Symbols

α - Non-peripheral position

β - Peripheral position

$\boldsymbol{\beta}$ - Full width at half maximum of the diffraction peak

ε - Molar extinction coefficient

ε_S - Singlet state molar extinction

ε_T - Triplet state molar extinction

θ - Angular position

λ - Wavelength

π - Pi bonding

π* - Pi antibonding

τ_F - Fluorescence lifetime

τ_T - Triplet lifetime

Φ_F - Fluorescence quantum yield

Φ_T - Triplet quantum yield

χ^2 - Chi square statistic

ΔA_T - Change in the triplet state absorption

ΔA_S - Change in the ground singlet state absorption

A - Absorbance

d - Debye Scherrer equation

E1 - 1st energy level

E2 - Higher energy level

Eff - FRET Efficiency

F - Area under a fluorescence emission curve

G - Ground state

k - Empirical constant

M - Metal

n - Refractive index

$^3O_2$ – triplet state oxygen

$^1O_2$ – singlet state oxygen

R - Substituent

S_0 - Ground singlet state

S_1 - First excited singlet state

S_2 - Second exited singlet state

T_1 - First excited triplet state

List of Abbreviations

APTES - 3-aminopropyltriethoxysilane

ClAlTCPc - Chloro-aluminium tetra carboxy phthalocyanine

ClAlTSPc - Chloro-aluminium tetra sulfonated phthalocyanine

DMF- Dimethylformamide

DMSO - Dimethyl sulfoxide

DPBF - 1,3-diphenylisobenzofuran

EDC - N-(3-dimethylaminopropyl)-N-ethylcarbodiimide hydrochloride

Eff - FRET efficiencies

ESA - Excited state absorption

EtOH - Ethanol

ETU - Energy transfer upconversion

FRET - Förster resonance energy transfer

FT-IR - Fourier transform infrared

H_2Pc - Unmetallated phthalocyanine

HOMO - Highest occupied molecular orbital

LUMO - Lowest unoccupied molecular orbital

Ln^{3+} - Lanthanide metals

MeOH - Methanol

MPc - Metallophthalocyanine

NHS - N-hydroxysuccinimide

NIR - Near infrared light

NP - Nanoparticle

$(OH)_2SiPc$ - Silicon phthalocyanine dihydroxide

PA - Photon avalanche

PACT - Photodynamic antimicrobial chemotherapy

PBS - Phosphate buffer solution

Pc - Phthalocyanine

PCI - Photochemical internalisation

PDT - Photodynamic therapy

Ps - Photosensitizer

PS - Polystyrene

QD - Quantum Dot

Re - Rare earth

SEM - Scanning electron microscopy

SHG - Second harmonic generation

STPA - Simultaneous two-photon absorption

TCSPC - Time correlated single photon counting

TEM - Transmission electron microscopy

TEOS - Tetraethylorthosilicate

THF - Tetrahydrofuran

UC - Upconversion

UCNP - Upconversion nanoparticles

UV - Ultraviolet light

UV-Vis - Ultraviolet/visible

XPS - X-ray photoelectron spectroscopy

XRD - X-ray powder diffraction

List of Figures

List of Tables

List of Schemes

Chapter 1

1.1 Phthalocyanines

1.1.1 Introduction and general applications

Phthalocyanines (Pc), Fig. 1.1, were first reported in 1907 [1], with their characterisation after 1927 resulting in the current name [1]. This dye soon became one of the most used dyes across the globe with almost a quarter of all organic pigments being part of the Pc family [2,3]. Modification of the Pc is possible by adding groups to the outer ring of isoindole units which allow for a host of derivatives to be made [4,5]. Further modification can be done to the Pc by adding over 60 different metals or metalloids to the centre of the ring. Some Pcs are relatively easy to synthesize, and modify (although not always easy to purify) [6]. Pcs possess many sought after properties such as chemical and photostability, they are generally non-toxic, exhibit fluorescence, have long-lived triplet states, can absorb in the red, near infrared (NIR) regions and have large molecular extinction coefficients [7,8].

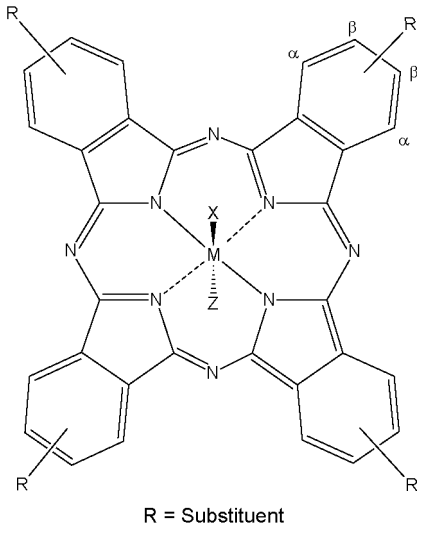

Figure 1.1: General chemical structure of metallated phthalocyanines, highlighting α and β substitution points.

These properties have seen Pcs used as light harvesters in photovoltaic applications, in fluorescence imaging, photochemical internalisation (PCI), as catalysts in redox reactions, in photodynamic antimicrobial chemotherapy (PACT), as sensors including

biosensors, for non-linear optical applications, as semiconductor materials and in photodynamic therapy (PDT) [7,9–16].

Some draw backs of Pcs are that some metal-free and metallo Pcs are insoluble in a variety of solvents and suffer from limited cell penetration depth if used as photosensitizers [17]. However these issues can be overcome by attaching peripheral substituents , Scheme 1.1, such as amino, carboxylic acid, nitro, sulfonic acid groups or others [8]. A large emphasis on the modification of phthalocyanines has seen a steady increase in the popularity of this class of compounds. Other than just peripheral structure modification, Pcs can be combined with nanomaterials such as quantum dots, nanotubes, liposomes and even dendrimers. Recently a lot of work has been done on enhancing the Pc as a photosensitizer for use in the biomedical field and cancer treatments such as photodynamic therapy. This has mainly been done through the synthesis of new Pc derivatives and by combining them with nanostructures [18].

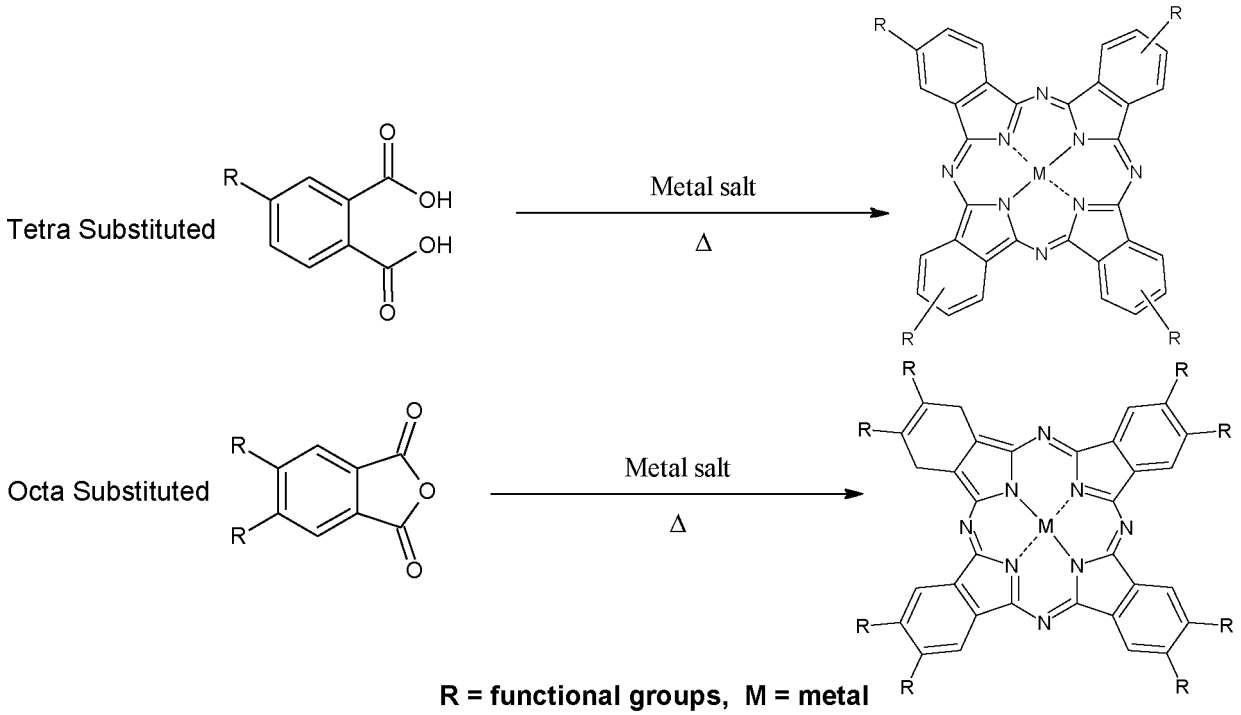

Scheme 1.1: Examples of starting materials and their resulting Pc structures.

1.1.2 Tetrasubstituted phthalocyanines

As previously mentioned Pcs have been extensively studied and in order to fully exploit their inherent properties they need to overcome their low solubility and high aggregation tendencies [19]. Tetra-substituted phthalocyanines are usually more soluble than octa substituted Pcs thanks to the formation of constitutional isomers and their ability to create a high dipole moment. The positions of the peripheral groups allow for only two types of tetra-substituted macrocycles, α or β substitutions shown in Fig. 1.1, that have different chemical and physical behaviours [19]. In this work, water soluble tetra substituted (β) Pcs are employed. These are chloro-aluminium tetra sulfonated Pc (ClAlTSPc), Fig 1.2, and chloro-aluminium tetra carboxy Pc (ClAlTCPc), whose synthesis is well known. The general synthesis of octa or tetra Pcs is shown in Scheme 1.1. The need for a water-soluble class of photosensitizers is growing, mainly due to potential biological application as mentioned earlier. The photophysical properties of sulfonated and carboxylated Pcs have been studied in biological media with promising results [20].

ClAlTSPc is employed since Photosens®, which is $ClAlPcS_{mix}$ (containing a mixture of mono, di, and tri sulfonated derivatives) is already in chemical trials [21] for PDT. It is known that the degree of sulfonation affects the lipid solubility and aggregation properties of sulfonated Pcs, both of which are known to influence cellular uptake and phototoxicity [22]. In this work a tetrasubstituted Pc is employed for linking to upconversion nanoparticles (UCNP). The sulphur substituents also have the capability of forming links with other functional groups making them very versatile.

The appeal of tetracarboxy Pcs lie in their ability to attach to other chemical groups or structures via easy covalent linkage [23–26]. ClAlTCPc was chosen due to less aggregation compared to other MTCPcs, as a result of the presence of the axial Cl ligand

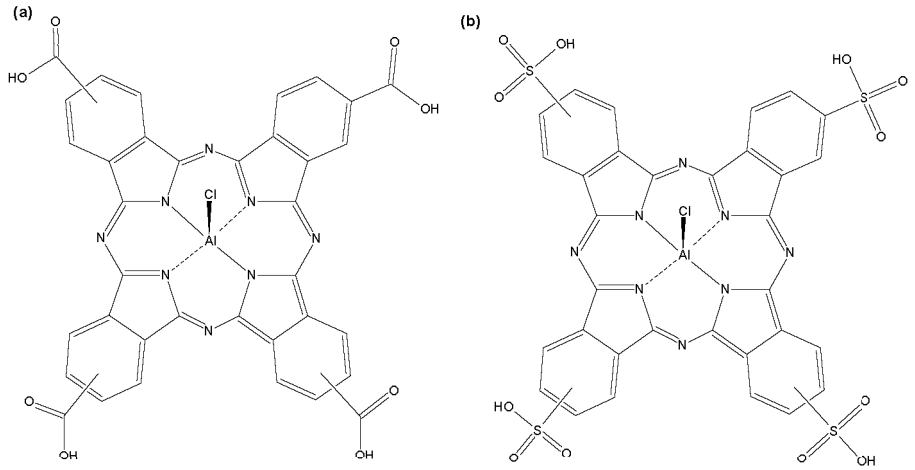

Figure 1.2: Typical chemical structures for tetra substituted (a) carboxy [25] ***and (b) sulfo Pc*** [26]**.**

1.1.3 Phthalocyanine absorption spectrum

Pcs exhibit a strong absorption band, known as the Q band, around 670 nm with variations occurring up to 1,000 nm, as well as a weaker band appearing in the UV region called the B bands, Fig 1.3. The normal unmetallated Pc, or H_2Pc, lies in one plane giving it a square planar, D_{2h} symmetry, with a split Q band, Fig 1.3. By adding a metal into the centre of the Pc's structure the symmetry increases from D_{2h} to D_{4h}, with a single Q band, Fig 1.3. As mentioned earlier attachment of various peripheral substituents can alter the tendency for aggregation, solubility, shift the Q band and alter the overall symmetry**.**

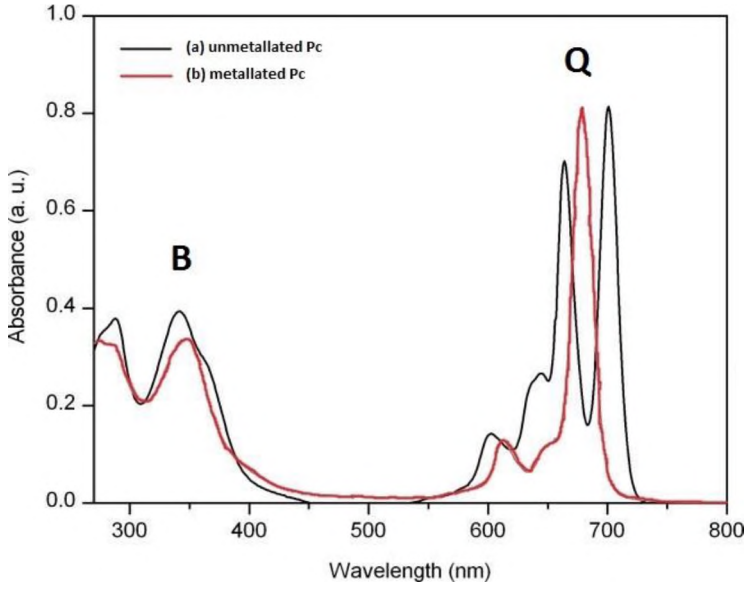

Figure 1.3: Absorption spectra for (a) an unmetallated Pc and (b) a metallated Pc [27]**.**

The Q and B bands are a result of π - π * transitions from the highest occupied molecular orbitals (HOMO) of the MPc ring to the lowest unoccupied molecular orbitals (LUMO), Fig 1.4 [27].

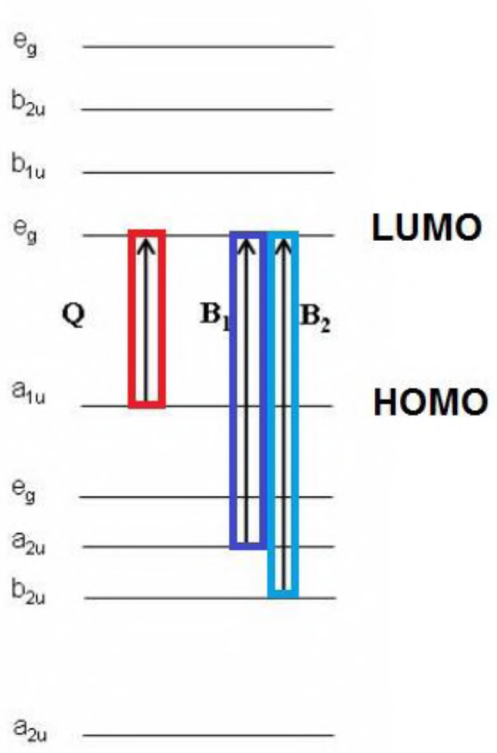

Figure 1.4: The scheme of energy levels in metallated phthalocyanines with the first two π→π* transitions [27]***.***

1.2 PDT: History and background

Photodynamic therapy, is the therapeutic use of light, which first saw scientific interest in the 1920's [28]. The promise that PDT holds is in its potential of treating many health issues, especially but not limited to cancer treatment [29,30]. New discoveries however have found PDT useful against other health issues such as immunological effects, inflammation and bacterial infections. Traditional cancer treatments have limited therapeutic effect, have their own side effects and are very often incredibly stressful and painful. These treatments include radiation, surgery and/or chemotherapy. PDT is an alternative method of treatment which may prove to be more effective and less harmful. PDT has reportedly been used for the treatment of bladder

cancers, brain cancers, breast metastases, skin cancers, gynaecological malignancies, colorectal cancers, thoracic malignancies, as well as oral, head and neck cancers [30].

There are a few conditions that need to be met in order for a photosensitizer to be considered viable for PDT. It needs to absorb in the red region of the visible spectrum, which would most likely fall within the therapeutic window, Fig 1.5 [31], should have a large molar extinction coefficient, be photostable, exhibit low dark toxicity and have rapid clearance. Phthalocyanines offer all these qualities and are therefore extensively studied as PDT agents.

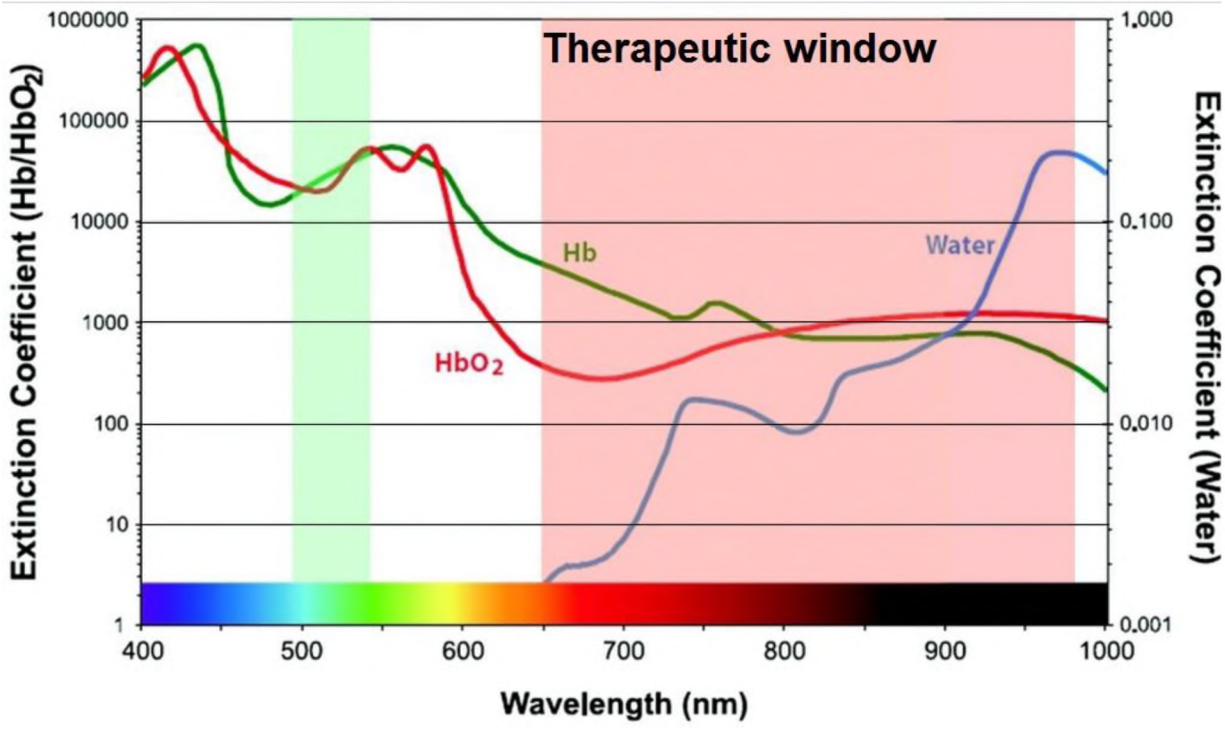

Figure 1.5: The absorbance's of different wavelengths in biological tissue, known as the biological window [31].

Three components are important for PDT, a photosensitizer (Ps), light, and oxygen [30,32]. Fig 1.6 shows the mechanism for PDT where the Ps is excited to higher energy states (S_1 or S_2). At this stage, the electron can fall back to its ground state (S_0) where we observe normal fluorescence [33]. However, generally the Ps has the

ability to undergo an electron spin conversion to its triplet state (T_1). Here it reacts directly with organic materials via electron exchange, resulting in an oxidized substrate and a reduced Ps (type I mechanism) [30]. Another process utilises a transfer of energy directly to molecular oxygen from the Ps triplet state, resulting in the formation of singlet oxygen (type II mechanism) [34].

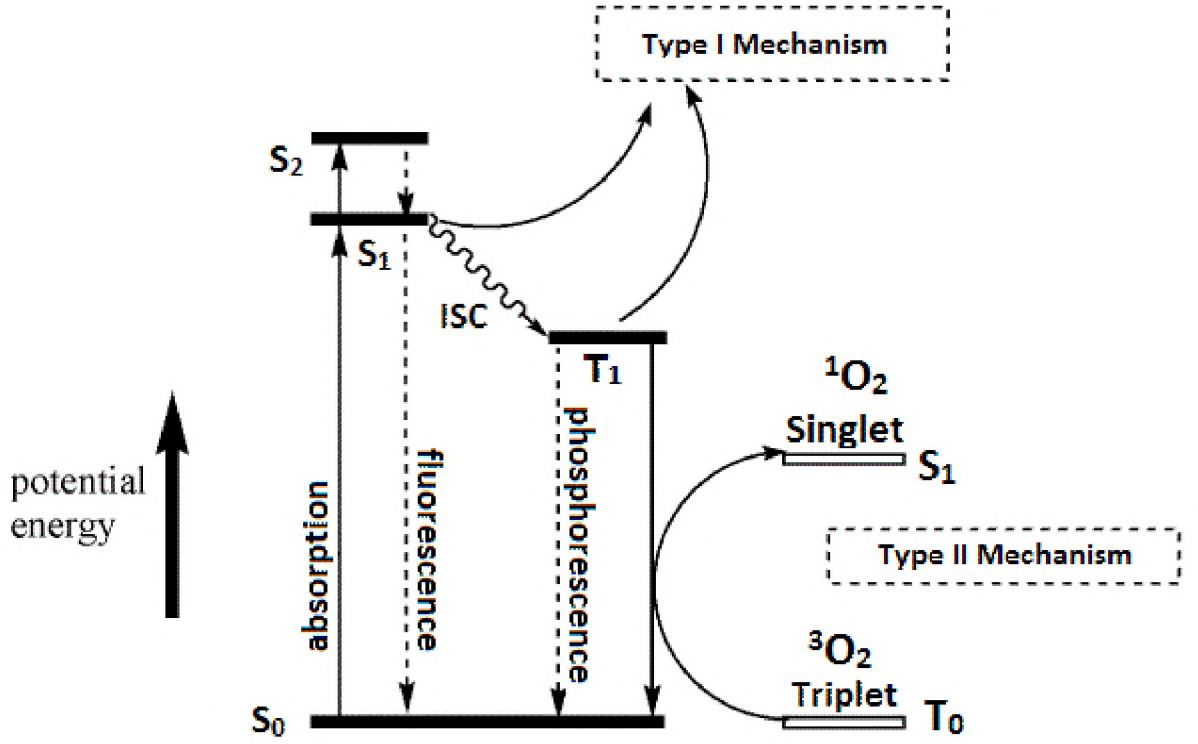

Figure 1.6: Jablonski diagram displaying the mechanism of type (I) and type (II) mechanisms.

The ideal PDT photosensitiser should absorb in the therapeutic window, 650–980 nm seen in Fig 1.5 [31], where there is deep light penetration. The Pcs in this work absorb near 670 nm. The aim of this work is to extend the absorption wavelength by linking the Pcs to UCNP which absorb at a longer wavelength (980 nm). The conjugate will be excited where UCNP absorb, resulting in energy transfer through Förster resonance energy transfer (FRET) to the Pc.

1.3 Nanoparticles

1.3.1 Introduction and General Applications

Nanoparticles can take a large range of shapes, sizes, types and origins. Simplistically nanoparticles fall into 6 classes, ceramic, metallic, carbon based, semiconductor and polymer based nanoparticles. Nanoparticles can occur naturally or be made synthetically. Liposomes are examples of nanoparticles which occur naturally [35,36]. Metallic nanoparticles are inorganic and very often synthetic nanostructures designed with specific properties for a predetermined application. Examples include iron oxide nanoparticles [35–37], magnetic NPs [35,36], carbon nanomaterials [35], quantum dots [35], and UCNP [38] (the latter are the subject of this thesis).

In the biomedical field an important area of research is that of nanoparticle targeted drug delivery. There are a number of characteristics that nanoparticles have which can affect their potential as drug delivery agents. Particle size, loading capacity and surface properties are among the most important features which dictate the effectiveness of drug delivery systems. A large segment of this area of research is dedicated to tumor targeting using nanoparticle delivery systems. A successful drug delivery system should target tumors which are localized within or on the surface of organs or organic tissues. Many anticancer drugs, even if they are located in the tumour, often have limited efficacy on solid tumours. Mainly because cancer cells are able to develop mechanisms of resistance, and activating the drug is hindered by the organic tissue [37].

1.3.2 Upconversion and Upconversion Nanoparticles

1.3.2.1 Basics

Normal fluorescence utilises visible or ultraviolet (UV) light as a sensitization source. While it is relatively common and follows Stokes shift laws this method of sensitization has some drawbacks, such as interference from auto fluorescence and scattering of various biological molecules [39]. For many reasons these characteristics are unfavourable and alternative fluorescent materials have been investigated. Lanthanide (Ln^{3+}) doped UCNPs, are some of these new materials and have seen a rise in interest due to their potentially versatile biological applications owing to their ability of converting near-infrared (NIR) light to visible light [40]. Other factors resulting in their popularity are their low background light, high detection limits for biological imaging and low toxicity which are major concerns to current fluorescent materials such as organic dyes and quantum dots [39,41]. UCNPs can be excited by using NIR light at a spectral range of 700 - 1000 nm, where the absorption coefficients of lipid, haemoglobin, and other biological components are minimal, as shown in Fig. 1.5 [31]. Water absorbs strongly in the 1000 nm region, however this region is still optimal for light to penetrate biological tissues. Upconversion (UC) luminescent nanomaterials are also employed in various optical devices such as three-dimensional flat-panel displays, solid-state lasers and low-intensity IR imaging [41,42].

So what is UC and how does it work?

Rare earth (Re) metals have similar physical and chemical properties. Of these properties, emitting through their 4f–4f intra-configurational transitions is interesting. Among the luminescent Ln^{3+} elements, a rather special phenomenon exists thanks to broad f–d transitions which are different from the usual f–f transitions [42]. Lanthanides have already been used as luminescent centres for molecular based functional materials. However, the elements like Sc^{3+}, Y^{3+}, La^{3+} and Lu^{3+} are not considered

because they lack unpaired 4f electrons. For this reason these elements are used in inorganic host materials. For the luminescent ions such as Yb^{3+}, the partially filled 4f shell is shielded by $5s^25p^6$ sub-shells. This leads to important and unique spectroscopic characteristics with less interference from the chemical micro-environment. Upconversion fluorescence typically displays narrow band emissions and long fluorescence lifetimes [39], which could result from this shielding effect.

Upconverting materials absorb low energy photons and emit higher-energy photons, Fig 1.7. The UC process is a nonlinear optical mechanism where the consecutive absorption of two or more photons result in the emission of shorter wavelength radiation. The mechanism utilises long-lived intermediate states and exhibits anti-Stokes emission [42].

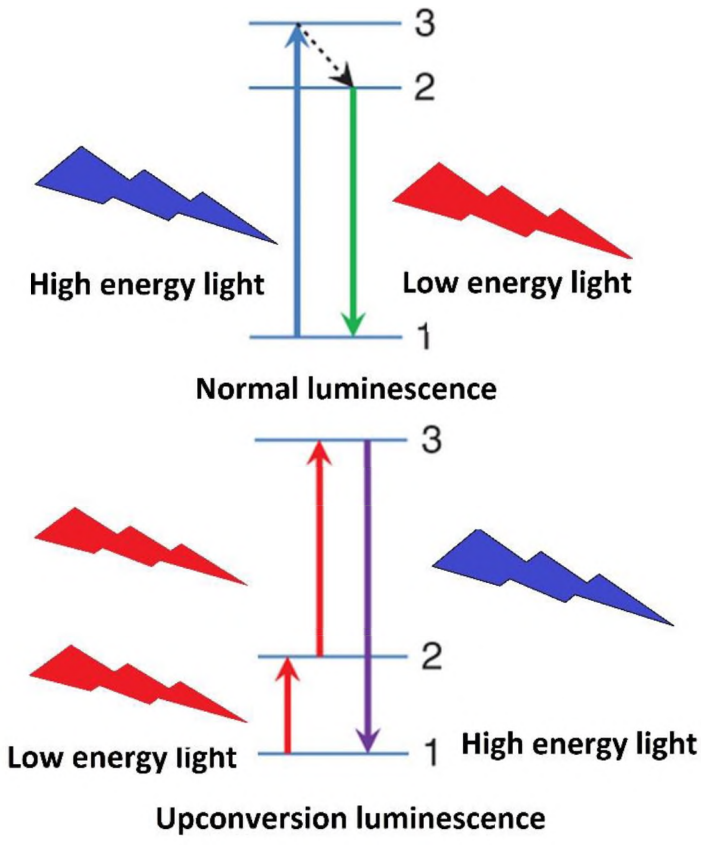

Figure 1.7: The difference between normal luminescence and upconversion luminescence

Fig. 1.8 [43] shows the energy diagrams of Ln^{3+} atoms in a $LaCl_3$ host lattice. The radiative transition between the energy levels determines which elements are selected for UC to occur. So it is pretty clear that the larger the energy level gap, from ground state to excited state, the less likely energy is nonradiatively transferred and increases excitation energy. For example, Gd^{3+} has a large energy gap between its ground state and its intermediate states, $^8S_{7/2} \rightarrow {}^6P_{7/2}$, Fig 1.8, meaning it cannot participate in any nonradiative energy transfer and requires a large amount of energy to be excited which results in it often being used as host lattice material instead of the luminescent centre [42].

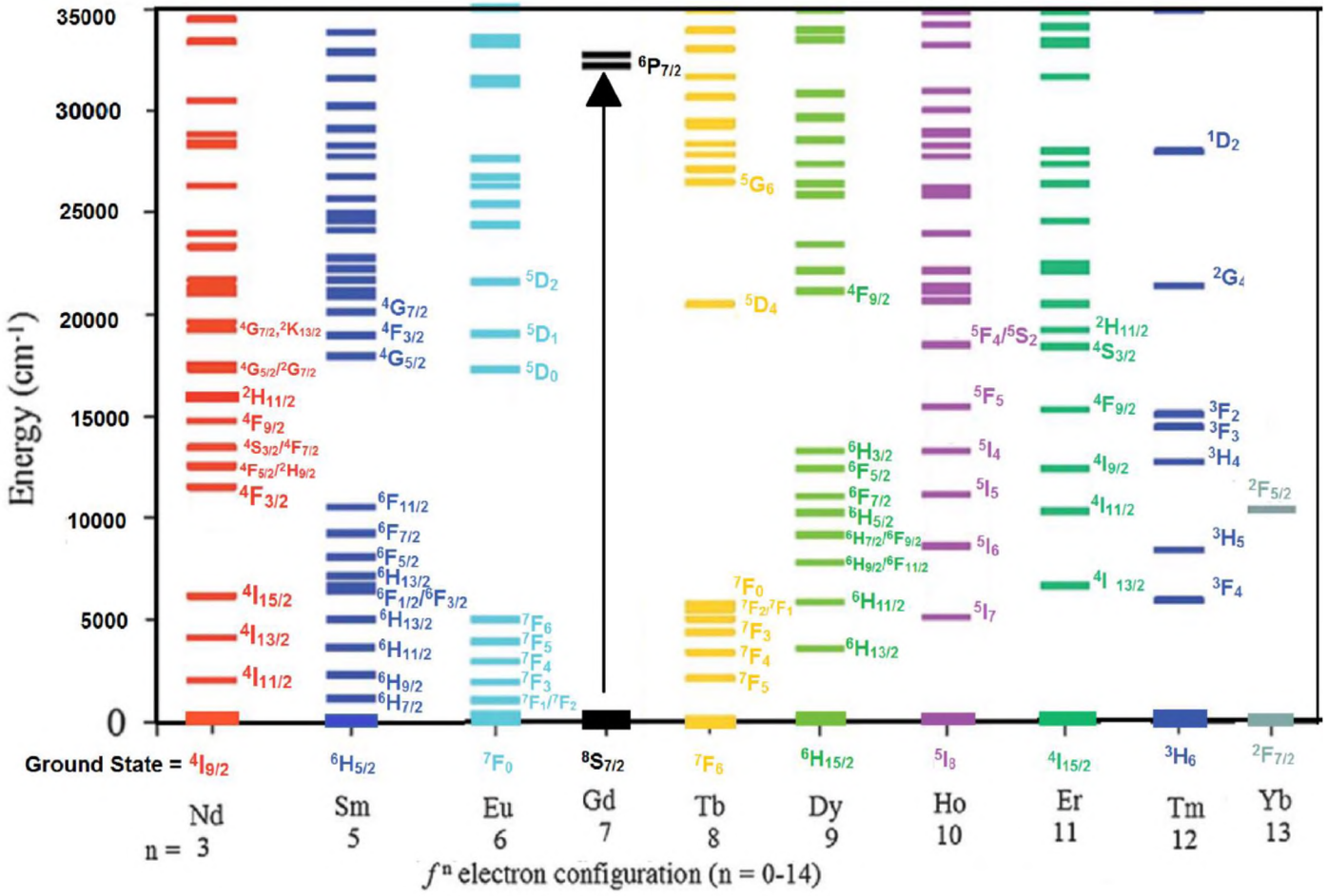

Figure 1.8: Energy diagrams for Ln^{3+} in a $LaCl_3$ lattice [43].

In contrast, the energy gaps for Sm^{3+} ($^6F_{11/2} \rightarrow {}^4G_{5/2}$), Eu^{3+} ($^7F_6 \rightarrow {}^5D_0$), Tb^{3+} ($^7F_0 \rightarrow {}^5D_4$) and Dy^{3+} ($^6H_{3/2} \rightarrow {}^4F_{9/2}$) have smaller step sizes and are thus sufficient for excitation,

however the mentioned energy levels are too far apart to facilitate the UC process using Yb^{3+}. The elements Nd^{3+} ($^4F_{3/2} \rightarrow {}^4G_{7/2}$) [44], Ho^{3+} ($^5I_6 \rightarrow {}^5F_4/{}^5S_2$) [45], Er^{3+} ($^4I_{11/2} \rightarrow {}^4S_{3/2}$) [46], and Tm^{3+} ($^3F_4 \rightarrow {}^3H_4$) [47], have on average slightly larger step sizes in their energy gaps. The energy transitions for the above mentioned elements fall within the resonance energy gap for Yb^{3+}, since the latter is the sensitizer, and this allows for visible to near infrared emissions owing to the regular energy gaps of the aforementioned transitions. Basically the elements used for upconversion have regular energy levels while have irregular energy levels as seen in Fig 1.8.

1.3.2.2 UC Mechanisms

There are 5 known anti-Stokes emission processes namely second harmonic generation (SHG), simultaneous two-photon absorption (STPA), excited state absorption (ESA), energy transfer upconversion (ETU) and photon avalanche (PA). [42], Fig 1.9.

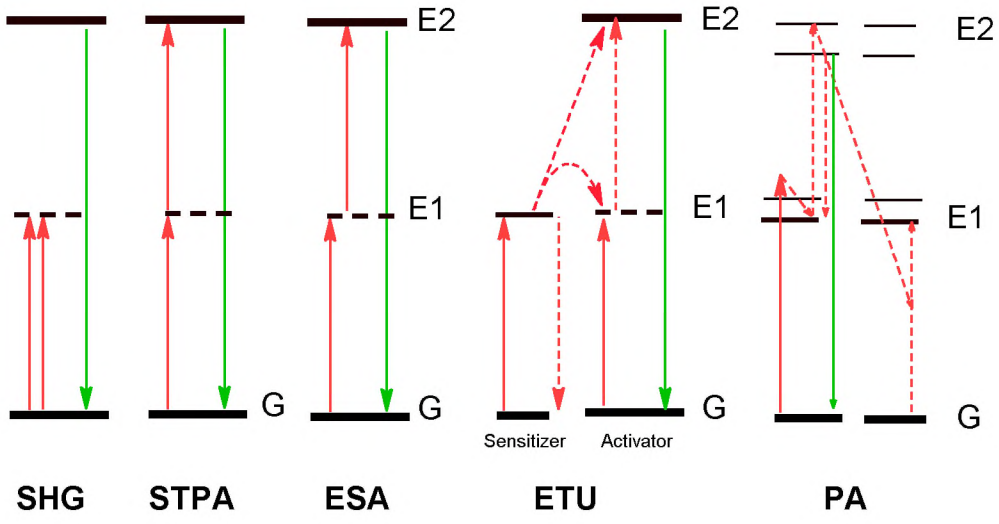

Figure 1.9: Examples of upconversion mechanisms.

The ESA process uses one atom which absorbs two photons consecutively resulting in population of higher excited state before relaxation, Fig 1.9. This is a relatively simple concept, in practice however it is not as simple. ETU is a much simpler way of

achieving UC. The ETU mechanism typically uses two luminescent centres known as the activator and sensitizer which are located in a host crystal matrix. Upon excitation with low energy photons, the sensitizer transfers its excitation energy nonradiatively to the adjacent activator, another sensitizer is excited and its energy is sequentially transferred to the already excited activator resulting in population of higher excited state. This sequential absorption and transfer may occur a number of times per sensitizer atom. Upon relaxation to the ground state the radiation emitted is of a higher energy than that of the excitation energy [42].

ETU is more commonly used in UC nanomaterials since it is easier to achieve. A very common sensitizer in ETU systems is Yb^{3+} thanks to its one and only unique excitation level of $^2F_{5/2}$, seen in Fig. 1.8. A potential activator needs ladder- like energy levels, long lived excited states and excellent resonance with the sensitizer's excited energy level. In the context of this study the sensitizer is Yb^{3+} ($^2F_{7/2}\rightarrow{}^2F_{5/2}$). Er^{3+}, Ho^{3+} and Tm^{3+} have been used as UC activators for a very long time [42]. Overall Er^{3+} shows really high UC efficiencies thanks to its similar sequential energy gaps ($^4I_{15/2}\rightarrow{}^2H_{11/2}$), ($^4I_{15/2}\rightarrow{}^4S_{3/2}$), and ($^4I_{15/2}\rightarrow{}^4F_{9/2}$), which have comparable energy, Fig 1.10 [46].

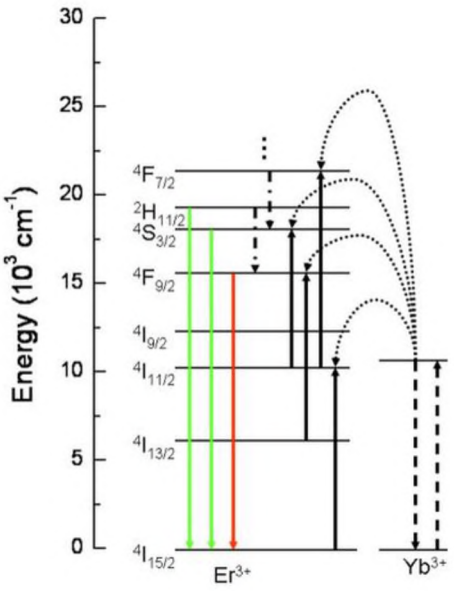

Figure 1.10: Representation of the energy transfer between the Yb^{3+} and Er^{3+} ions [46].

The host matrix is one of the most important structures impacting on the UC process. It provides the environment within in which the process can occur. However very often the host matrix interferes with the internal energy transfers and as such host matrices with low lattice phonon energies like $NaYF_4$ have proven to be optimal in providing highly efficient UC emissions [39,42]. In general there are two types of crystal lattice structural configurations, the cubic phase (α-phase) and hexagonal phase (β-phase). For the greatest UC efficiency, it is generally agreed that the β-phase, which provides a greater density of atoms, favours the emission of the Yb^{3+}, Er^{3+} dual ion activated systems [41,42]. The above mentioned systems typically display green emissions at 525 and 543 nm with red emissions at 655 nm [42] and weak blue emissions at 410 nm. Although UCNPs are simple to make, controlling their size, phase and optical properties are difficult and a challenge to reproduce or upscale [41].

1.3.3 Linking of UCNP to Pcs

UC or UCNP is not new, with the principle first expounded in 1966 [48], however only in the last 10 years have their properties really been explored. On their own they are not the most versatile of nanomaterials, however if combined with other materials a lot more possibilities open up. Conventional upconversion nanoparticles are not very soluble, or even dispersible in many solvents. This is due to the fact that normally their surface layers are usually oleate capped. This problem is easily solved by simply adding another surfactant which can be chosen for specific solvents or for further modification of the nanoparticles surface. For example in this work the normal UCNP is capped with silicon dioxide with the intention of increasing water solubility and the eventual addition of amino groups for conjugation to ClAlTCPc and ClAlTSPc.

Table 1.1: Summary of work done on linking the upconversion nanoparticle with a photosensitiser for use in PDT.

Application	UCNP coating	Ps	Link	UCNP Fluo lifetime before and after	Ref.
PDT	SiO_2	MC540	Encapsulation	n/a	[49]
PDT	PEI	ZnPc	Adsorption	n/a	[50]
Labelling	PEG	Streptavidin	Covalent	n/a	[51]
PDT	Mesoporous silica	ZnPc	Shell loading	n/a	[52]
PDT	Mesoporous silica	ZnPc	Shell loading	n/a	[53]
PDT	PEG	Ce6	Loading	n/a	[54]
PDT	PEGbCC	TPP		n/a	[55]
PDT	Mesoporous Silica	MC540	Shell loading	n/a	[56]
PDT		ZnPc		n/a	
PDT/MRI	Mesoporous silica	AlTCPc	Covalent	n/a	[57]
PDT/MRI	SiO_2	SPCD	Covalent grafting	n/a	[58]
		HP		n/a	
PDT	Chitosan	Ppa	Amide Covalent	n/a	[59]
PDT	SiO_2	MB	Water-in-oil reverse microemulsion	n/a	[60]
PDT/PTT	Core-Shell NH_2	ZnPc	Adsorption	n/a	[61]
		NGO	Covalent grafting		
PDT	α -CD.	Ce6	Adsorption	n/a	[62]
		ZnPc			
		MB			
PDT	Silica and NH_2	ZnTCPc	Amide Covalent	368 µs - 192 µs	[63]
PDT	OQPGA-PEG/RGD/TAT lipid micelles	ZnPc	Encapsulation	n/a	[64]
PDT	Bio-cellulose membranes	ClAlPc		n/a	[65]
PDT	Silica and NH_2	AlOCPc	Amide Covalent	240 µs - 220 µs	[18]
PDT	NH_2	Ce6	Covalent	84 µs - 64 µs	[66]
				218 µs - 63 µs	

a* abbreviations:

PEI - poly(ethylene imine)
α-CD - α-cyclodextrin .
SPCD - silicon phthalocyanine dihydroxide
MRI - Magnetic resonance imaging
PEGbCC - PEG-block-copolymer coatings
AlOCPc – Aluminium octacarboxy Pc
PEG - Poly(ethylene glycol)
MC540 - merocyanine 540
HP – hematoporphyrin
Ce6 - chlorin e6
MB - Methylene Blue
NGO - nanographene oxide
PTT - Photothermal therapy
TPP -tetraphenyl porphrine
Ppa - pyropheophorbide a
ZnTCPc - Zinc(II) tetracarboxy Pc
ZnPc - Zinc(II) Phthalocyanine
n/a = not applicable
OQPGA-PEG/RGD/TAT – Octadecyl-quaternized modified poly glutamic acid - grafted PEG / grafted targeting peptide (RGD) / grafted transmembrane peptide (TAT)

Numerous work has been done on bringing the UCNP into close proximity with a photosensitiser. Table 1.1 [18,49–66] shows a number of photosensitizers which have been linked to UCNPs. Only a few Pcs have been reportedly linked to UCNP.

Silicon phthalocyanine dihydroxide ($(OH)_2SiPc$) has been covalently linked to UCNPs [58]. Excitation where UCNPs absorb (980 nm) resulted in energy transfer to ($(OH)_2SiPc$) and the generation of singlet oxygen [58]. Tetrasubstituted carboxy aluminium phthalocyanine has been covalently linked to silica-coated $NaGdF_4$:Yb,Er/$NaGdF_4$ nanoparticles and applied in PDT and magnetic resonance imaging (MRI) of cancer cells. The conjugate was found to be efficient in generating cytotoxic singlet oxygen under near- infrared (NIR) light irradiation [57]. Unsubstitued ZnPc has been linked to UCNP by adsorption for PDT applications, but no data on lifetimes of UCNP and singlet oxygen generation were provided [50]. In another study AlOCPc was linked to UCNP through an amide bond [18] as is the case in this work although in our case we used ClAlTCPc. No singlet oxygen generation, essential for PDT, has been reported in literature. This thesis outlines the results of a study where the effects of UCNPs on the fluorescence and triplet state behaviour of ClAlTSPc or ClAlTCPc have been investigated for the first time. In addition, the effects of the ClAlTSPc or ClAlTCPc on the fluorescence behaviour of UCNPs are also presented. The conjugates of Pcs with UCNPs are formed via amide or sulphonamide bonds, for ClAlTCPc and ClAlTSPc, respectively.

Surface adsorption offers close proximity and a potentially high loading capacity, depending on the NP size, however in the absence of formal bonds the adsorbate may deabsorb or separate from the nanoparticle in different media. In biological environments these particles may encounter a variety chemically volatile areas, such as immune system responses or areas with varying pH. This means the two constiuents have a high chance of separation. Mesoporous shell loading operates on

a similar principle as absorption but with a greater surface area and depending on the shell composition, a localised area could protect the loaded PS [67]. This method may be more effective but it still has the same issues as the physical adsorption.

Covalent linkage, Scheme 1.2, employed in this work, offers close proximity, potential high loading capacity and a chemical bond which has a higher resistance to environmental effects and decreases the chance of separation. Covalent linking is relatively simple, the NP and Ps should normally have peripheral substituents capable of readily forming a bond, such as amino, carboxylic and sulfoxide groups which are capable of forming amide or sulphonamide bonds. Under the right circumstances these reactions are quick and have a high degree of completion.

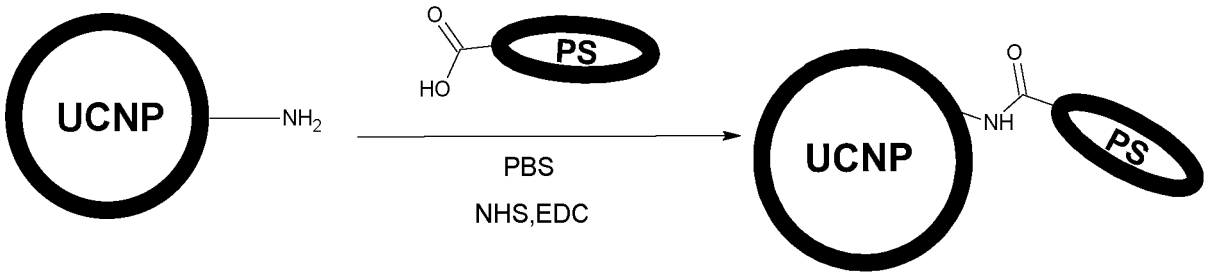

Scheme 1.2: Linking of UCNP to a PS via amide bond

1.4 Förster resonance Energy Transfer (FRET)

The theory of dipole-dipole energy transfer first came about in 1948, and was postulated by a Förster, and subsequently called Förster resonance energy transfer (FRET). FRET is a nonradiative energy transfer that occurs between a donor and acceptor which are in close proximity [68], Fig 1.11.

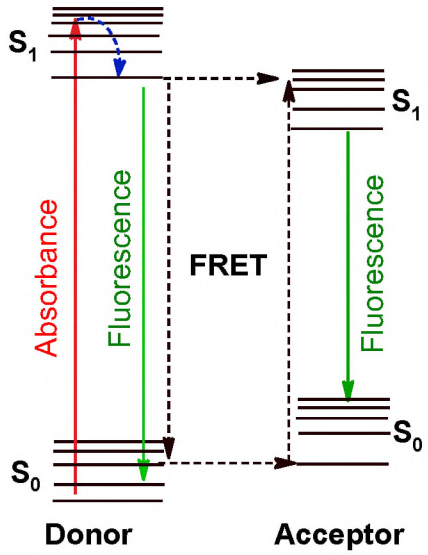

Figure 1.11: Non radiative energy transfer via FRET.

In this work the energy transfer from UCNP to Pc will be investigated, Fig 1.12. UCNP–Pc conjugates will be studied in solution and when embedded in electrospun nanofibres to be discussed next.

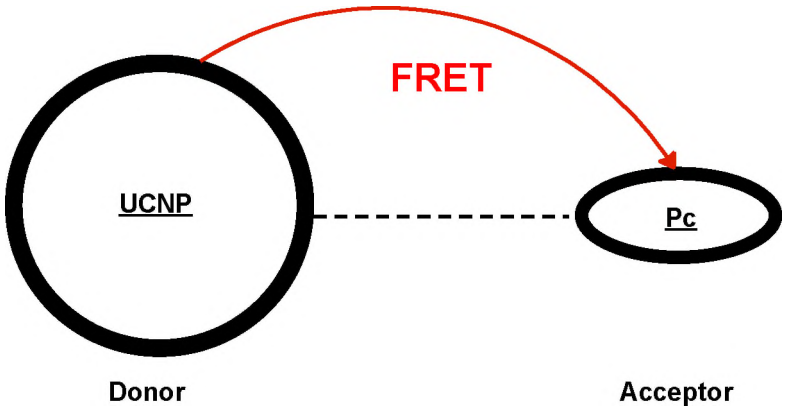

Figure 1.12: Representation of UCNP and Pc in close proximity or linked undergoing FRET.

The FRET theory states that for efficient transfer the energy donor and acceptor need to be in resonance, which in basic terms means the fluorescence emission of the donor must overlap the absorption of the acceptor, The FRET efficiencies (Eff) may be quantified from the fluorescence quantum yields or lifetimes of the donor in the

absence $\left(\boldsymbol{\Phi_{F(donor)}}\ \mathbf{or}\ \boldsymbol{\tau_{F(donor)}}\right)$ and the presence $\left(\boldsymbol{\Phi_{F(donor)}^{linked}}\ \mathbf{or}\ \boldsymbol{\tau_{F(donor)}^{linked}}\right)$ of the acceptor, respectively using Eqs. 1.1 and 1.2 [69,70]

$$\boldsymbol{Eff} = \mathbf{1} - \frac{\boldsymbol{\Phi_{F(donor)}^{linked}}}{\boldsymbol{\Phi_{F(donor)}}} \qquad \textbf{(1.1)}$$

$$\boldsymbol{Eff} = \mathbf{1} - \frac{\boldsymbol{\tau_{F(donor)}^{linked}}}{\boldsymbol{\tau_{F(donor)}}} \qquad \textbf{(1.2)}$$

where $\boldsymbol{\Phi_F}$ is the fluorescence quantum yield and $\boldsymbol{\tau_F}$ is the fluorescence lifetime of the specific fluorescence peak.

1.5 Nanofibres and Electrospinning

1.5.1 Introduction and Applications

The term nanofibre is self-explanatory, it is a fibre with at least one dimension in the nanometre, usually the diameter. There are many methods one can use to fabricate these nanostructured materials such as drawing, template synthesis, phase separation, self-assembly, and electrospinning [71], however electrospun nanofibres are among the easiest. Electrospun nanofibres have their beginning in 1934, with Formhals, when he patented a process of creating polymer filaments using electrostatic repulsions between surface charges, and that is where the term "electrospinning" derives its origin [72–74]**.** The electrospinning process is capable of creating ultrafine fibres or fibrous structures with numerous types of polymers that possess diameters from submicrons down to nanometres [71,75]. These dimensions give the nanofibres properties like large surface area, high surface-to-volume ratio and a porous structure which allow for easy functionalization [73,76]**.**

Due the simplicity and versatility of electrospinning there is a large and growing interest in this field shared by academics and industries. A large and important area of research in applications is in the biomedical field among others. These possible applications of electrospun fibres include tissue engineering, drug release, wound dressing, enzyme immobilization, implants, biotransformation, cell imaging, wound healing and drug release [76,77]

Nanofibres are not necessarily new, however their worth is in what can be achieved by combining them with other nanomaterials and newer spinning techniques, which gives access to a diverse and limitless array of devices and applications capable of solving problems in engineering, physical, chemical, material, medicinal, biological, and computer sciences [78].

1.5.2 Electrospinning technique

For electrospinning there are three components: a high voltage supply, a capillary tube with a needle of small diameter and a metal collecting screen. Two electrodes are used, one on the needle and the other attached to the collector [75]. The high voltage generates a charge at the tip of the needle. As polymer solution is pushed out the needles tip, the charge creates a jet of polymer solution, or melt, called the taylor cone, as shown in Fig. 1.13 [79] . As the charged jet of polymer is pulled towards the collecting screen, the solution in the polymer evaporates while the polymer hardens, and is subsequently collected as an interconnected, interwoven mat of nanofibres. In principle the polymer solution, at the tip, is held together by its surface tension. This creates a charge on the surface of the solution. What follows is mutual charge repulsion and the contraction of the surface charges to the counter electrode cause a force directly opposite to the surface tension [80]. When one increases the voltage, the electrostatic force overcomes the surface tension and the polymer solution is ejected as a very long and thin stream [76].

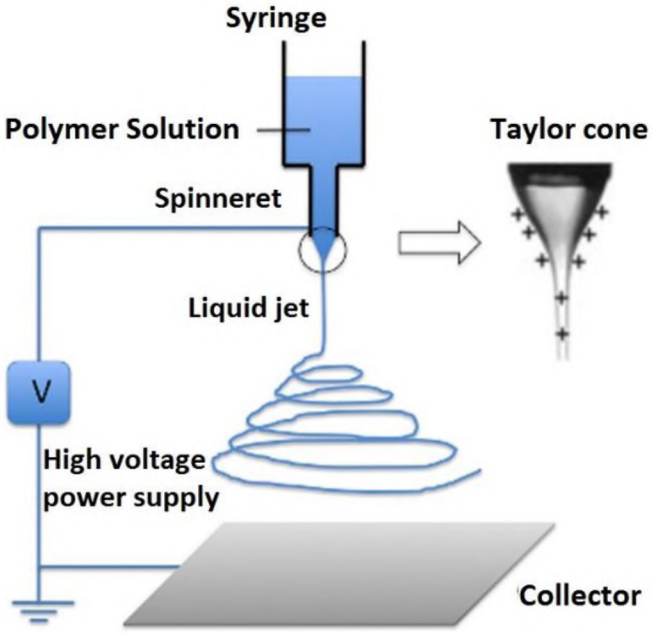

Figure 1.13: A typical electrospinning setup [79]***.***

Table 1.2: Summary of UC materials embeded in or coated with polymer structures and their applications.

UC Crystal	Application	Polymer	Medium	Ref
Er^{3+}	Academic	Lead-germanate glasses		[81]
Er^{3+}	Academic	Fluoroindate glass		[82]
LaF_3:Er^{3+}	Academic	Sol-Gel-Derived silica Thin Film		[83]
$NaYF_4$: Er^{3+}	Effects of heating	Transparent Glass ceramics		[84]
Tm^{3+}/ Yb^{3+}	UC Fibre Lasers	TeO2–$BiCl_3$ glass		[85]
La^{3+}/Yb^{3+}/Er^{3+}/F_3 NP	Academic	Silica sol-gel thin films		[86]
Er^{3+}	UC Enhancement	PbO–GeO_2 glass containing silver nanoparticles		[87]
Yb^{3+}/ Er^{3+}	UC Enhancement	PbO-GeO_2 glass containing silver nanoparticles		[88]
$NaYF_4$: Yb^{3+}/ Er^{3+} $NaYF_4$: Yb^{3+}/ Er^{3+}/Tm^{3+}	Stabilising UC luminescence	Polyvinylpyrrolidone (PVP)	Electrospun	[89]
$NaYF_4$: Yb^{3+}/Er^{3+}	Doping effects	PVP	Electrospun	[90]
Er^{3+}	UC Enhancement	Tellurite glass containing silver nanoparticles		[91]
Yb^{3+}/Er^{3+}	UC Enhancement	PbO–GeO_2 glass with silver nanoparticles		[92]
Er^{3+}/ Yb^{3+}	UC Enhancement	Bismuth-Germanate Glasses		[93]
Er^{3+}	UC Enhancement	Phosphate glasses		[94]
Er^{3+}	UC Enhancement	Sodium lead tellurite glass containing silver nanoparticles		[95]
UCNPs	Near Infrared Light Triggered Release of Bio-macromolecules	Polyacrylamide−poly(ethylene glycol) (PEG) hydrogel.		[96]
$NaYF_4$: Yb^{3+}/ Er^{3+}	Academic	Poly(methyl methacrylate) (PMMA) film	Electrospun	[97]
$NaYF_4$: Yb^{3+}/ Er^{3+}	Biomedicine	PVP	Electrospun Nanotubes	[98]
Y_2O_3: Yb^{3+}/ Er^{3+}	Academic Study	PVP then no PVP		[99]
$NaGdF_4$: Gd^{3+}/ Yb^{3+}/ Er^{3+}	Multimodal Imaging and Serum-Enhanced Gene Delivery	Poly(ethylene glycol) (PEG) and then with two layers of poly(ethylenimine) (PEI)	NPs	[100]
$NaYF_4$:Yb^{3+}/ Er^{3+} $NaYF_4$:Yb^{3+}/Tm^{3+}	Removal of colourful dye from aqueous solutions	Silica nanotubes (SNTs)	Electrospun nanotubes.	[101]
$NaGdF_4$: Yb^{3+}/Er@$NaGdF_4$:Yb@m SiO_2-PEG nanoparticles	Orthotopic cancer treatment in vivo	Poly(ε-caprolactone) (PCL)	Electrospun fibre mats	[102]

1.5.3 Doping Nanofibres with UCNPs.

Table 1.2 [81–102] gives a time line of some of the areas explored with UC and polymers. Many of the examples cited are focussed on enhancing already established mechanisms while others deal with theoretical aspects. Only recently has the focus been shifted onto applications. The biomedical field has received a lot of this attention with only one or two aimed at cancer research. It is not surprising that this has happened, especially with all the advances in nanotechnology we can finally explore this region of the nanotechnology map. The work done in this thesis exploits the ease of electrospinning polystyrene and the photophysical properties of UCNP to generate cytotoxic singlet oxygen in a solution of ClAlTSPc.

1.6 Summary and Aims

Among the sea of research involving Pcs, singlet oxygen, UCNP and electrospinning none have yet succinctly combined together and formulated a study comparing the efficacy of UCNP-Pc conjugates, via fluorescence lifetimes on the UCNP, or the viability of embedded UCNP generating singlet oxygen in a Pc solution upon irradiation by 980 nm light.

To summarize the objectives:

- To synthesise UCNPs and embed them in polystyrene nanofibres.
- Study the effect these fibres have in Pc solutions upon NIR irradiation,
- To synthesize two aluminium Pcs and link them to UCNPs and to investigate their viability for potential FRET applications.

Chapter 2

2. Experimental

2.1 Materials.

The lanthanide salts and various other salts used were purchased from Sigma Aldrich and they include: $Y(NO_2)_3{\cdot}6(H_2O)$, $ErCl_3{\cdot}6(H_2O)$, $YbCl_3{\cdot}6(H_2O)$, $GdCl_3{\cdot}6(H_2O)$, NH_4F and NaOH pellets. Sigma Aldrich also provided the Zinc phthalocyanine (ZnPc) standard, tetraethylorthosilicate (TEOS), Igepal CO-520, 1-octadecene, oleic acid, 3-aminopropyltriethoxysilane (APTES), polystyrene (PS, Mw=192,000 g/mol) and 1,3-diphenylisobenzofuran (DPBF). Solvents such as ethanol (EtOH), methanol (MeOH), toluene, thionyl chloride, dimethylformamide (DMF), tetrahydrofuran (THF), dimethyl sulfoxide (DMSO) and cyclohexane were from SAARCHEM. NaCl was purchased from MINEMA. Reidel-De Haën provided the Na_2HPO_4 and the KH_2PO_4 is from Altec Agencies. N-hydroxysuccinimide (NHS) and N-(3-dimethylaminopropyl)-N-ethylcarbodiimide hydrochloride (EDC) were from Fluka. ClAlTSPc [22] and ClAlTCPc [103] were synthesised as reported in literature.

2.2 Equipment

The thermal decomposition reactions were undertaken in a rotary regavolt temperature controlled Gallenkamp porcelain heating oven. $NaYF_4$:Yb/Er/Gd@Si@NH_2 UCNPs were washed and collected with a Merk chemicals Eppendorf Centrifuge 5810. Ground-state electronic absorption spectra were recorded on a Shimadzu, UV-Vis 2550 spectrometer, and a Cary 500 UV-Vis/ NIR spectrophotometer, for the UCNP. Excitation and emission spectra were recorded using a Varian Eclipse fluorescence spectrofluorimeter. Infra-red spectra were collected on a Perkin-Elmer Universal ATR Sampling accessory spectrum 100 FT-IR spectrometer.

Transmission electron microscopy (TEM) images were obtained using a JEOL JEM 1210 transmission electron microscope using 90 KW acceleration voltage. Scanning electron microscope (SEM) images of the fibre alone or modified with UCNPs were obtained using a JOEL JSM840 scanning electron microscope

Powder X-ray diffraction (XRD) spectra were performed on a Bruker D8 Discover diffractometer, equipped with a Lynx Eye detector, under Cu-Kα radiation (λ= 1.5405 Å). Data were collected in the range from 2θ = 10° to 90°, scanning at 0.010° min^{-1} and 192 s per step. The samples were placed on a zero background silicon wafer slide.

For time correlated single photon counting (TCSPC) studies, the $NaYF_4$:Yb/Er/Gd@Si@NH_2 UCNPs were excited at 975 nm with a diode laser (LDH-D-C-980, burst mode, 40 MHz repetition rate, PicoQuant GmbH). The detector employed was a Peltier cooled Photomultiplier (PMA-C 192-M, PicoQuant GmbH) for both fluorescence spectra and lifetime studies. For excitation of the ClAlTSPc or ClAlTCPc, the excitation source was a diode laser (LDH-P-670 driven by PDL 800-B, 670 nm, 20 MHz repetition rate, 44 ps pulse width, Picoquant GmbH).

X-ray photoelectron spectroscopy (XPS) data were collected using a Kratos Axis Ultra DLD, using an Al (monochromatic) anode, equipped with charge neutralizer. The operating pressure was kept below $5x10^{-9}$ torr. The resolution was 10 eV pass energy in the slot mode. For wide/survey XPS scans, the following parameters were used: emission current was kept at 12.5 mA and the anode (HT) voltage at 15 kV. The resolution used to acquire wide/ survey scans was at 160 eV pass energy using a hybrid lens in the slot mode. For the high resolution scans, the resolution was changed to 40 eV pass energy in the slot mode

2.3 Synthesis of $NaYF_4$:Er,Yb,Gd nanoparticles and subsequent capping

2.3.1 Uncapped $NaYF_4$:Yb/Er/Gd, Scheme 3.1

The UCNPs were synthesised as reported in literature [104] with slight modification as follows: the lanthanide salts consisting of $ErCl_3 \cdot 6(H_2O)$ (0.0061 g, 0.016 mmol), $YbCl_3 \cdot 6(H_2O)$ (0.0558 g, 0.144 mmol), $GdCl_3 \cdot 6(H_2O)$ (0.0441 g, 0.1186 mmol) and $Y(NO_2)_3 \cdot 6(H_2O)$, (0.1992 g and 0.595 mmol) were dispersed in 4 mL methanol and added to a mixture of oleic acid (6 mL) and 1-octadecene (4 mL) in a 100 mL round bottomed flask. The mixture was heated to 160 °C while stirring for 30 min. The solution was allowed to cool to room temperature. NH_4F (0.1185 g, 2.2 mmol] and NaOH (0.08 g, 2 mmol) were added to 10 mL of methanol and sonicated until fully dispersed. This mixture was then added to the solution of the metal salt and the resulting mixture stirred at room temperature for 30 min. A 70 °C heating step took place for 30 min, to remove excess solvent, and then the mixture was cooled to room temperature. The solution was then heated to 300 °C for 90 min in a GallenKamp porcelain heating oven, with the temperature being monitored with an external thermocouple. The solution was flushed with argon for 30 min, before the heating began. After 90 min heating, the solution was cooled to room temperature and then washed with ethanol (20 mL). The precipitate was collected by centrifuge for 20 min at 3000 rpm and then dried at 70 °C for 24 h. The resulting nanoparticles are termed uncapped $NaYF_4$:Yb/Er/Gd UCNPs, Scheme 3.1.

2.3.2 Silica Capped $NaYF_4$:Yb/Er/Gd@Si, Scheme 3.1

The uncapped $NaYF_4$:Yb/Er/Gd UCNPs (70 mg) prepared above, were dispersed in of cyclohexane (60 mL) in a round bottomed flask. Igepal CO-520 (1 mL), which acts as a surfactant for the facilitation of the formation of the silicon oxide layer, was added. After 5 min, a second portion of Igepal CO-520 (4 mL) and 0.92 mL of 30% ammonia were added to facilitate the capping of the nanoparticles with a silicon oxide layer. The solution was sonicated until a transparent emulsion was obtained. TEOS (400 µl) was added dropwise and then the reaction mixture was left to stir for 4 days. The silica capped nanoparticles were then precipitated out with methanol, and then washed using a 1:1 EtOH and H_2O mixture. The nanoparticles were collected by centrifugation for 20 min at 3000 rpm and left to dry. The resulting nanoparticles are represented as $NaYF_4$:Yb/Er/Gd@Si UCNPs, Scheme 3.1. The $NaYF_4$:Yb/ Er/Gd@Si UCNPs were washed with anhydrous ethanol followed by toluene.

2.3.3 Amino Capped $NaYF_4$:Yb/Er/Gd@Si@NH_2

The cleaned $NaYF_4$:Yb/Er/Gd@Si UCNPs (10 mg) were added to DMF (12 mL) and toluene (8 mL) in a 100 mL round bottomed flask and stirred for 10 min. APTES (1000 µl) was subsequently added drop-wise. The mixture was stirred for 24 h at room temperature under argon atmosphere. The particles were washed with toluene, methanol and then collected by centrifuge. The resulting nanoparticles are represented as $NaYF_4$:Yb/Er/Gd@Si@NH_2 UCNPs, Scheme 3.1.

2.4 Electrospinning

UCNPs (uncapped $NaYF_4$:Yb/Er/Gd, $NaYF_4$:Yb/Er/Gd@Si or $NaYF_4$:Yb/Er/Gd@Si@NH_2) (0.0013 g) were added to polystyrene (2.5 g) in a solvent mixture of DMF (8 mL) and THF (2 mL). The resulting solution was then stirred for 24 h at ambient temperature. After the 24 h of stirring, the solution was deposited in a syringe. The height from the tip of the needle to the collector plate was set at 11 cm with the flow rate set up at 0.03 mL/h. The voltage between the collector plate and the needle tip was set to 15 kV. The set up was left running until a uniform looking electrospun fibre matt had formed.

2.5 Synthesis of Phthalocyanine UCNP Conjugates

2.5.1 Sulphonamide bond with ClAlTSPc (Scheme 3.2)

The covalent linkage was carried out in accordance with literature [105] but with modifications. ClAlTSPc (14.0 mg, 0.016 mmol) was weighed into 25 mL round bottom flask, then DMF (3 mL) was added and the mixture was stirred in ice bath for 20 min. Thionyl chloride (6 µL, 0.021 mmol) was added drop wise to the reaction to gently activate the sulfonic acid moiety of the Pc. The reaction was left stirring at ambient temperature for 2 h, after which a solution of $NaYF_4$:Yb/Er/Gd@Si@NH_2 (3 mg in 3 mL DMF) was added and the mixture was left stirring for further 24 h leading to the formation of a secondary sulfonamide linked $NaYF_4$:Yb/Er/Gd@Si@NH_2/ClAlTSPc. The nanocomposites were precipitated out of solution by centrifugation and were successively purified with methanol to remove unreacted $NaYF_4$:Yb/Er/Gd@Si@NH_2 and ClAlTSPc because the $NaYF_4$:Yb/Er/Gd@Si@NH_2 and ClAlTSPc alone are sparingly soluble in methanol while the conjugates are not soluble.

2.5.2 Amide bond with ClAlTCPc, (Scheme 3.3)

ClAlTCPc (15 mg, 0.0167 mmol) was added to phosphate buffer solution (PBS) pH 7.2 (5 mL). EDC (0.23 g, 1.2 mmol) and NHS (0.115 g, 1 mmol) were added to activate the carboxylic groups of the ClAlTCPc. The reaction mixture was left to stir for 3 h under N_2. Then $NaYF_4$:Yb/Er/Gd@Si@NH_2 UCNPs (8.4 mg), suspended in PBS pH 7.2 (5 mL), were added to the above solution. The mixture was allowed to stir for 24 h under N_2. The obtained product was precipitated by adding ethanol and collected by centrifugation. The conjugate particles were washed once with NaOH, to remove unconjugated ClAlTCPc.

Chapter 3

The results in this dissertation have been published in the journals listed below.

1 Z. Watkins, J. Taylor, S. D'Souza, J. Britton, T. Nyokong Fluorescence behaviour and singlet oxygen production of aluminium phthalocyanine in the presence of upconversion nanoparticles J. Fluoresc. 25 (2015) 1417–1429.

2 Z. Watkins, I. Uddin, J. Britton, T. Nyokong The photophysical behaviour of conjugates of NaYF4:Yb,Er,Gd upconversion nanoparticle with aluminium phthalocyanines. Submitted.

3. Results and discussion

3.1 Synthesis and characterisation of UCNPs

The UCNPs were synthesised via the thermal decomposition method. Oleic acid was used as a stabiliser and 1-octadecence acts as a surfactant in the synthesis of the uncapped $NaYF_4$:Yb/Er/Gd UCNPs, Scheme 3.1. Upon capping with silicon oxide, TEOS was hydrolysed at the oil/water interface which is catalysed by a basic medium, in this case ammonia. The capping of silica not only stabilises the UCNP crystal structure but also makes the nanoparticle water miscible, or more soluble in most other solvents. The addition of APTES resulted in the condensation of the siloxane moiety with free amine groups attached at the end of the propyl pendant arms, after only 24 hours of stirring at room temperature to form $NaYF_4$:Yb/Er/Gd@Si@NH_2 UCNPs, this allows for the easy linking of the UCNP to other materials.

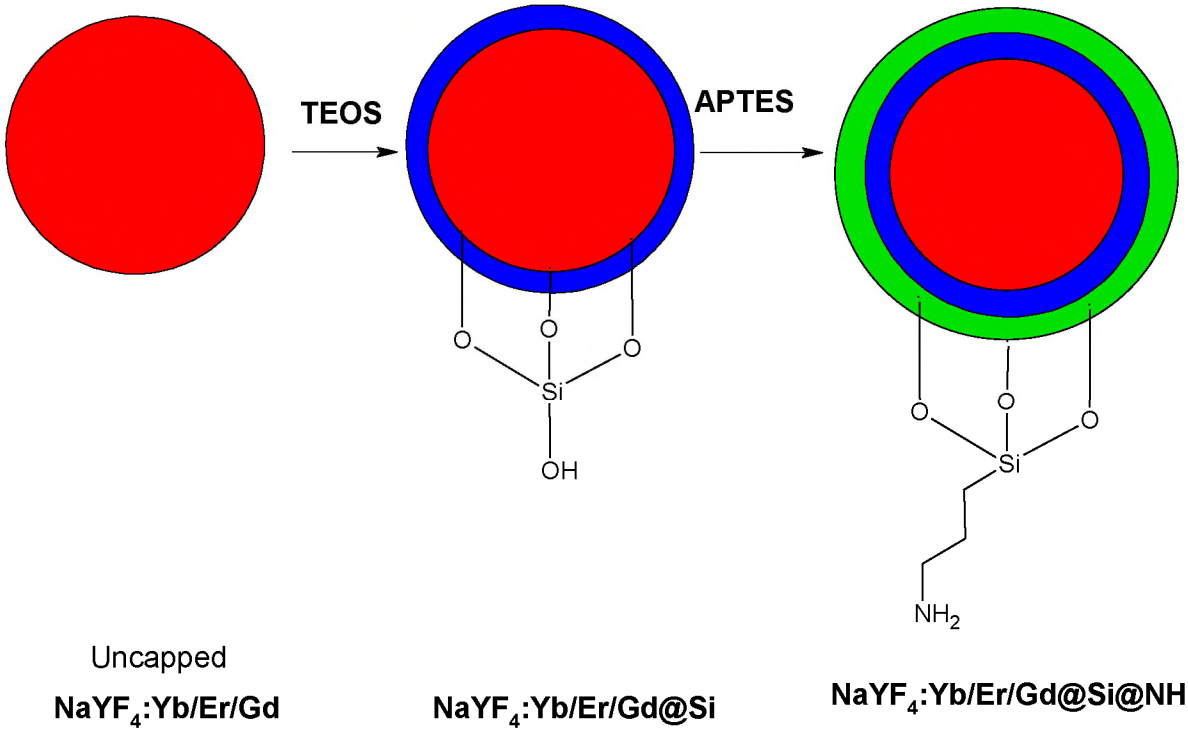

Scheme 3.1: Schematic of UCNP capping and functionalisation.

3.1.1 Transmission electron microscopy analysis.

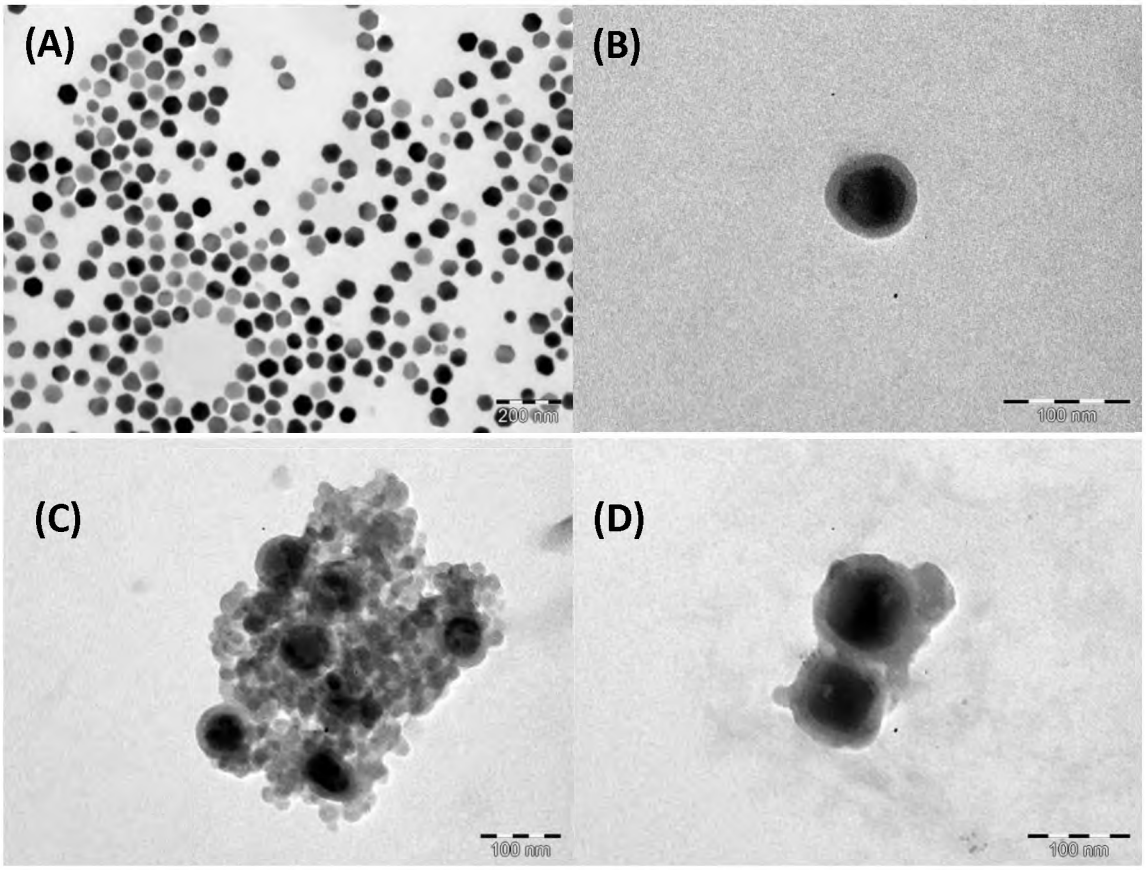

Figure 3.1: TEM images of uncapped $NaYF_4$:Yb/Er/Gd UCNPs (A), $NaYF_4$:Yb/Er/Gd@Si UCNPs (B), $NaYF_4$:Yb/Er/Gd@Si@NH_2 (C) and $NaYF_4$:Yb/Er/Gd@Si@NH_2 mixed with ClAlTSPc (D).

The TEM image of uncapped $NaYF_4$:Yb/Er/Gd nanoparticles (Fig. 3.1 (A)) shows that they are roughly 40 nm in size, monodispersed and have a uniform hexagonal disc shape. The $NaYF_4$:Yb/Er/Gd@Si particles in Fig. 3.1 (B) are clearly coated in a silica shell and exhibit monodisparity. The same cannot be said for the $NaYF_4$:Yb/Er/Gd@Si@NH_2, Fig. 3.1 (C) which show aggregation. Fig 3.1 (D) shows the TEM image of $NaYF_4$:Yb/Er/Gd@Si@NH_2 following mixing with ClAlTSPc, showing less aggregation compared to $NaYF_4$:Yb/Er/Gd@Si@NH_2 alone. The sizes for $NaYF_4$:Yb/Er/Gd@Si@NH_2 and $NaYF_4$:Yb/Er/Gd@Si were not too different from uncapped $NaYF_4$:Yb/Er/Gd.

3.1.2 XRD analysis

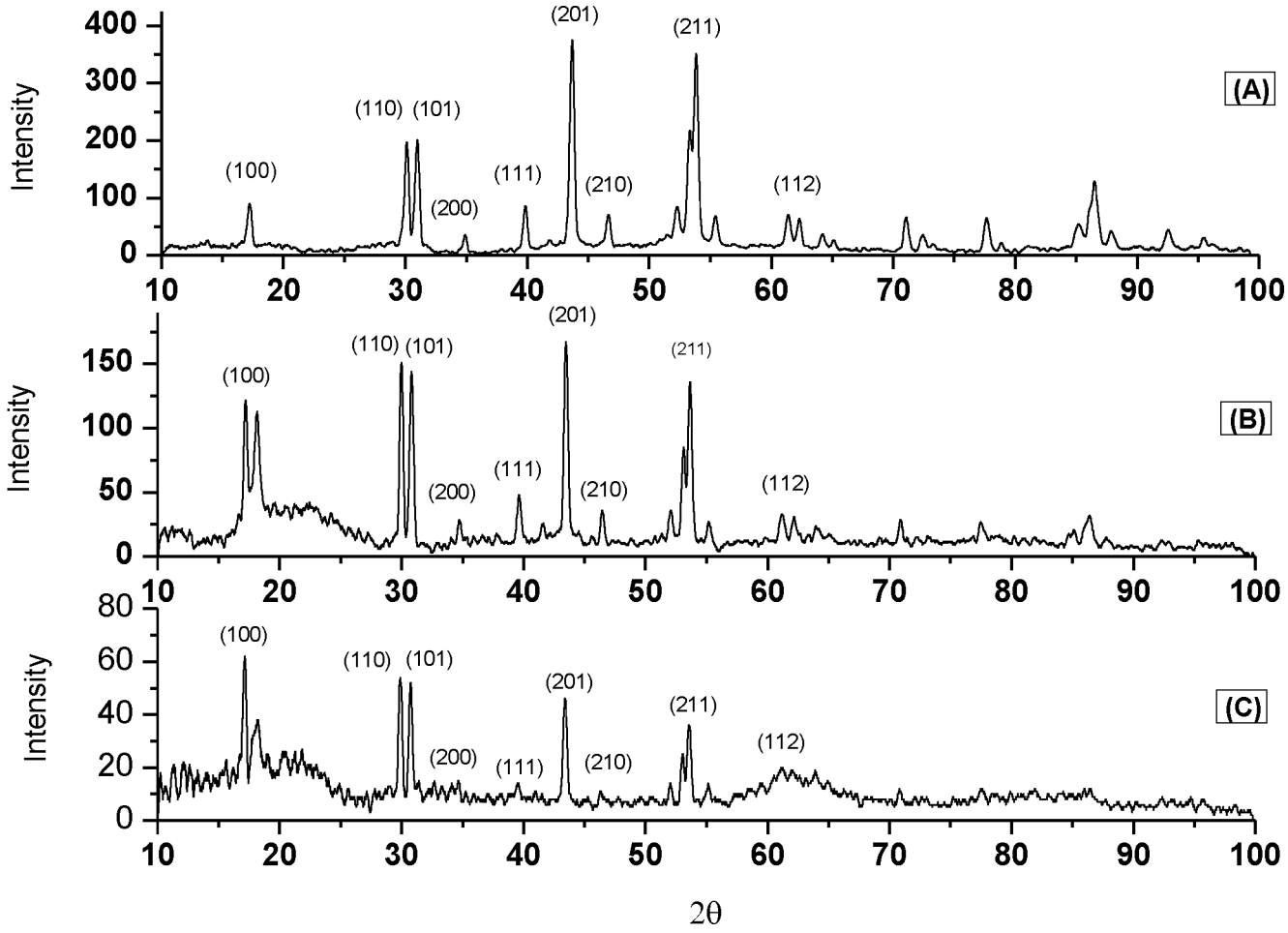

Figure 3.2: XRD spectra for uncapped $NaYF_4$:Yb/Er/Gd (A) and $NaYF_4$:Yb/Er/Gd@Si (B) $NaYF_4$:Yb/Er/Gd@Si@NH_2 (C) UCNPs.

The XRD spectra, Fig. 3.2A, confirms that the particle size for uncapped $NaYF_4$:Yb/Er/Gd UCNP is roughly 40 nm, using the Debye Scherrer equation (3.1) [106],

$$d = \frac{k\lambda}{\beta \cos\theta} \qquad \textbf{(3.1)}$$

where λ is the wavelength of the X-ray source (1.5405 Å), k is an empirical constant with a value of 0.9, β is the full width at half maximum of the diffraction peak, and θ is the angular position. The UCNP size of 40 nm confirms the findings obtained using

TEM. The numbers above each peak are assigned to the crystal phase of the particles, which in this case is hexagonal. For $NaYF_4$:Yb/Er/Gd@Si (Fig. 3.2B) and $NaYF_4$:Yb/Er/Gd@Si@NH_2 (Fig. 3.2C), there is a large broad peak at the $2\theta = 20^\circ$ which corresponds to the non-crystalline silica shell on the UCNP surface. Again the XRD spectra combined with TEM analysis further confirm that the silica or amino cappings had no effect on the crystal structure of the $NaYF_4$:Yb/Er/Gd hexagonal UCNP. No significant size difference was obtained between the different types of UCNPs using XRD.

3.1.3 Absorbance and Emission spectra

Figure 3.3 (insert) shows the near infrared (NIR) absorbance for a typical uncapped $NaYF_4$:Yb/Er/Gd UCNP, which is within the biological window and not near where ClAlTSPc absorbs as will be discussed below.

3.2 UCNP and ClAlTSPc mixed (no chemical bond)

The following studies were done by mixing ClAlTSPc (as an example) with UCNPs without a chemical bond.

3.2.1 UV-Vis Spectra

Fig. 3.3 shows that there was no change in the ClAlTSPc spectrum on addition of UCNPs. No change is expected since the latter absorbs at ~980 nm, and hence do not absorb where the Pc absorbs. The absorption spectral maxima are the same as the excitation spectral maxima for neat ClAlTSPc and in the presence of UCNPs, Fig. 3.4. The emission spectra are mirror images of the excitation and absorption spectra.

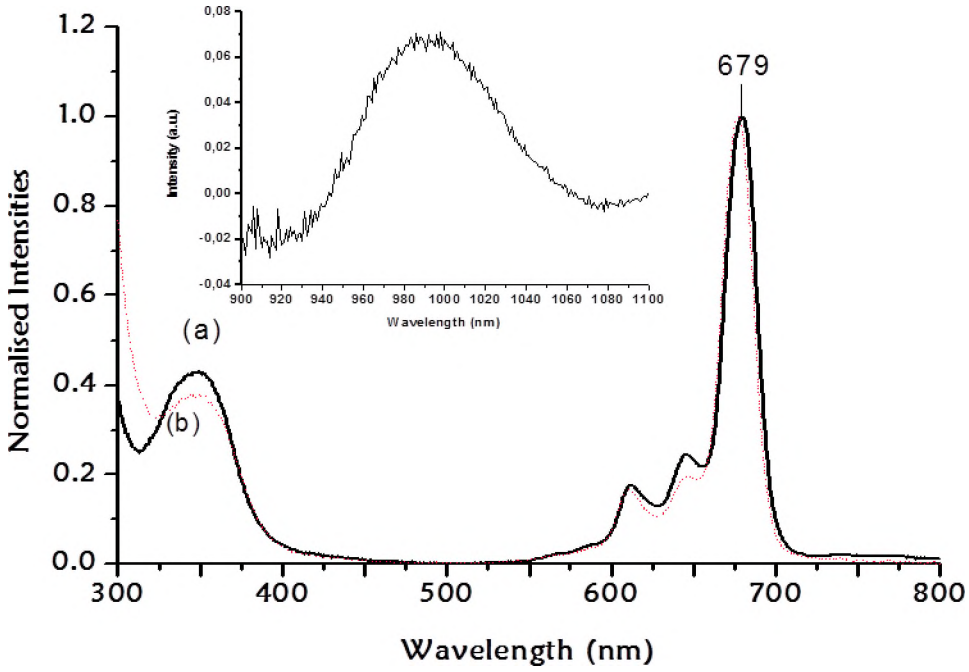

Figure 3.3: UV-Vis Absorption spectra of ClAlTSPc alone (7.3 × 10^{-6} M) (a) and in the presence of $NaYF_4$:Yb/Er/Gd@Si@NH_2 (b) in ethanol. Insert = NIR absorbance spectra for uncapped $NaYF_4$:Yb/Er/Gd UCNPs in cyclohexane.

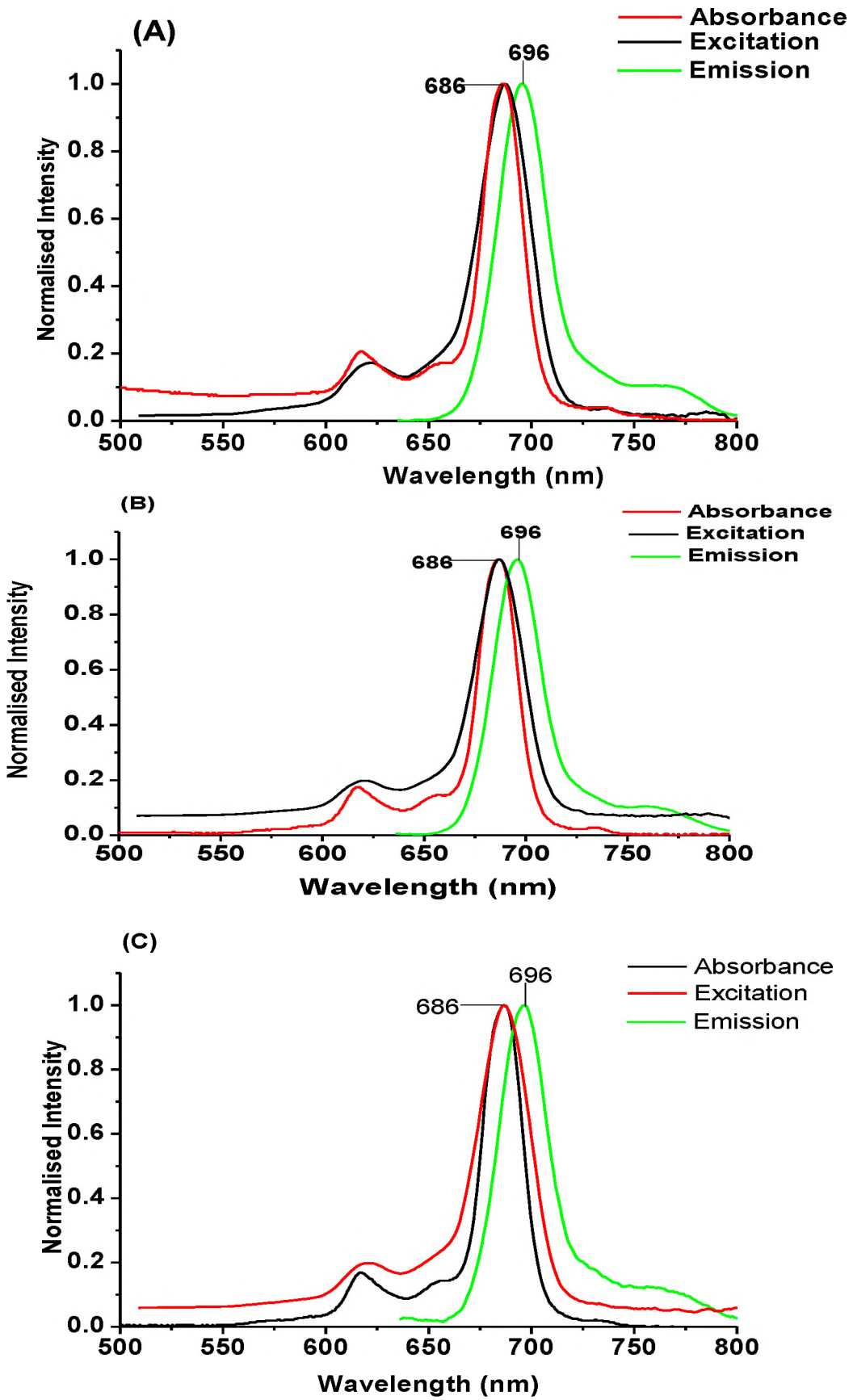

Figure 3.4: Absorption, Excitation and Emission spectra of ClAlTSPc in the presence of (A) $NaYF_4$:Yb/Er/Gd, (B) $NaYF_4$:Yb/Er/Gd@Si and (C) $NaYF_4$:Yb/Er/Gd@Si@NH_2. Excitation was at 630 nm in DMSO.

3.2.2 Photophysical behaviour of ClAlTSPc alone or in the presence of UCNPs: Excitation where ClAlTSPc absorbs.

The studies in this section were done using a mixture of UCNPs (not embedded in fibre) and ClAlTSPc in solution, in order to check the effect of UCNPs on the photophysical behaviour of ClAlTSPc as explained in the introduction. For these studies it was not important to stabilize UCNPs in fibre (as will be done below) since it is the changes in the properties of ClAlTSPc (not UCNPs) being evaluated.

3.2.2.1 Fluorescence quantum yields and lifetimes

The Fluorescence quantum yield of ClAlTSPc alone or with UCNP was determined in DMSO using equation 3.2 [107]:

$$\Phi_F = \Phi_{F(Std)} \frac{F.A_{Std}.n^2}{F_{Std}.A.n_{Std}^2} \quad \textbf{(3.2)}$$

where Φ_F is the quantum yield of the sample and $\Phi_{F(Std)}$ that of the standard ZnPc, $\Phi_{F(Std)}$ = 0.20 in DMSO [108], F and F_{std} represent the areas under the fluorescence emission curve for the sample and standard, respectively; A and A_{std} refer to the absorbance of the sample and standard, respectively and n and n_{Std} are the refractive indices of the sample and standard solutions, respectively. The samples and the standard were both excited at the same relevant wavelength in each case. Excitation was where UCNPs do not absorb and Pcs do.

In Table 3.1, the Φ_F value of ClAlTSPc [109] decreases in the presence of UCNPs due to the heavy atom effect of the latter, which encourages intersystem crossing to the triplet state rather than fluorescence. Fig. 3.5 shows the TCSPC traces of ClAlTSPc in the absence and presence of $NaYF_4$:Yb/Er/Gd@Si@NH_2. Fluorescence lifetimes are longer for ClAlTSPc in the presence of UCNPs and could be due to the protection of the former by the latter from the environment.

Table 3.1: Photophysical parameters of ClAlTSPc in the absence and presence of UCNPs in DMSO.

Analysed Sample	$\Phi_{F(Pc)}$	$\tau_{F(Pc)}$ (ns)	$\Phi_{T(Pc)}$	$\tau_{T(Pc)}$ (μs)
ClAlTSPc alone	0.18	6.51	0.38[a]	103
$NaYF_4$:Yb/Er/Gd@Si/ClAlTSPc	0.15	7.03	0.44	138
$NaYF_4$:Yb/Er/Gd@Si@NH_2/ClAlTSPc	0.14	7.39	0.52	111

[a] data from reference [108]

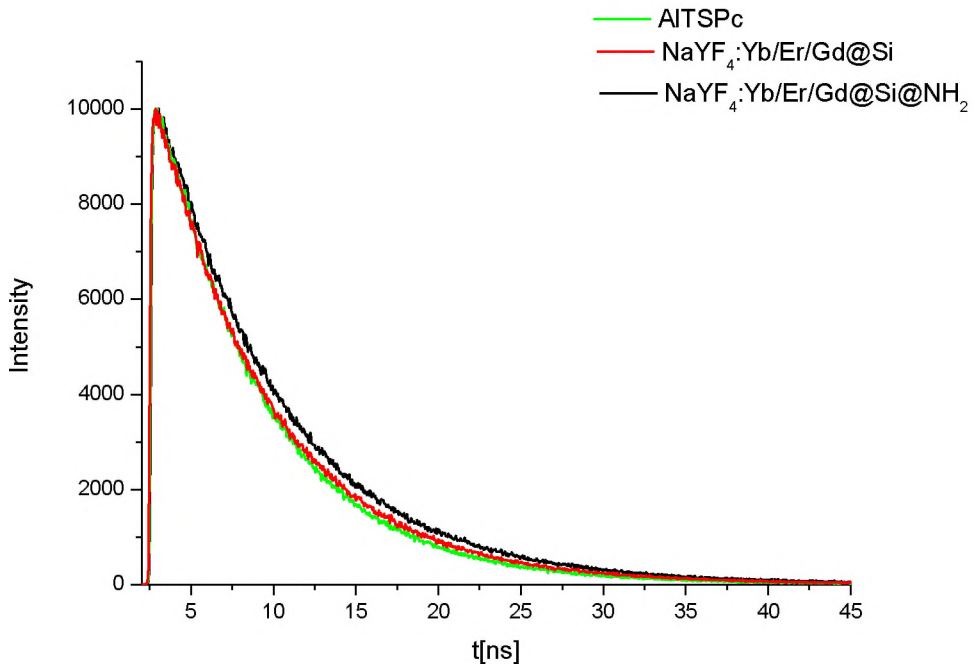

Figure 3.5: TCSPC trace of the ClAlTSPc alone and in the presence of $NaYF_4$:Yb/Er/Gd@Si and or $NaYF_4$:Yb/Er/Gd@Si@NH_2 in DMSO. Excitation at 650 nm

3.2.2.2 Triplet state behaviour

The triplet decay curves for ClAlTSPc alone and in the presence of UCNPs are shown in Fig. 3.6. The data was fitted to a monoexponential decay for ClAlTSPc alone or in the presence of UCNPs. Triplet quantum yields of the ClAlTSPc alone or in the presence of UCNPs were determined by the comparative method, using Eq. 3.3.

$$\Phi_T = \Phi_T^{Std} \frac{\Delta A_T \varepsilon_T^{Std}}{\Delta A_T^{Std} \varepsilon_T} \quad \textbf{(3.3)}$$

where ΔA_T and ΔA_T^{Std} are the changes in the triplet state absorption of the MPc derivative and the standard (ZnPc), respectively. Φ_T^{Std} is the triplet state quantum yield for the standard (Φ_T^{Std} = 0.65 for ZnPc in DMSO [109]). ε_T and ε_T^{Std} are the triplet state extinction coefficients for the MPc derivatives and the standard, respectively. ε_T and ε_T^{Std} are determined using the singlet depletion method using the changes in absorbance of the ground singlet states of both the sample (ΔA_S) and the standard (ΔA_S^{Std}), the changes in triplet state absorptions of the sample (ΔA_T) and the standard (ΔA_T^{Std}) and the molar extinction coefficient of their singlet ground state for both the sample (ε_S) and the standard (ε_S^{Std}) using equations 3.4 and 3.5

$$\varepsilon_T = \varepsilon_s \frac{\Delta A_T}{\Delta A_S} \quad \textbf{(3.4)}$$

$$\varepsilon_T^{Std} = \varepsilon_S^{Std} \frac{\Delta A_T^{Std}}{\Delta A_S^{Std}} \quad \textbf{(3.5)}$$

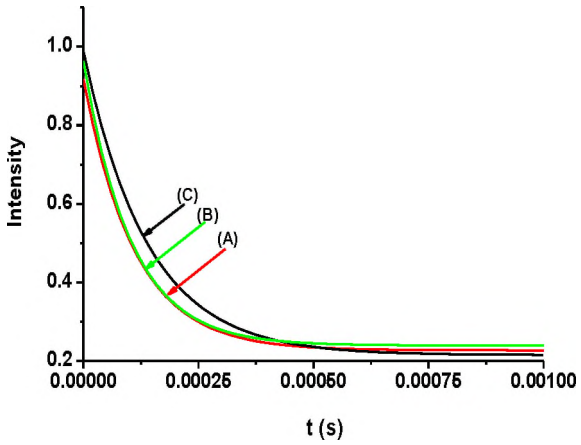

Fig. 3.6 Triplet decay curve of ClAlTSPc alone (A) and in the presence of (B) $NaYF_4$:Yb/Er/Gd@Si and (C) $NaYF_4$:Yb/Er/Gd@Si@NH_2. Solvent = DMSO.

The triplet quantum yield for ClAlTSPc alone was taken from literature [108]. Higher triplet quantum yields are expected (and observed) for ClAlTSPc in the presence of UCNPs as a result of heavy atoms associated with UCNPs which encourages

intersystem crossing to the triplet state, Table 3.1. The triplet lifetimes for ClAlTSPc became longer in the presence of UCNPs, Table 3.1. Lengthening of triplet lifetimes of Pcs in the presence of nanoparticles (such as quantum dots) has been observed before [110] and was attributed to the protection of the Pc by the nanoparticles.

3.2.3 Fluorescence behaviour of UCNPs alone or in the presence of ClAlTSPc: Excitation where UCNPs absorb (at 975 nm)

3.2.3.1 UCNPs alone in solution (not in fibre)

These studies were done in ethanol and DMSO, except for uncapped UCNPs alone which were not soluble in ethanol. Fluorescence analysis of the hexagonal discs produced typical emission peaks associated with UCNPs, Fig. 3.7. The fluorescence exhibited by the UCNPs following excitation at 975 nm, is characteristic of other documented UCNPs, with peaks in the red (~658 nm) and green (~540 nm) region of the electromagnetic spectrum indicating steady upconversion properties. In solution (both DMSO and ethanol) however, the peaks are not as reproducible, hence the UCNPs were embedded in polystyrene fibres as will be discussed in the next section. The fluorescence could be stabilised by repeatedly recording fluorescence (at least 20 runs) as will be discussed later. However when embedded in electrospun fibres there was no need for multiple runs.

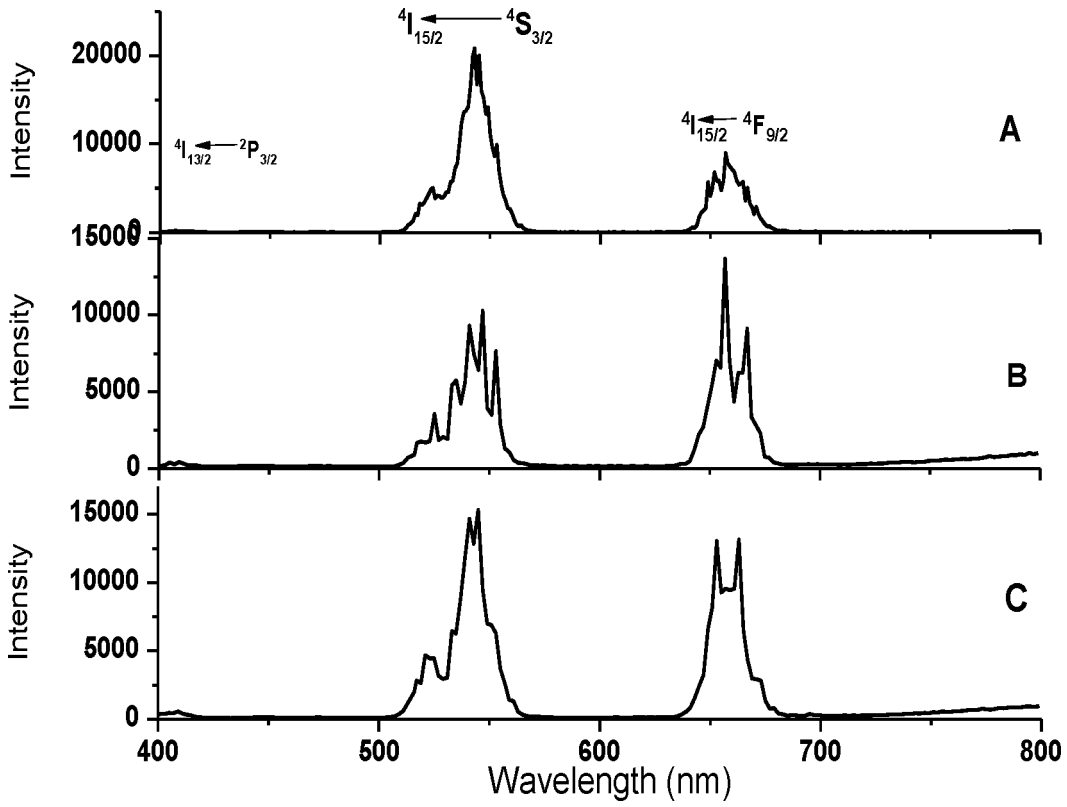

Figure 3.7: Fluorescence spectra for (A) uncapped $NaYF_4$:Yb/Er/Gd UCNP (1.3×10^{-3} g/mL) in cyclohexane, (B) $NaYF_4$:Yb/Er/Gd@Si (6.4×10^{-4} g/mL) in ethanol and (C) $NaYF_4$:Yb/Er/Gd@Si@NH_2 (9.5×10^{-4} g/mL) in ethanol.

UCNPs are known to suffer from surface deactivations which have been attributed to surface defects, and to ligands and solvents that possess high phonon energy [111]. In ethanol, the lack of reproducibility of UCNP fluorescence peaks may be attributed to the OH group in ethanol which may facilitate multiphonon relaxations [111]. High phonon energy results in large non-radiative loss and weak upconversion luminescence [85], hence the irreproducible UCNPs emissions in solutions could be attributed to non-radiative losses. Other solvents such as DMSO were then used in order to minimize these non-radiative losses.

3.2.3.2 UCNPs alone when embedded in fibre, and suspended in DMSO.

First, the fibres are characterised by SEM. The SEM images of the functionalized electrospun PS fibres are shown in Fig. 3.8. SEM was used to study the size, and the morphology of the functionalized fibres.

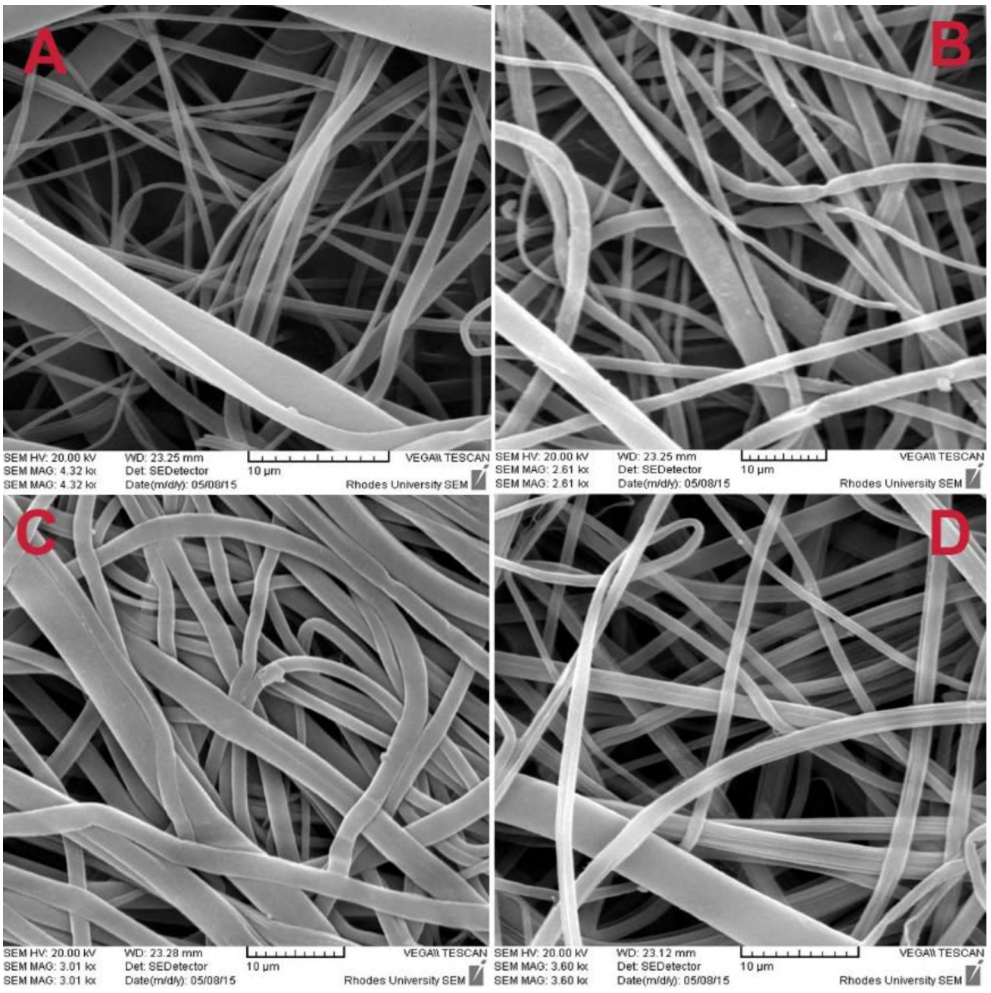

Figure 3.8: SEM images of the electrospun polystyrene fibers alone (A) in the presence of (B) $NaYF_4$:Yb/Er/Gd/PS, (C) $NaYF_4$:Yb/Er/Gd@Si/PS and (D) $NaYF_4$:Yb/Er/Gd@Si@NH_2/PS UCNPs.

The fibres obtained were cylindrical, slightly branched with relatively smooth surfaces. The diameters of the fibres ranged from 1 – 5 µm and there was no significant increase on the fibre's diameter upon functionalization with UCNPs. The UCNP fibres are represented with PS at the end of the name in Table 3.2.

Table 3.2: Absorption spectra and fluorescence data for UCNPs alone, in fibre and in the presence of ClAlTSPc. Excitation was at 975 nm in DMSO.

Analysed Sample	λ (nm)	T_{UCNP} (μs)	Error	χ^2	*Eff*
UCNPs on fibre (suspended in DMSO with or without ClAlTSPc)					
Uncapped $NaYF_4$:Yb/Er/Gd/PS	440	30.2	(± 9.5)	1.03	
	488	2.6	(± 0.4)	1.16	
	540	13	(±7.1)	0.97	
	658	443.7	(± 56.9)	0.99	
	755	7	(± 1.7)	1.16	
Uncapped $NaYF_4$:Yb/Er/Gd/ PS suspended in DMSO solution of ClAlTSPc	440	36	(± 18.9)	1	
	488	3.8	(± 2.3)	1.03	
	540	16.9	(± 1.0)	0.97	
	658	a	a	a	a
	755	8.5	(± 7.1)	1	
$NaYF_4$:Yb/Er/Gd@Si/PS	440	46.3	(± 46.8)	1.02	
	488	5.3	(± 0.5)	1.03	
	540	250	(± 37.3)	1.02	
	658	420.6	(± 89.5)	0.99	
	755	28	(± 16.5)	1.01	
$NaYF_4$:Yb/Er/Gd@Si/ PS Suspended in DMSO solution of ClAlTSPc	440	a	a	a	
	488	7.6	(± 2.8)	1.01	
	540	141	(± 120.5)	0.97	
	658	110.9	(± 53.9)	1	0.74
	755	24.1	(± 186.0)	0.97	
$NaYF_4$:Yb/Er/Gd@Si@NH_2/PS	440	33	(± 27.8)	0.99	
	488	4.8	(± 0.6)	1.15	
	540	36.9	(± 10.0)	1.03	
	658	51.8	(± 18.0)	1	
	755	10.5	(± 1.8)	1.06	
$NaYF_4$:Yb/Er/Gd@Si@NH_2 /PS Suspended in DMSO solution of ClAlTSPc	440	38.4	(± 16.7)	1	
	488	7.9	(± 1.2)	0.98	
	540	57	(± 46.1)	1.03	
	658	37.3	(± 10.4)	1.18	0.28
	755	17.2	(± 8.8)	1.01	

[a] no peak

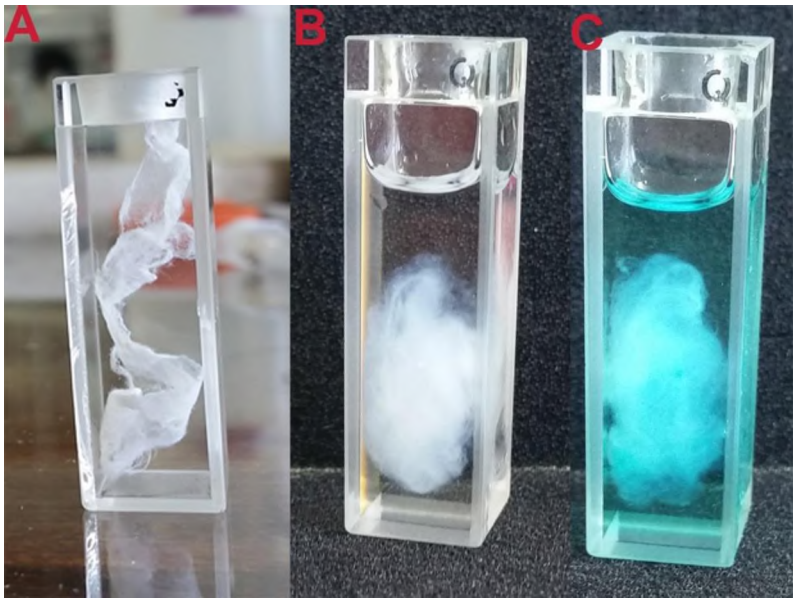

Figure 3.9: Photos of $NaYF_4$:Yb/Er/Gd@Si/PS in fluorescence cell without DMSO (A), $NaYF_4$:Yb/Er/Gd@Si/PS suspended in DMSO solution (B) and $NaYF_4$:Yb/Er/Gd@Si/PS suspended in DMSO ClAlTSPc solution (C).

The UCNPs electrospun fibres were suspended in DMSO and they did not dissolve, Fig 3.9 B. The fluorescence behaviour of the UCNPs was investigated when embedded in electrospun fibres and suspended in DMSO in the absence of ClAlTSPc. For these studies, excitation was at 975 nm where UCNPs absorb.

Fig. 3.10 shows the emission spectra of the modified fibres suspended in DMSO in the absence of ClAlTSPc. The UCNPs showed intense and incredibly stable fluorescence emissions in the visible region. The emission increased after consecutive exposures and then stabilized. The peaks in the blue (440 nm and 488 nm) and far IR (755 nm) regions of the spectrum remain stable while the red (540 nm) and green (658 nm) peaks increased and then stabilized.

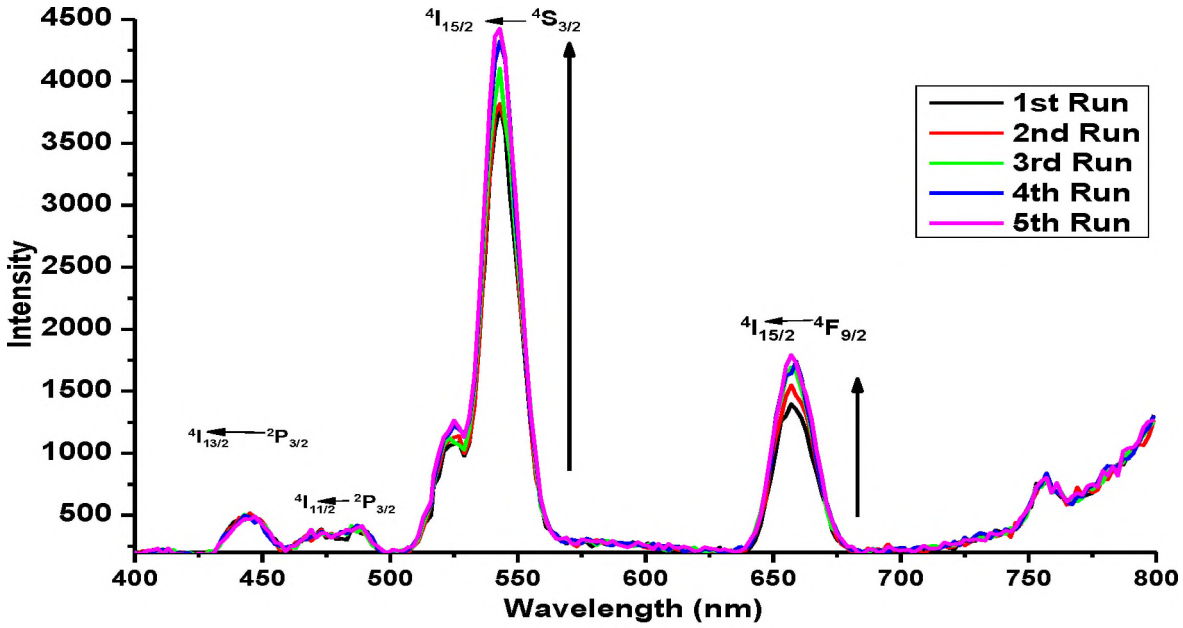

Figure 3.10: Fluorescence spectra of $NaYF_4$:Yb/Er/Gd@Si/PS suspended in DMSO.

As stated above, high phonon energy results in large non-radiative loss and weak upconversion luminescence [85]. Thus, the increase in emission intensity for $NaYF_4$:Yb/Er/Gd@Si/PS with time may be due to a decrease in the phonon energy (probably as a result of isolation from solution), resulting in improved fluorescence. Fig. 3.11, showing typical UCNP fluorescence [112,113], compares the fluorescence spectra of uncapped $NaYF_4$:Yb/Er/Gd/PS, $NaYF_4$:Yb/Er/Gd@Si/PS and $NaYF_4$:Yb/Er/Gd@Si@NH_2/PS when suspended in DMSO. Compared to $NaYF_4$:Yb/Er/Gd@Si/PS the uncapped $NaYF_4$:Yb/Er/Gd/PS and $NaYF_4$:Yb/Er/Gd@Si@NH_2/PS have stronger emission peaks at 440 nm, 488 nm and 755 nm and weaker peaks at 540 nm and 688 nm. There are several factors which affect relative intensities of the UCNP emission peaks such as the size and morphology of the NPs [114] as well as the surface quenching effects [111]. Thus, the changes in the relative intensities of the different UCNPs could be related to some or all of these factors.

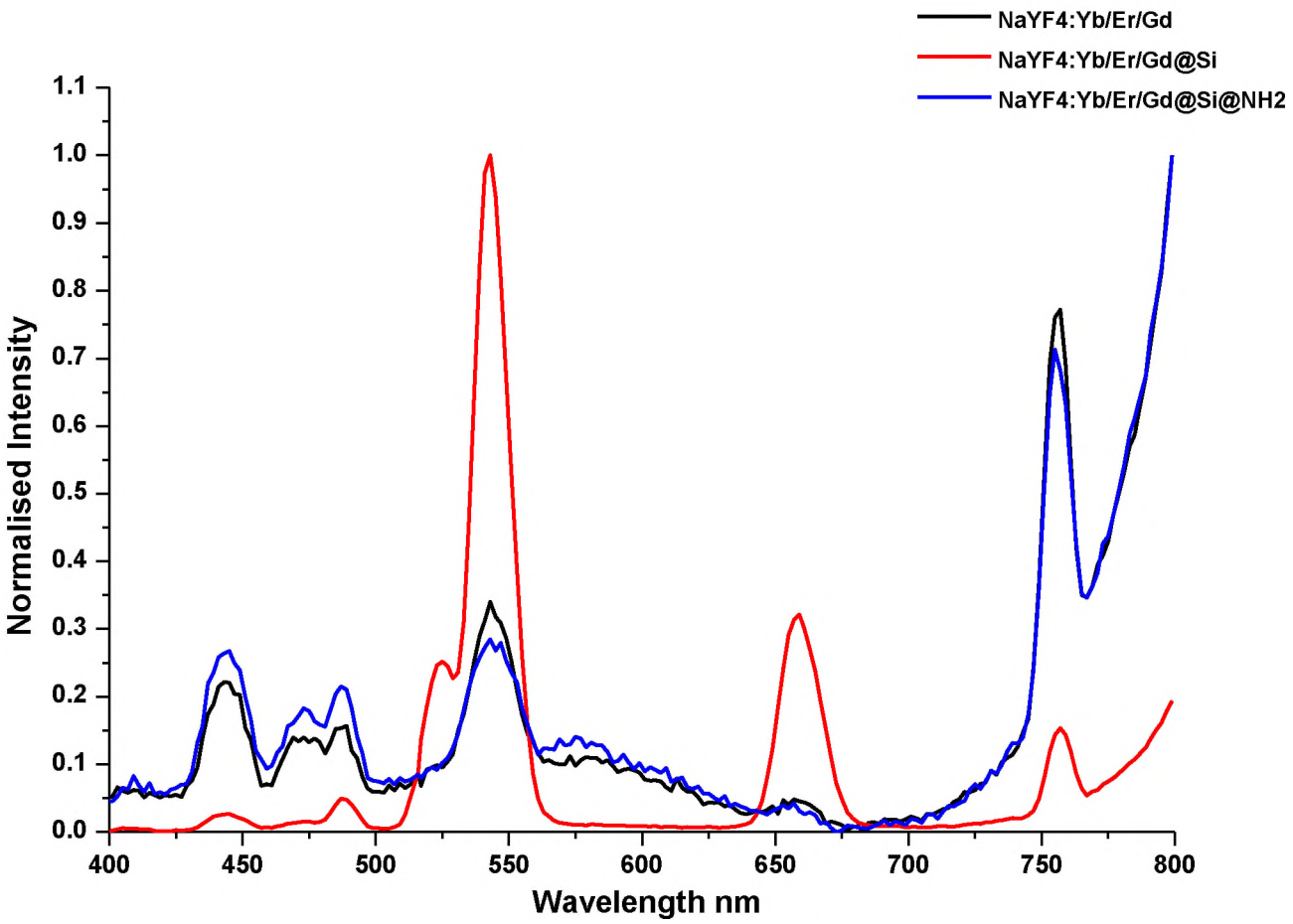

Figure 3.11: Fluorescence spectra of uncapped $NaYF_4$:Yb/Er/Gd/PS, $NaYF_4$:Yb/Er/Gd@Si/PS and $NaYF_4$:Yb/Er/Gd@Si@NH_2/PS in DMSO.

3.2.3.3 UCNPs studied when embedded in fibre, and suspended in DMSO solution containing ClAlTSPc.

For these studies, the fluorescence behaviour of the UCNPs was investigated when embedded in electrospun fibres and suspended in DMSO containing ClAlTSPc and excited at 975 nm where UCNPs absorb and ClAlTSPc does not. Fig 3.9 can show clearly the fibres alone in DMSO compared with the ClAlTSPc and DMSO solution.

The fluorescence lifetimes, Table 3.2, can validate the data seen in Fig 3.11. Firstly the uncapped $NaYF_4$:Yb/Er/Gd UCNPs/PS, when suspended in DMSO only gave τ_F of 0.013 ms and 0.444 ms for the 540 nm and 658 nm respectively. The 658 nm τ_F is unexpectedly high. However when studied with the DMSO in the presence of ClAlTSPc, the 540 nm increased (0.017 ms) and the 658 nm was not detectable. The loss of the 658 nm lifetime could be attributed to FRET, however a 100 % *Eff* is highly unlikely.

For $NaYF_4$:Yb/Er/Gd@Si/PS in DMSO solution the lifetimes mirrored the fluorescence spectra. The 540 nm (0.250 ms) lifetime was much larger than the uncapped while the 658 nm (0.420 ms) is slightly smaller. It is not unexpected considering a larger portion of the energy is relaxing from the $^4S_{3/2}$ energy level, Fig 1.10. When suspended in DMSO, in the presence of ClAlTSPc, the 540 nm (0.141 ms) and the 658 nm (0.111 ms) both decreased. The 658 nm drop is drastic. Although both decreased, the fluorescence decay spectra for the 540 nm was incredibly noisy resulting in an error of 0.120 ms. Only when compared with the fluorescence spectra can a conclusion be made. The same could be said for the 658 nm, however the major loss of τ_F, and relatively small error approximation for the red peak is a strong indication of FRET occurring between the UCNPs and the ClAlTSPc.

The $NaYF_4$:Yb/Er/Gd@Si@NH_2/PS suspended in DMSO displayed 0.037 ms and 0.052 ms for the 540 nm and 658 nm, respectively. When looking at Fig 3.11 low lifetimes are expected since the fluorescence is so weak at 540 and 658 nm. In the presence of DMSO and the ClAlTSPc the 540 nm (0.057 ms) increased while for the 658 nm (0.037 ms) decreased. Again these results although small may be an indication of FRET.

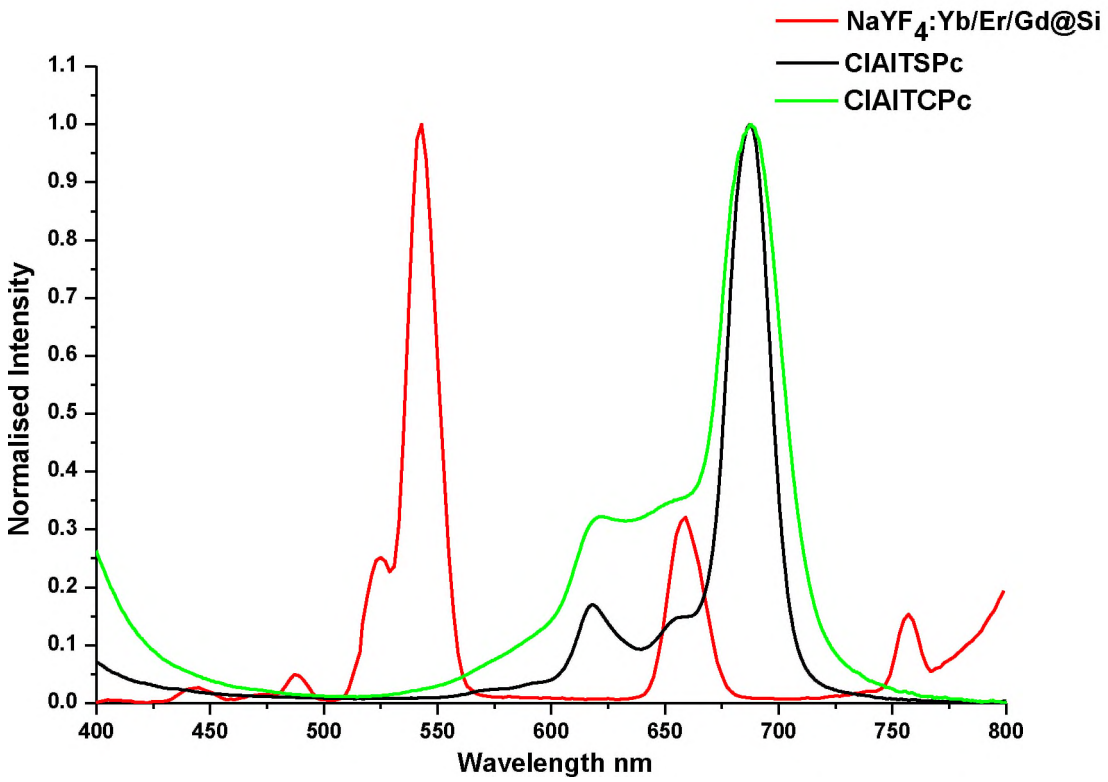

Figure 3.12: Fluorescence spectra for $NaYF_4$:Yb/Er/Gd@Si/PS and the absorbance for ClAlTSPc and ClAlTCPc in DMSO.

As mentioned above the fluorescence lifetimes for $NaYF_4$:Yb/Er/Gd@Si@NH_2/PS and uncapped $NaYF_4$:Yb/Er/Gd/PS saw an increase at all wavelengths (except at 658 nm) in the presence of ClAlTSPc. The decrease in emission at 658 nm for the $NaYF_4$:Yb/Er/Gd@Si/PS which overlaps with the Q band of ClAlTSPc may be attributed to FRET, Fig 3.12.

A decrease in phonon energy results in an increase of the lifetime [115]. Hence the observed increase in lifetimes for some of the wavelengths for $NaYF_4$:Yb/Er/Gd@Si@NH_2/PS and uncapped $NaYF_4$:Yb/Er/Gd/PS in the presence of ClAlTSPc could be related to a decrease in phonon energy as a result of the interaction between the UCNPs embedded in electrospun fibre and ClAlTSPc in solution. For $NaYF_4$:Yb/Er/Gd@Si/PS, there was no emission at 440 nm in the presence of ClAlTSPc, and there was a decrease in emission lifetime at 540 nm, 658 nm and 755

nm. A decrease in lifetime suggests increased phonon energy or quenching effects in the presence ClAlTSPc.

It has been reported before [111] that as the size of the UCNPs decreases, the surface-induced defects increase, resulting in the increase in multiphonon-assisted nonradiative relaxations, which could lead to a decrease in lifetimes. However, the sizes of the three UCNPS are about the same. For FRET to occur there has to be an overlap between the donor (UCNPs) emission and acceptor (ClAlTSPc) absorption as shown in Fig. 3.12 for the 658 emission. At 658 nm, FRET is possible due to the overlap of the absorption of ClAlTSPc and the emission of UCNPs, Fig. 3.12, which is a requirement for FRET and will be discussed below. The decrease in the lifetime at 540 and 755 nm, for $NaYF_4$:Yb/Er/Gd@Si/PS could not be related to FRET since there is minimal ClAlTSPc absorption at these wavelengths.

If FRET occurs, there should be a decrease in donor emission and the stimulated emission of the acceptor. From Fig. 3.13, it is evident that the red emission peak (at 658 nm) of the donor (UCNP) has decreased dramatically in intensity, suggesting the occurrence of FRET. There is only a small increase in background where the ClAlTSPc emission is expected at ~ 690 nm (see Fig. 3.13). FRET is not the only process that results in the decrease in the donor emission [116,117], hence the observed weak stimulated emission of ClAlTSPc which does not correspond to the large decrease in UCNP emission. There are many factors other than FRET reported (and are still under debate) that influence photoluminescence decrease in nanoparticles such as quantum dots (QDs) [116–119]. For example, it has been reported that for QD-Porphyrin nanocomposites, the major part of the observed quenching of QD photoluminescence can be assigned to non-FRET processes [119]. As already stated, the surface properties and the crystal structure of nanocrystals can change the intensity of UCNP fluorescence peaks [120]. Thus the decrease of the red

peak at 658 nm could also be due to changes in the surface properties of UCNPs embedded in fibre and suspended in ClAlTSPc solution.

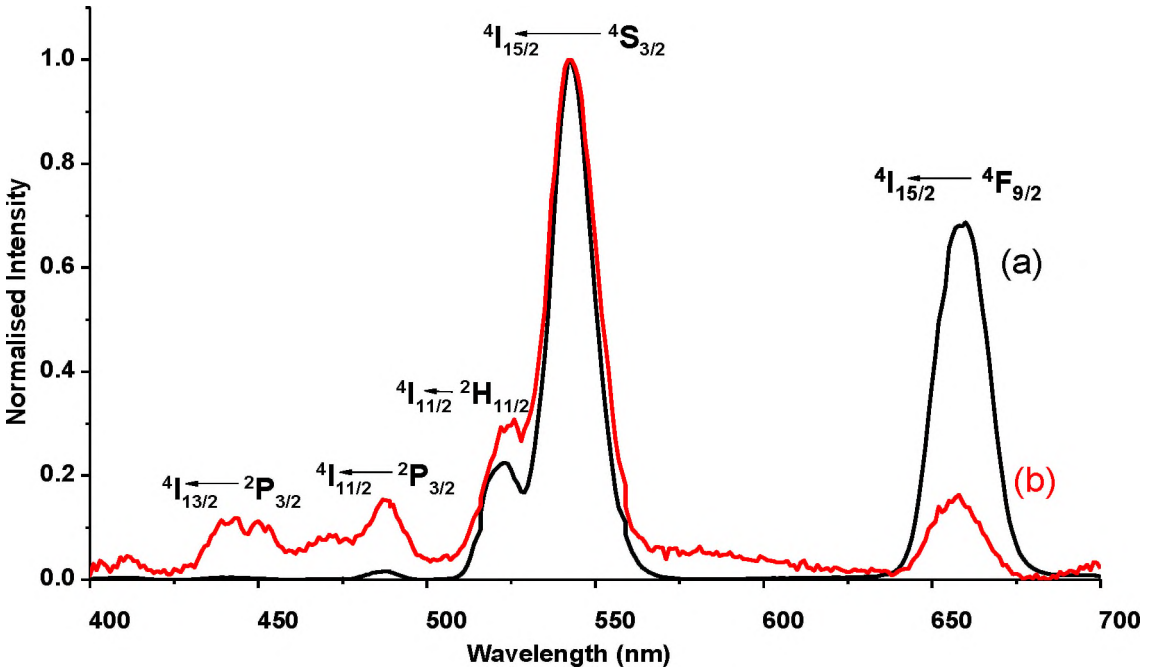

Figure 3.13: Fluorescence emission for $NaYF_4$:Yb/Er/Gd@Si/PS (a) and $NaYF_4$:Yb/Er/Gd@Si /PS suspended in ClAlTSPc (8.3×10^{-6} M) (b) in DMSO.

The peaks between 400 and 600 nm re-appear for $NaYF_4$:Yb/Er/Gd@Si/PS in the presence of ClAlTSPc, Fig. 3.13. The increase in the intensity of these peaks could be due to decrease in surface quenching effects of the UCNPs in fibre in the vicinity of ClAlTSPc in solution. Using equation 1.2, FRET efficiencies for energy transfer from UCNPs to ClAlTSPc following excitation at 975 nm (exciting UCNPs) were estimated to be 74 % and 28 % in DMSO, Table 3.2, for $NaYF_4$:Yb/Er/Gd@Si/PS and $NaYF_4$:Yb/Er/Gd@Si@NH_2/PS, respectively. The larger *Eff* for $NaYF_4$:Yb/Er/Gd@Si/PS/ClAlTSPc is a result of the more intense emission at 658 nm for $NaYF_4$:Yb/Er/Gd@Si/PS in the absence of ClAlTSPc compared to the rest of the UCNPs. For uncapped $NaYF_4$:Yb/Er/Gd/PS, there was no emission at 658 nm in the presence of ClAlTSPc making the estimation of *Eff* difficult.

3.2.4 Singlet oxygen generation by ClAlTSPc in the presence of UCNPs

UCNPs were embedded in electrospun fibres for these studies and suspended in a DMSO solution of ClAlTSPc in order to stabilize the emission of UCNPs, since it is expected that there will be FRET between UCNPs and ClAlTSPc. Fig. 3.14 shows the degradation profile of DPBF (a singlet oxygen quencher) on excitation of $NaYF_4$:Yb/Er/Gd@Si/PS when suspended in DMSO containing DPBF and ClAlTSPc and excited at 975 nm, where UCNPs absorb, but ClAlTSPc does not absorb. There was no decrease in the DPBF absorption for ClAlTSPc alone when irradiation was performed at 975 nm. Thus in the presence of the UCNPs and ClAlTSPc the decrease of the DPBF peak at 418 nm is proof of singlet oxygen generation by ClAlTSPc following excitation of UCNP and the energy transfer between the two. When UCNPs (which are not embedded in fibre) and ClAlTSPc were mixed in a DMSO solution, the DPBF peaks were repeatedly irregular, unstable and thus irreproducible.

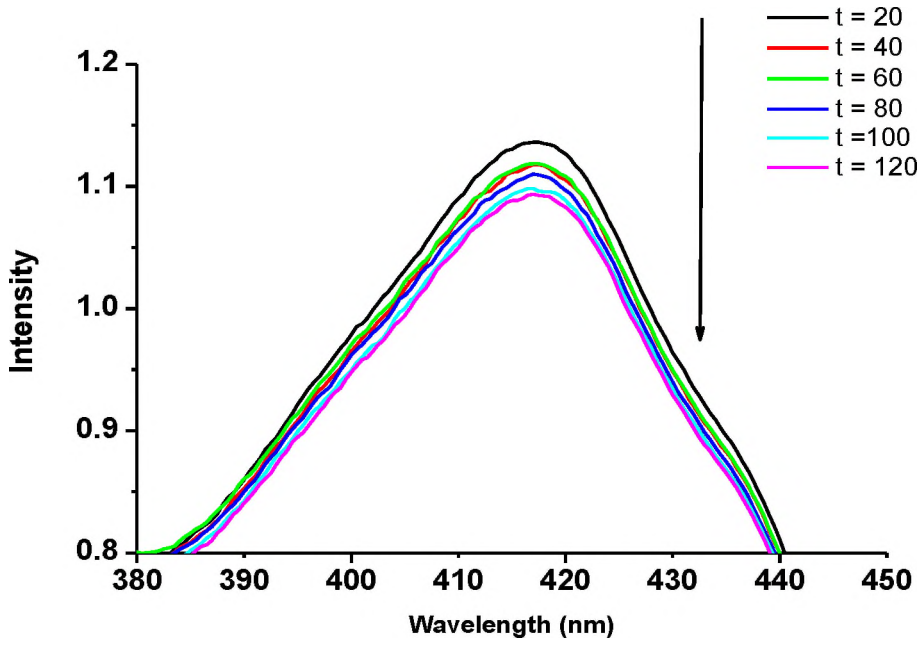

Figure 3.14: Degradation profile of DPBF in the presence $NaYF_4$:Yb/Er/Gd@Si/PS suspended in DMSO of ClAlTSPc (7.2×10^{-6} M) containing DPBF (4.9×10^{-5} M). Time = 0 to 120 min (20 min interval).

3.3 Characterization of the conjugates of ClAlTSPc and ClAlTCPc with UCNPs (chemically linked)

ClAlTSPc was linked to UCNPs via sulfonamide bond to form $NaYF_4$:Yb/Er/Gd@Si@NH_2/ClAlTSPc, while ClAlTCPc was linked via an amide bond to form $NaYF_4$:Yb/Er/Gd@Si@NH_2/ClAlTCPc. The linking to the Pcs is represented in Schemes 3.2 and 3.3. Considering the approximate size of the Pc of 1 nm, the linking of more than one UCNPs to a Pc is unlikely from size consideration. But the reverse is possible where more than one Pc links to one UCNP.

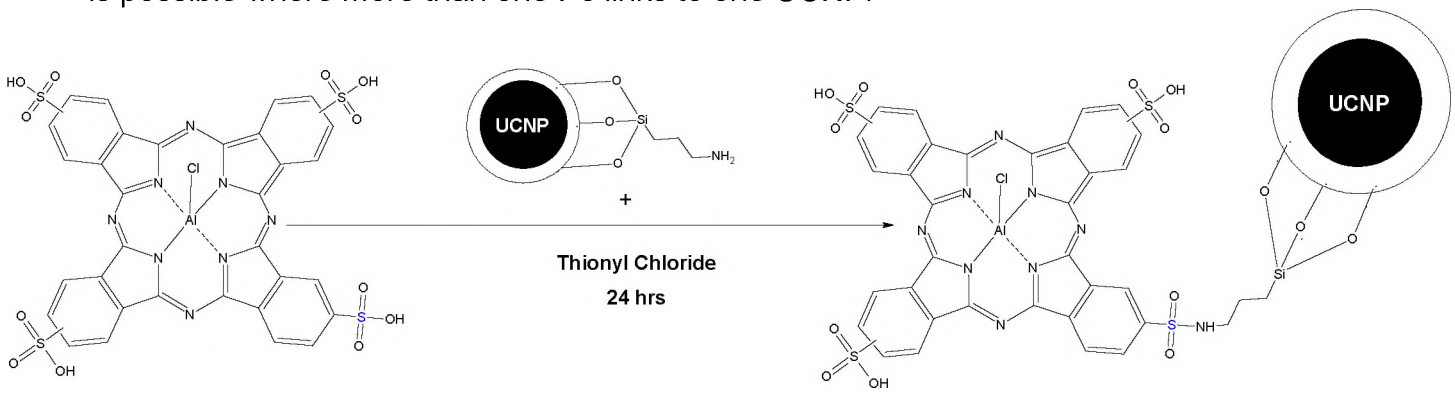

Scheme 3.2: Schematic diagram for the formation of $NaYF_4$:Yb/Er/Gd@Si@NH_2/ClAlTSPc

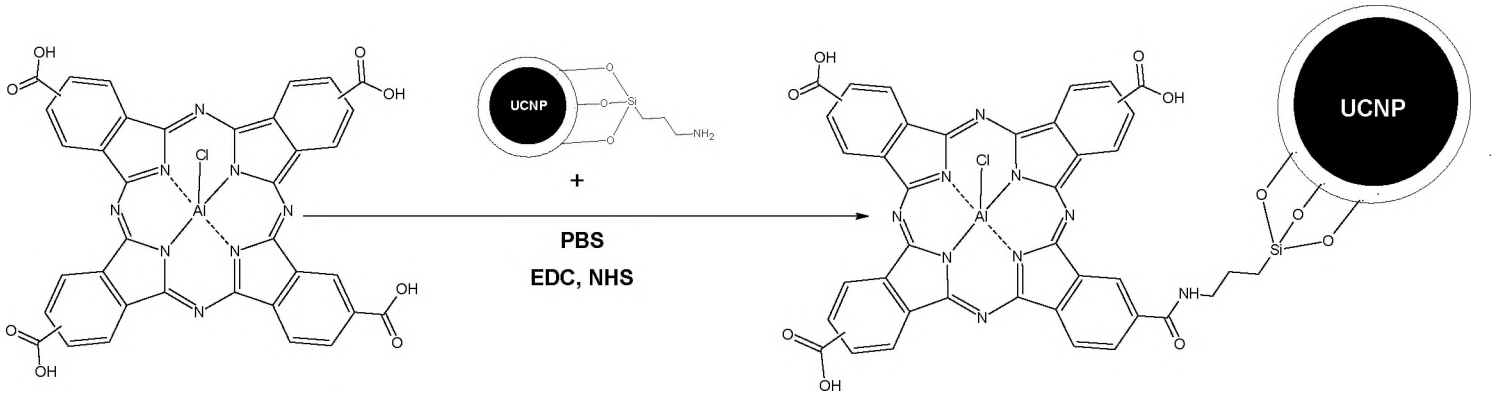

Scheme 3.3: Schematic diagram for the formation of $NaYF_4$:Yb/Er/Gd@Si@NH_2/ ClAlTCPc.

3.3.1 TEM analysis

The TEM images of $NaYF_4$:Yb/Er/Gd@Si@NH_2 UCNPs have been presented in Figure 3.15 but are shown here since a new batch of $NaYF_4$:Yb/Er/Gd@Si@NH_2 UCNPs was synthesized. The TEM image of $NaYF_4$:Yb/Er/Gd@Si@NH_2 UCNPs, Fig. 3.15A shows aggregation in a majority of the sample however single particles (insert in Fig 3.15A) were found showing the silica shell. The presence of the lone particles indicate that the particles display this aggregation due to the slow rate of evaporation experienced by the solvent they were dispersed in. The size for $NaYF_4$:Yb/Er/Gd@Si@NH_2 was ~ 60 nm. TEM analysis of the ClAlTCPc and ClAlTSPc conjugates is shown in Fig. 3.15B and C respectively. Both conjugates display clear silhouettes around their core structure implying that the integrity of the silica scaffold layer is maintained. The size of the UCNPs did not change much on conjugation. The aggregation of $NaYF_4$:Yb/Er/Gd@Si@NH_2 continues on conjugation to the Pcs. Aggregation of Pcs is well documented [121] and has been widely reported to be due to π-π stacking between the rings of the Pcs. The interaction between Pc molecules on adjacent UCNPs would result in increased aggregation.

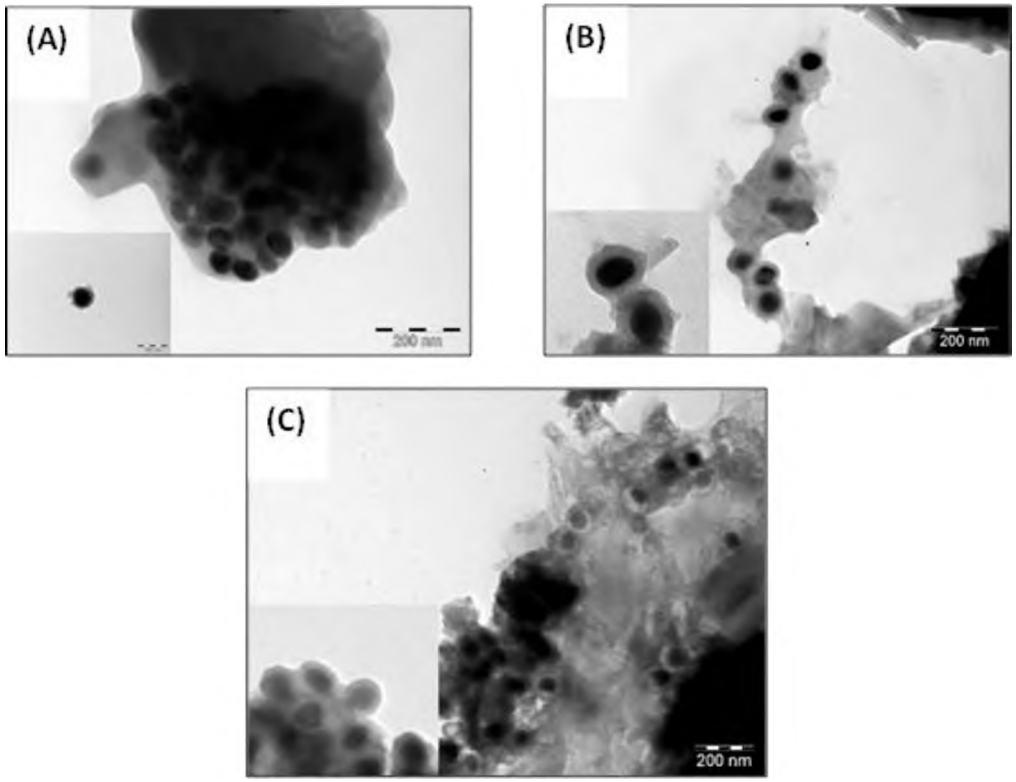

Figure 3.15: TEM images of (A) $NaYF_4$:Yb/Er/Gd@Si@NH_2 UCNP (with isolated NP as an insert), (B) $NaYF_4$:Yb/Er/Gd@Si@NH_2/ClAlTCPc conjugate and (C) $NaYF_4$:Yb/Er/Gd@Si@NH_2/ClAlTSPc conjugate.(Close up NPs are shown as in insets in A, B and C).

3.3.2. XRD Analysis

UCNPs are known to have two crystal phases; cubic, α-phase, or hexagonal, β-phase. The spectra in Fig. 3.16 confirm a β-phase crystal structure. Fig 3.16 shows that the peaks of the conjugates ($NaYF_4$:Yb/Er/Gd@Si@NH_2/ClAlTCPc and $NaYF_4$:Yb/Er/Gd@Si@NH_2/ClAlTSPc) are a match with those of the unconjugated $NaYF_4$:Yb/Er/Gd@Si@NH_2 UCNPs. Interestingly the slightly broad peaks in the $2\theta = 20^\circ$ region are due to the known broad XRD pattern of the Pcs [122]. From Fig. 3.16 it is clear that the inner crystal structure of the core UCNPs remains unchanged following conjugation.

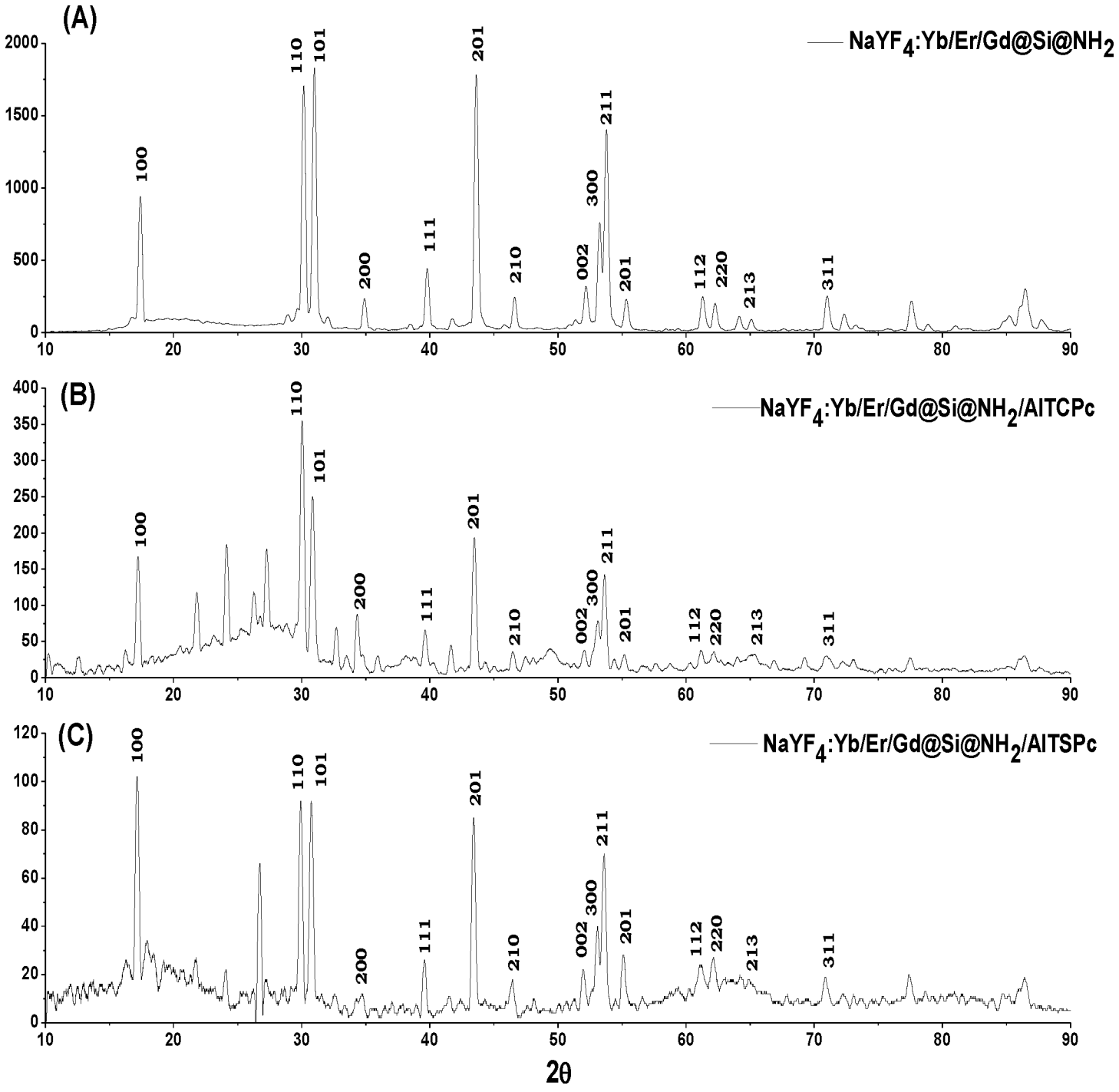

Figure 3.16: XRD spectra for (a) **$NaYF_4$:Yb/Er/Gd@*Si@NH_2*, *(b)*** **$NaYF_4$:Yb/Er/Gd@*Si@NH_2/ ClAITCPc** ***and (c)*** **$NaYF_4$:Yb/Er/Gd@*Si@NH_2/ClAITSPc***

The particle size for $NaYF_4$:Yb/Er/Gd@Si@NH_2 was found to be roughly 60 nm (confirming the values obtained using TEM), using the Debye Scherrer equation (3.1) [106].

3.3.3. FTIR spectra

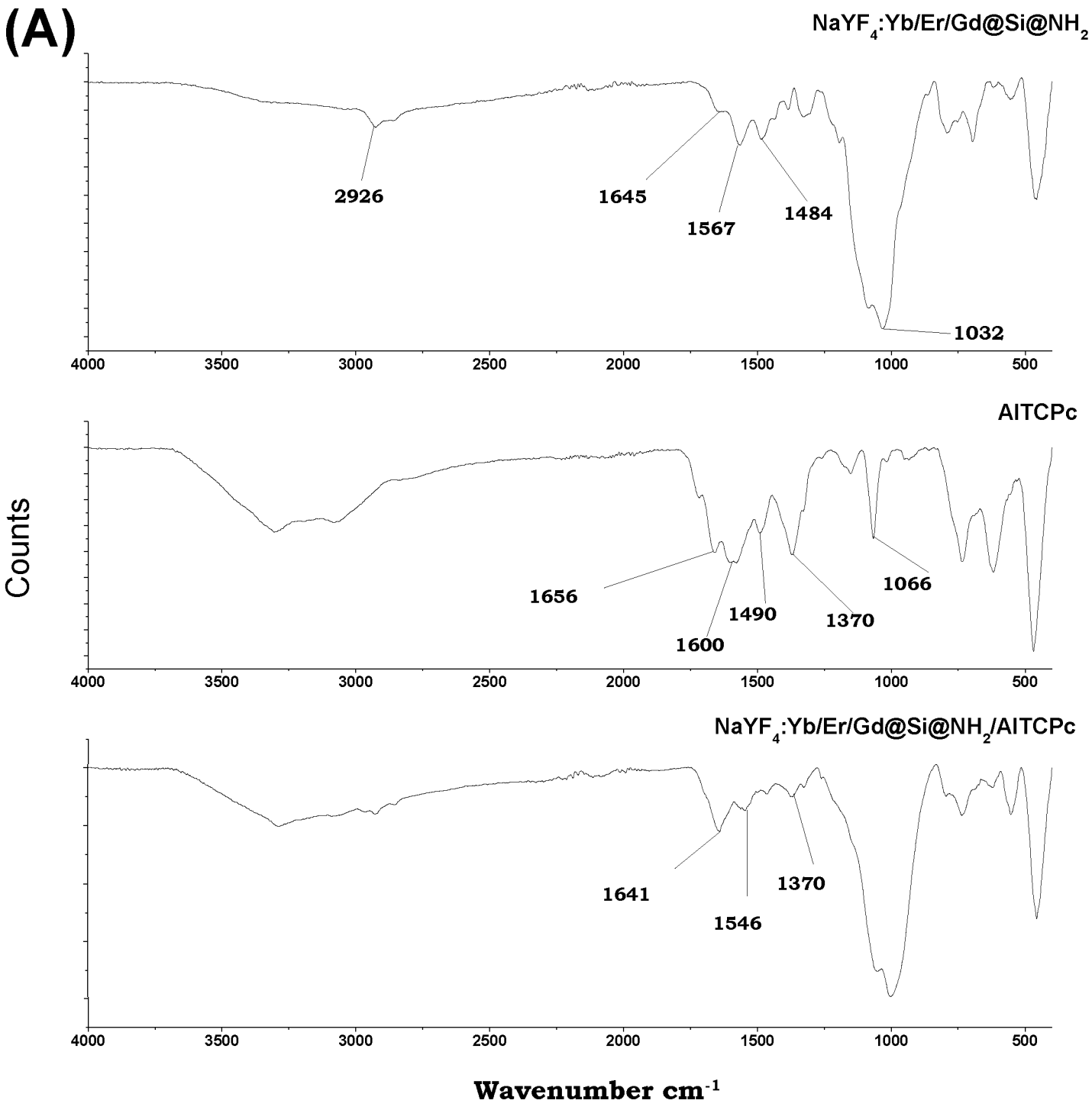

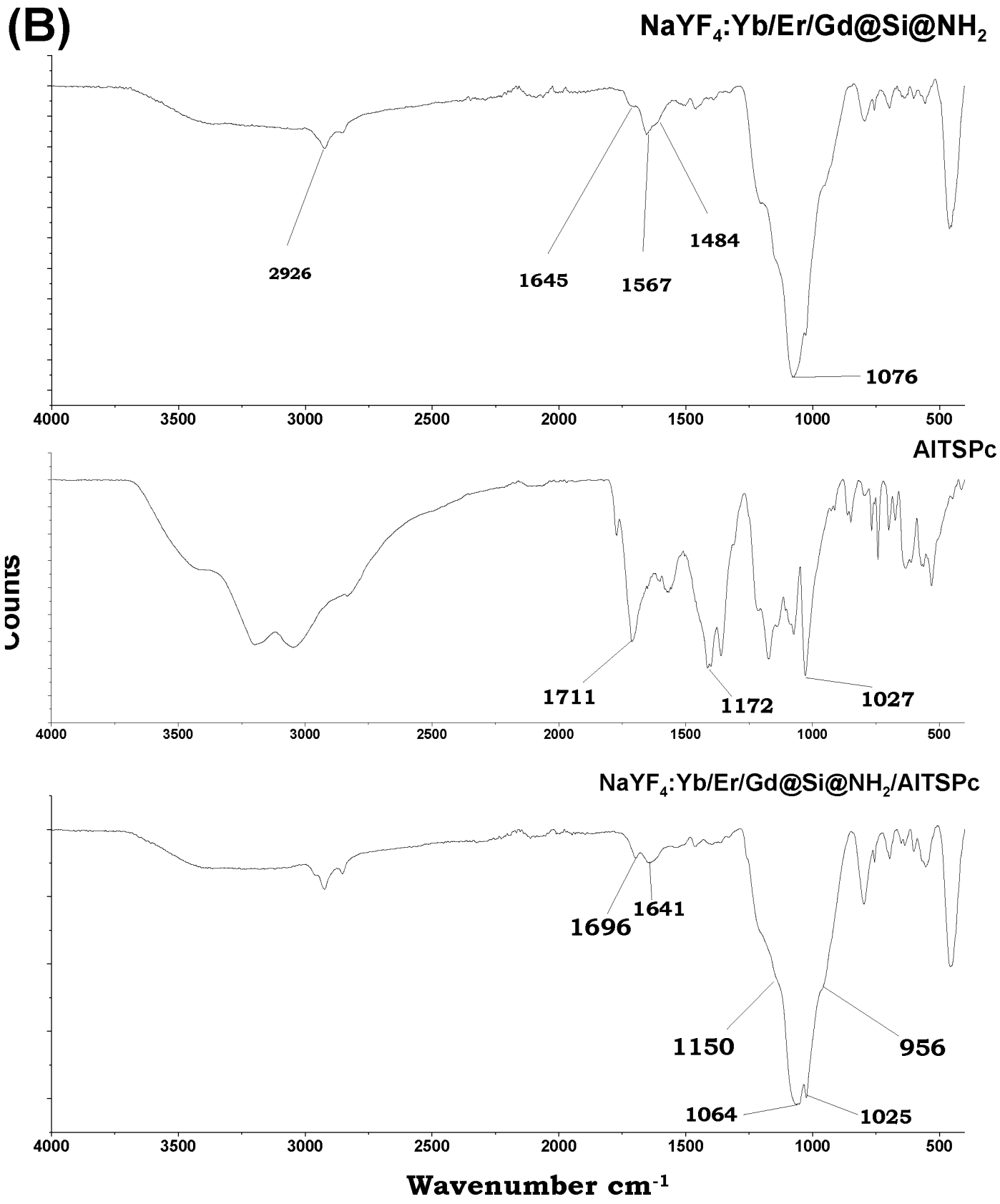

Figure 3.17: FTIR Profiles for (A) $NaYF_4$:Yb/Er/Gd@Si@NH_2 UCNPs, ClAlTCPc and $NaYF_4$:Yb/Er/Gd@Si@NH_2/ClAlTCPc conjugate and (B) $NaYF_4$:Yb/Er/Gd@Si@NH_2 UCNPs, ClAlTSPc and $NaYF_4$:Yb/Er/Gd@Si@NH_2/ClAlTSPc conjugate.

Fig. 3.17A shows the IR spectra for the ClAlTCPc and its conjugate. For ClAlTCPc alone, the following peaks are observed: OH at 3300 cm^{-1}, CH at 3080 cm^{-1}, the C=O groups at 1600 cm^{-1}, OH bend at 1370 cm^{-1}. Upon conjugation the OH groups shifts from 3300 cm^{-1} to 3291 cm^{-1}. The band at 1641 cm^{-1} may be due to the amide bond. It is known that shifts in IR bands confirm structural change [123–125].

For ClAlTSPc–UCNP conjugate, Fig. 3.17B, the secondary sulfonamide band is expected near 1160 cm^{-1}, but could not be clearly identified due to the large SiOH peak in the 1000 cm^{-1} and 1250 cm^{-1} region. Hence XPS was employed below for further characterization.

3.3.4 XPS

3.3.4.1 ClAlTCPc

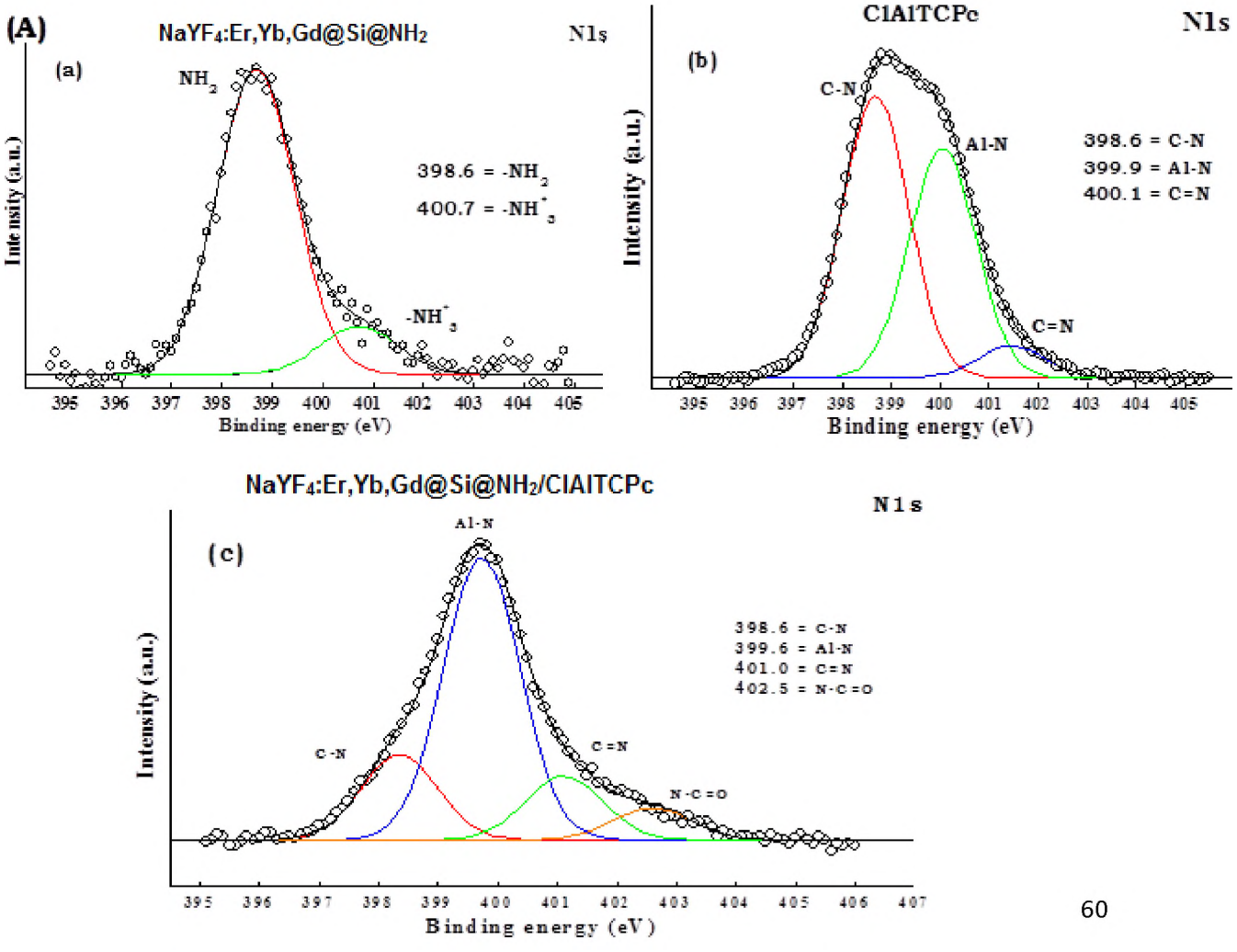

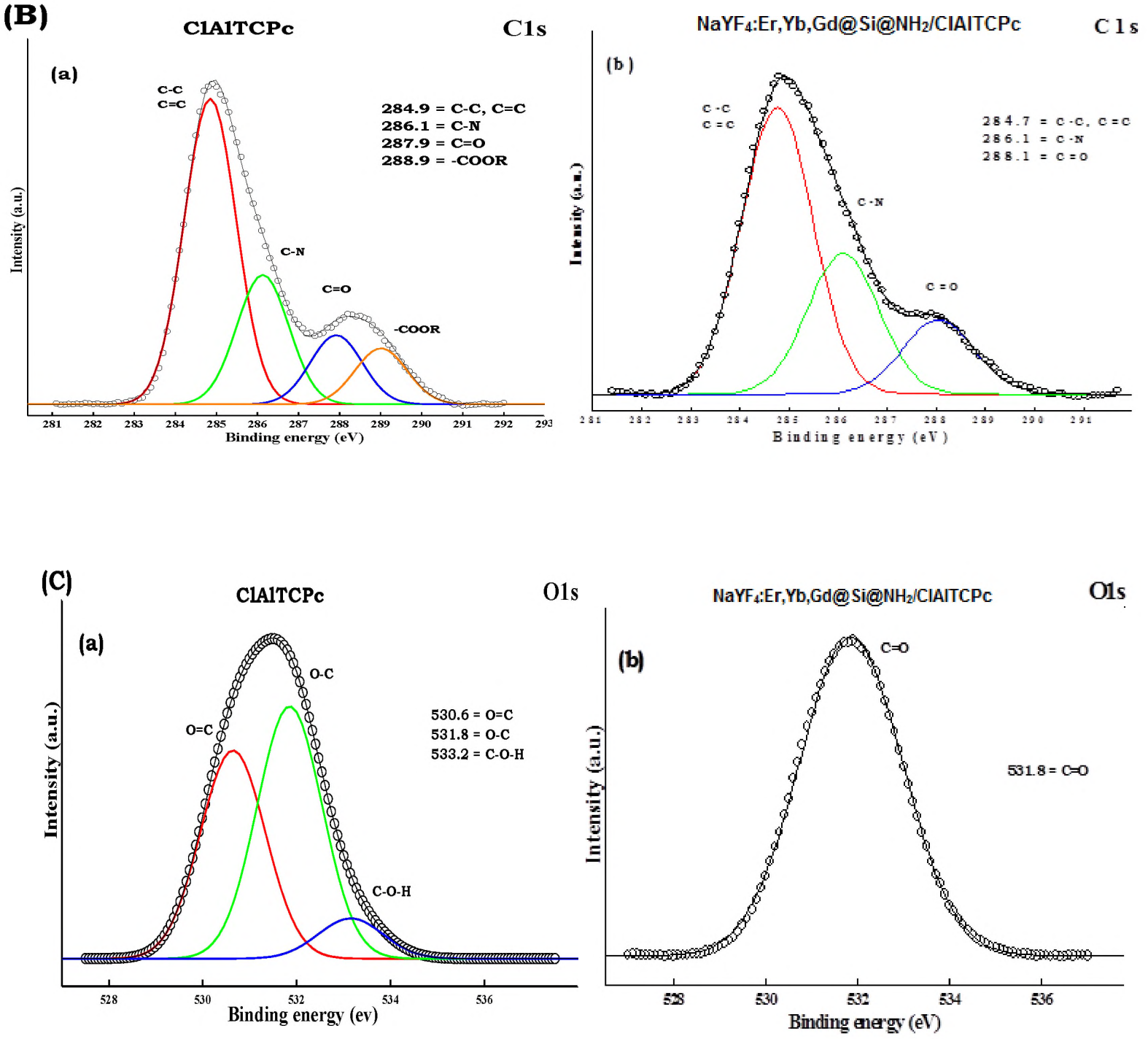

Figure 3.18: High resolution XPS spectra for ClAlTCPc and its conjugates. (A) N1s, (B) C1s and (C) O1s. For (A): (a) UNCPs alone, (b) ClAlTCPc alone and (c) $NaYF_4$:Yb/Er/Gd@Si@NH_2/ClAlTCPc. For (B) and (C) (a) ClAlTCPc alone and (b) $NaYF_4$:Yb/Er/Gd@Si@NH_2/ClAlTCPc

Deconvoluted high resolution N1s XPS spectra for native $NaYF_4$:Yb/Er/Gd@Si@NH_2 UCNPs alone gave binding energies at 398.6 and 400.7 eV belonging to NH_2 and NH^{3+}, respectively, Fig. 3.18A (a) [126–128]. ClAlTCPc showed peaks at 398.6, 399.9 and 400.1 eV corresponding to C-N, Al-N and C=N respectively, Fig 3.18A (b). Once conjugated to $NaYF_4$:Yb/Er/Gd@Si@NH_2/ClAlTCPc, there was a disappearance of the NH_2 peak of the native $NaYF_4$:Yb/Er/Gd@Si@NH_2 UCNPs alone and the appearance of the N-C=O peak a 402.5 eV which is what was expected as a result of the amide bond formation Fig. 3.18A (c). The C1s spectra for ClAlTCPc alone exhibits the carbonyl peak at 288.9 eV (Fig. 3.18B (a) and it disappears after conjugation Fig. 3.18B (b)) [127,129].

Fig. 3.18C (a), O1S, shows 3 types of bonds on the Pc, the O-C, O-H and the O=C [130]. Once conjugated the O-H and O-C disappear only the O=C, Fig. 3.18C (b) was left.

3.3.4.2 ClAlTSPc

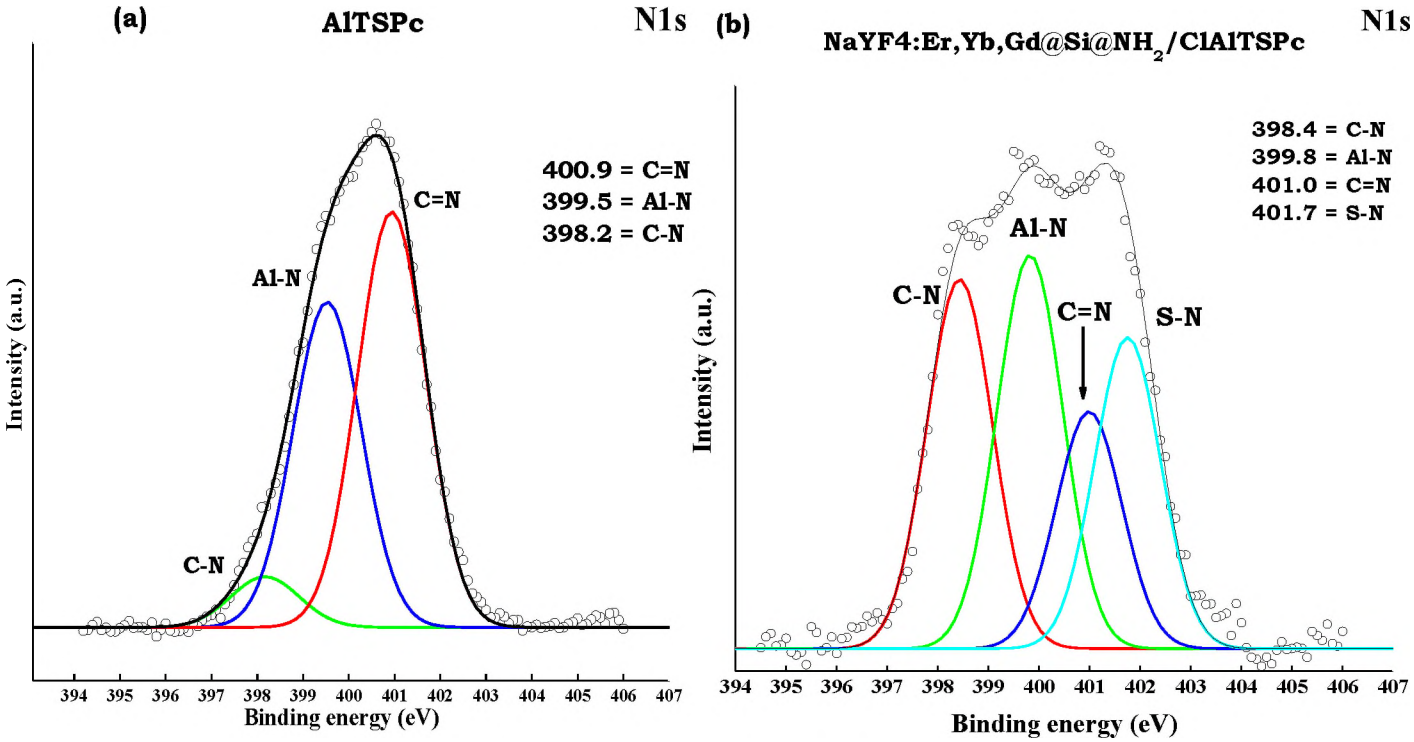

Figure 3.19: High resolution N 1S XPS spectra for (a) ClAlTSPc and (b) NaYF4:Er,Yb,Gd@Si@NH2/ClAlTSPc

Figure 3.19 (a) shows the high resolution deconvoluted N1s for ClAlTSPc, the C-N bond is observed at 398.2 eV, the Al-C at 399.5 eV and the C=N bond at 400.9 eV [131]. After conjugation Fig. 3.19b shows the same peaks but with the addition of the S-N peak at 401.7 eV due to the sulphonamide bond, hence confirming conjugation.

3.3.5. UV-Vis spectra for ClAlTSPc and ClAlTCPc.

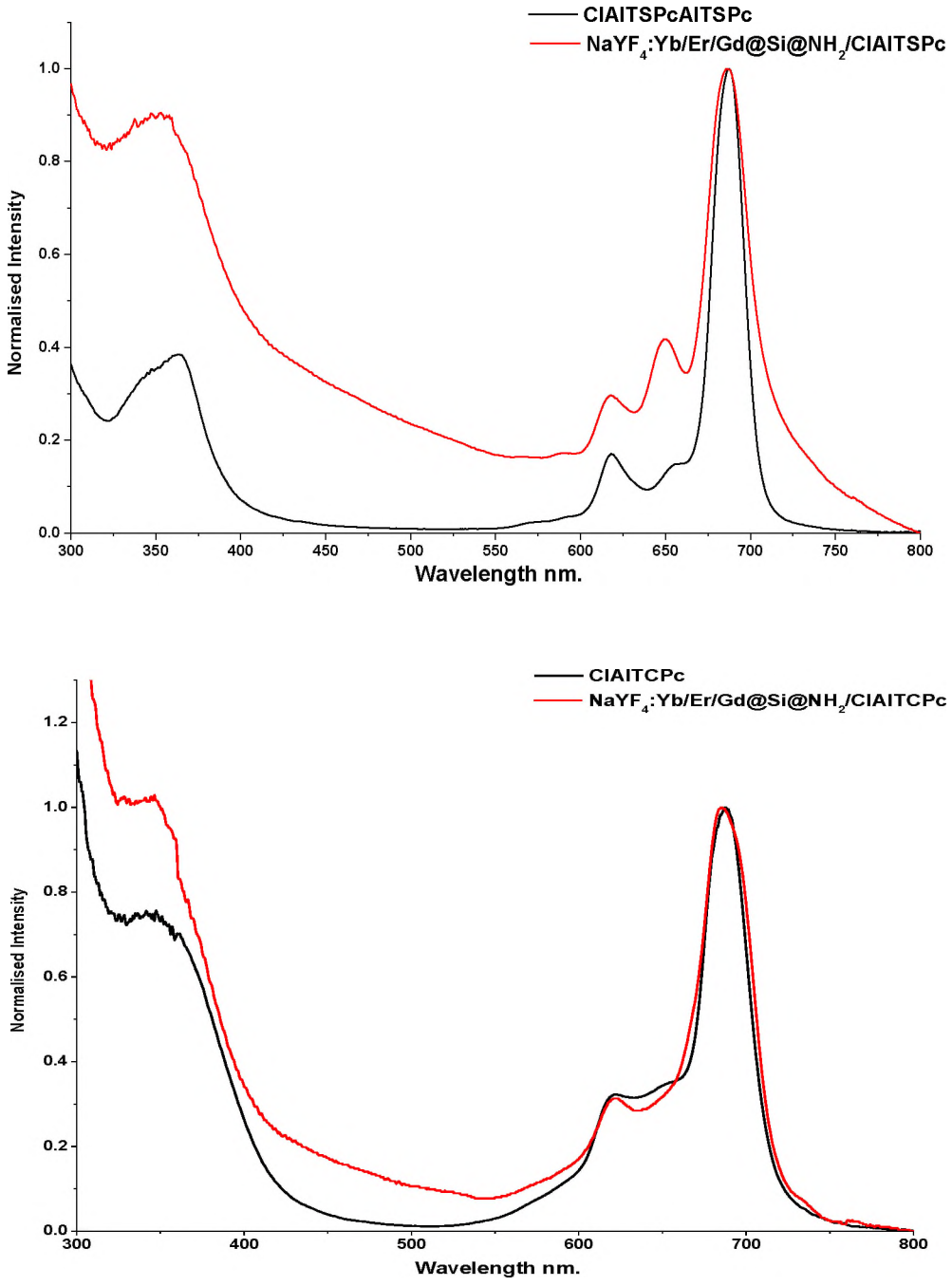

Figure 3.20: UV-Vis absorption spectra for (A) the ClAlTSPc and (B) ClAlTCPc alone and when conjugated to $NaYF_4$:Yb/Er/Gd@Si@NH_2 UCNPs. Solvent = DMSO.

The absorption spectra for ClAlTSPc showed a monomeric behaviour with a narrow Q band before conjugation, Fig. 3.20A. There was broadening following conjugation, most likely due to the colloidal nature of the conjugate. The spectrum for ClAlTCPc shows some aggregation before conjugation, Fig. 3.20B. The so called "H" aggregation in phthalocyanines is evidenced by a broad (or split) Q band with peaks due to the aggregate at higher energy than those of the monomer peak near 630 nm [121]. A broad non-vibronic peak is observed near 630 nm for ClAlTCPc alone in Fig. 3.20B, due to aggregation.

3.3.6. FRET Studies

Due to the lack of reproducibility of the fluorescence in solution, Fig 3.7, the samples were each run 20 times successively and overall displayed the trend seen in Fig 3.21. The spectra of all twenty runs were averaged out and yielded smoother and uniform peak shapes, Fig 3.21. There is the disappearance of a peak at 755 nm, Fig 3.11, this is due to the UCNP being embedded in polystyrene fibre, which as mentioned before stabilizes the nanoparticles. The stabilization allows for the relaxation of electrons from a different energy level lower down on the energy level diagram, Fig 1.8.

FRET studies in this work were for MPcs linked to UCNPs, not mixed as in Section 3.2.3.3. If any FRET occurs, we expect the intensity of the red emission peak of the UCNPs to decrease, this is observed in Fig. 3.21. The decrease in the peak at 658 nm is clearly demonstrated for both ClAlTSPc and ClAlTCPc. There is no change in the 544 nm emission of the UCNPs where there is no overlap with the Pcs, Fig 3.12. This shows that FRET occurs by transfer of energy from the 658 nm emission of UCNPs to the Pcs.

Two mechanisms have been reported to be responsible for the quenching of emission from the nanoparticles, they are FRET and emission reabsorption [132,133]. The latter

involves quenching of the fluorescence as a result of the light emitted from the UCNP being absorbed by a chromophore in close proximity but not anchored on it. Since in this work the UCNPs are linked to the Pcs, it is suggested that FRET is the major mechanism.

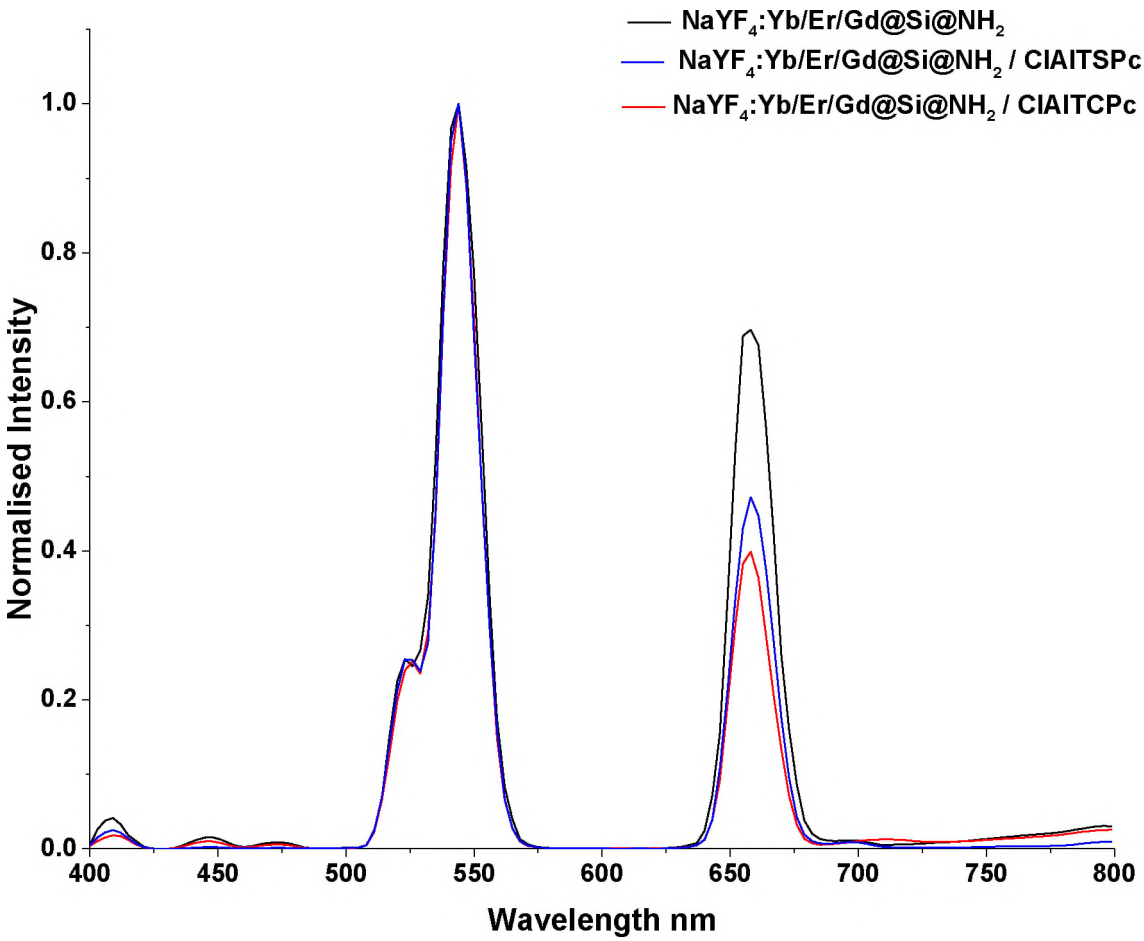

Figure 3.21: Fluorescence emission profiles of $NaYF_4$:Yb/Er/Gd@Si@NH_2 and its ClAlTSPc and ClAlTCPc conjugates in DMSO.

There is a decrease in fluorescence lifetimes (Table 3.3, Fig. 3.22) for the conjugates compared to $NaYF_4$:Yb/Er/Gd@Si@NH_2 alone due to FRET. The decrease in luminescence lifetimes of the UCNP in the conjugate when compared to $NaYF_4$:Yb/Er/Gd@Si@NH_2 UCNPs alone may also be due to the presence of additional relaxation pathways induced by the phthalocyanines [133].

Table 3.3: Fluorescence lifetimes for the 658 nm emission of the UCNPs alone and when conjugated to ClAlTSPc or ClAlTCPc; and FRET efficiency of the conjugates in DMSO

Nanoparticle	τ_F (ms)	Error	χ^2	*Eff*
$NaYF_4$:Yb/Er/Gd@Si@NH_2	0.596	± 0.055	0.981	
NaYF4:Yb/Er/Gd@Si@NH_2/ClAlTSPc	0.491	± 0.017	0.961	0.18
NaYF4:Yb/Er/Gd@Si@NH_2/ClAlTCPc	0.471	± 0.073	0.957	0.21

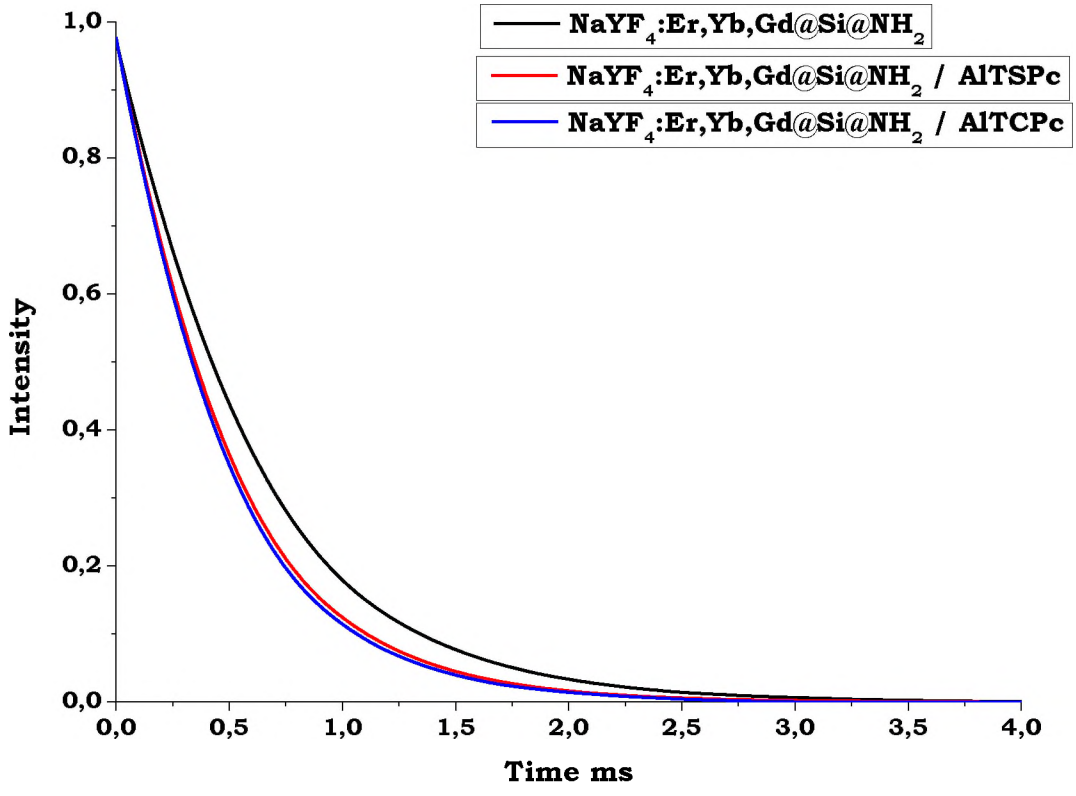

Figure 3.22: Fluorescence lifetimes for the 658 nm emission from the $NaYF_4$:Er,Yb,Gd@Si@NH_2 nano particles, $NaYF_4$:Er,Yb,Gd@Si@NH_2/ClAlTSPc and $NaYF_4$:Er,Yb,Gd@Si@NH_2/ClAlTCPc in DMSO.

FRET efficiencies (*Eff*) may be quantified from the fluorescence lifetimes of the donor in the absence ($\tau_{F(UCNP)}$) and the presence ($\tau_{F(UCNP)}^{linked}$) of the acceptor, using Eq. 1.2 [69].

Low FRET efficiencies (18 and 21%) were observed even though there was a good spectral overlap between the 658 nm emission of UCNPs and the absorption spectra of the Pcs. The FRET efficiency of 18% for ClAlTSPc linked to UCNPs is lower than when the two were physically mixed i.e. not covalently bonded and in which case the efficiency was 28%, see Table 3.2. This is surprising since the energy transfer efficiency is distance dependent, and it should be enhanced when the Pc is chemically linked to the UCNPs (as is the case here) as opposed to the two just physically mixed (as was the case earlier).

FRET efficiency may also be affected by the orientation of the donor and acceptor, with parallel efficiency resulting in more efficient FRET when compared to perpendicular orientation. Another possibility is the concentration or amount of Ps per nano particle may be larger for the mixed studies than that of the linked. The linked may only have a few Pcs attached while in solution the entire UCNP could be surrounded by Pcs affecting the *Eff* measured.

3.7 Conclusion

The results presented above show that although upconversion nanoparticles (UCNPs) were synthesised and their surfaces successfully modified, they were plagued by erratic and unstable fluorescence emissions in solution. In order to overcome this the various modified UCNPs were embedded in polystyrene electrospun nano fibres (PS). The fluorescence was stabilised across all variations. The uncapped and NH_2 functionalised UCNPs, although stable, suffered poor fluorescence emissions as a result from surface interactions which increased the particles phonon energies. UCNPs, although incredibly versatile, are limited thanks to these non radiative internal energy transfers. Greater understanding and further exploration of these materials are required before lanthanide upconversion materials can really make an impact. The polymer stabilised $NaYF_4$:Yb/Er/Gd@Si/Ps showed a relative decrease in fluorescence lifetimes and fluorescence emissions for the 658 nm when the electrospun fibres were suspended in a dimethyl sulfoxide (DMSO) solution of the chloro-aluminium tetrasulfo phthalocyanine (ClAlTSPc). Förster resonance energy transfer (FRET) between the UCNPs in fibre and ClAlTSPc was approximated and confirmed by the degradation of a singlet oxygen quencher DPBF when irradiated by near infrared (NIR) light. The conjugation, chemical linking, of $NaYF_4$:Yb/Er/Gd@Si@NH_2 and ClAlTSPc, as well as chloro-aluminium tetracarboxy phthalocyanine (ClAlTCPc) for comparison, was confirmed with X-ray photoelectron spectroscopy (XPS) and FTIR spectroscopy. The link for the ClAlTSPc and ClAlTCPc was through sulfonamide and amide bonds respectively. The 658 nm fluorescence emissions and fluorescence lifetimes for the conjugates decreased when compared to the UCNP alone, more so for the ClAlTCPc than the ClAlTSPc. These results are a

promising indication that the conjugates may generate singlet oxygen when irradiated by NIR light and have potential as PDT agents.

References

[1] N.B. McKeown, Phthalocyanine materials: synthesis, structure, and function, Cambridge University Press, New York, 1998.

[2] W. Herbst, K. Hunger, G. Wilker, R. Ohleier, Heinfred; Winter, Industrial Organic Pigments, Wiley-VCH Verlag GmbH & Co. KGaA, Weinheim, FRG, 2004.

[3] P. Gregory, The Chemistry and Application of Dyes, Springer US, Boston, MA, 1990.

[4] P. Matlaba, T. Nyokong, Synthesis, electrochemical and photochemical properties of unsymmetrically substituted zinc phthalocyanine complexes, Polyhedron, 21 (2002) 2463–2472.

[5] E.A. Lukyanets, V.N. Nemykin, The key role of peripheral substituents in the chemistry of phthalocyanines and their analogs, J. Porphyr. Phthalocyanines. 14 (2010) 1–40.

[6] V.N. Nemykina, E. a. Lukyanets, Synthesis of substituted phthalocyanines, Arkivoc. 2010 (2010) 136.

[7] N. Sekkat, H. Van Den Bergh, T. Nyokong, N. Lange, Like a bolt from the blue: Phthalocyanines in biomedical optics, Molecules. 17 (2012) 98–144.

[8] J.D. Spikes, Phthalocyanines as photosensitizers in biological systems and for the photodynamic therapy of tumors, Photochem. Photobiol. 43 (1986) 691–699.

[9] A. Ivaturi, S.K.W. MacDougall, R. Martín-RodríguezI, M. Quintanilla, J. Marques-Hueso, K.W. Krämer, A. Meijerink, B. S. Richards, Optimizing infrared to near infrared upconversion quantum yield of β-$NaYF_4$:Er^{3+} in fluoropolymer matrix for photovoltaic devices, J. Appl. Phys. 114 (2013) 013505.

[10] M. Ambroz, A. MacRobert, J. Morgan, G. Rumbles, M.S.C. Foley, D. Phillips, Time-resolved fluorescence spectroscopy and intracellular imaging of disulphonated aluminium phthalocyanine, J. Photochem. Photobiol. B. 22 (1994) 105–117.

[11] H.L. Lu, W.J. Syu, N. Nishiyama, K. Kataoka, P.S. Lai, Dendrimer phthalocyanine-encapsulated polymeric micelle-mediated photochemical internalization extends the efficacy of photodynamic therapy and overcomes drug-resistance in vivo, J. Control. Release. 155 (2011) 458–464.

[12] V. Iliev, Phthalocyanine-modified titania - Catalyst for photooxidation of phenols by irradiation with visible light, J. Photochem. Photobiol. A Chem. 151 (2002) 195–199.

[13] M. Wainwright, Photodynamic antimicrobial chemotherapy (PACT), J. Antimicrob. Chemother. 42 (1998) 13–28.

[14] P. Skladal, M. Mascini, Sensitive detection of pesticides using amperometric

sensors based on cobalt phthalocyanine-modified composite electrodes and immobilized cholinesterases, Biosens. Bioelectron. 7 (1992) 335–343.

[15] S.M. O'Flaherty, S. V. Hold, M.J. Cook, T. Torres, Y. Chen, M. Hanack, W. J. Blau, Adv. Mater. 15 (2003) 19–32.

[16] W. Huang, J. Sinha, M.L. Yeh, J.F.M. Hardigree, R. LeCover, K. Besar, A. M. Rule, P. N. Breysse, H. E. Katz, Diverse organic field-effect transistor sensor responses from two functionalized naphthalenetetracarboxylic diimides and copper phthalocyanine semiconductors distinguishable over a wide analyte range, Adv. Funct. Mater. 23 (2013) 4094–4104.

[17] M. Bejar, M. Liras, NIR excitation of upconversion nanohybrids containing a surface grafted Bodipy induces oxygen-mediated cancer cell death, Journal Mater. Chem. B. (2014) 1–19.

[18] J. Taylor, C. Litwinski, T. Nyokong, E. Antunes, Fluorescence Behaviour of an Aluminium Octacarboxy Phthalocyanine - $NaYGdF_4$:Yb/Er Nanoparticle Conjugate, J. Fluoresc. 25 (2015) 489–501.

[19] M. Durmuş, T. Nyokong, Synthesis, photophysical and photochemical properties of aryloxy tetra-substituted gallium and indium phthalocyanine derivatives, Tetrahedron. 63 (2007) 1385–1394.

[20] X.Y. Li, X. He, A.C.H. Ng, C. Wu, D.K.P. Ng, Influence of surfactants on the aggregation behavior of water-soluble dendritic phthalocyanines, Macromolecules. 33 (2000) 2119–2123.

[21] V. V Sokolov, V.I. Chissov, R.I. Yakubovskaya, E.I. Aristarkhova, E. V Filonenko, T.A. Belous, G. N. Vorozhtsov, N. N. Zharkova, V. V. Smirnov, M. B. Zhitkova, Photodynamic therapy (PDT) of malignant tumors by photosensitzer photosens: results of 45 clinical cases, in: B. Ehrenberg, G. Jori, J. Moan (Eds.), 1996: pp. 281–287.

[22] M. Ambroz, a Beeby, a J. MacRobert, M.S. Simpson, R.K. Svensen, D. Phillips, Preparative, analytical and fluorescence spectroscopic studies of sulphonated aluminium phthalocyanine photosensitizers., J. Photochem. Photobiol. B. 9 (1991) 87–95.

[23] V.T. Verdree, S. Pakhomov, G. Su, M.W. Allen, A.C. Countryman, R.P. Hammer, S. a. Soper, Water soluble metallo-phthalocyanines: The role of the functional groups on the spectral and photophysical properties, J. Fluoresc. 17 (2007) 547–563.

[24] R.M. Negri, A. Zalts, E.A. Roman, P.F. Aramendia, S.E. Braslavsky, Carboxylated zinc-phthalocyanine, influence of dimerization on the spectroscopic properties. an Absorption, emission, and thermal lensing study, Photochem. Photobiol. 53 (1991) 317–322.

[25] P. Modisha, E. Antunes, T. Nyokong, Photophysical properties of zinc tetracarboxy phthalocyanines conjugated to magnetic nanoparticles, J. Nanosci. Nanotechnol. 15 (2015) 3688–3696.

[26] D.O. Oluwole, J. Britton, P. Mashazi, T. Nyokong, Synthesis and photophysical properties of nanocomposites of aluminum tetrasulfonated phthalocyanine covalently linked to glutathione capped CdTe/CdS/ZnS quantum dots, Synth.

Met. 205 (2015) 212–221.

[27] Y. Rio, M. Salomé Rodríguez-Morgade, T. Torres, Modulating the electronic properties of porphyrinoids: a voyage from the violet to the infrared regions of the electromagnetic spectrum, Org. Biomol. Chem. 6 (2008) 1877.

[28] R. Bonnett, Chemical Aspects of Photodynamic Therapy, CRC Press, 2000.

[29] M.P. De Filippis, D. Dei, L. Fantetti, G. Roncucci, Synthesis of a new water-soluble octa-cationic phthalocyanine derivative for PDT, Tetrahedron Lett. 41 (2000) 9143–9147.

[30] S. Swavey, M. Tran, Porphyrin and phthalocyanine photosensitizers as PDT agents : A new modality for the treatment of melanoma, Recent Adv. Biol. Ther. Manag. Melanoma. (2013) 253–282.

[31] B.P. Joshi, T.D. Wang, Exogenous Molecular Probes for Targeted Imaging in Cancer: Focus on Multi-modal Imaging, Cancers (Basel). 2 (2010) 1251–1288.

[32] F. Chen, S. Zhang, W. Bu, Y. Chen, Q. Xiao, J. Liu, H. Xing, L. Zhou, W. Peng, A uniform sub-50 nm-sized magnetic/upconversion fluorescent bimodal imaging agent capable of generating singlet oxygen by using a 980 nm laser., Chem. - Eur. J.. 18 (2012) 7082–90.

[33] D.K. Chatterjee, L.S. Fong, Y. Zhang, Nanoparticles in photodynamic therapy: an emerging paradigm., Adv. Drug Deliv. Rev. 60 (2008) 1627–37.

[34] E. Panzarini, V. Inguscio, L. Dini, Overview of cell death mechanisms induced by rose bengal acetate-photodynamic therapy, Int. J. Photoenergy. 2011 (2011) 1–11.

[35] V.S. Shivashankara, R. Yogananda, D.R. Bharathi, A review on nanoparticles applications in different drug delivery systems, Am. J. PharmTech Res. 2 (2012) 163–176.

[36] W.T. Liu, Nanoparticles and their biological and environmental applications, J. Biosci. Bioeng. 102 (2006) 1–7.

[37] V.J. Mohanraj, Y. Chen, Nanoparticles – A Review, Trop. J. Pharm. Res. 5 (2006) 561–573.

[38] Z. Chen, H. Chen, H. Hu, M. Yu, F. Li, Q. Zhang, Z. Zhou, T. Yi, C. Huang, Versatile synthesis strategy for carboxylic acid-functionalized upconverting nanophosphors as biological labels., J. Am. Chem. Soc. 130 (2008) 3023–9.

[39] J. Jin, Y. Gu, C.W. Man, J. Cheng, Z. Xu, Y. Zhang, et al., Polymer-coated $NaYF_4$:Yb^{3+}, Er^{3+} upconversion nanoparticles for charge-dependent cellular imaging., ACS Nano. 5 (2011) 7838–47.

[40] M. Wang, Z. Chen, W. Zheng, H. Zhu, S. Lu, E. Ma, D. Tu, S. Zhou, Shanyong M. Huang, X. Chen, Lanthanide-doped upconversion nanoparticles electrostatically coupled with photosensitizers for near-infrared-triggered photodynamic therapy., Nanoscale. 6 (2014) 8274–8282.

[41] H.X. Mai, Y.W. Zhang, L.D. Sun, C.H. Yan, Size- and phase-controlled synthesis of monodisperse $NaYF_4$:Yb,Er nanocrystals from a unique delayed nucleation pathway monitored with upconversion spectroscopy, J. Phys. Chem. C. 111

(2007) 13730–13739.

[42] H. Dong, L.-D. Sun, C.-H. Yan, Basic understanding of the lanthanide related upconversion emissions., Nanoscale. 5 (2013) 5703–14.

[43] H. Wang, Y. Liu, M. Li, H. Huang, H.M. Xu, R.J. Hong, H. Shen, Multifunctional TiO_2 nanowires-modified nanoparticles bilayer film for 3D dye-sensitized solar cells, Optoelectron. Adv. Mater. Rapid Commun. 4 (2010) 1166–1169.

[44] X. Zhang, Z. Zhao, X. Zhang, D.B. Cordes, B. Weeks, B. Qiu, K. Madanan, D. Sardar, J. Chaudhuri, Magnetic and optical properties of $NaGdF_4$:Nd^{3+}, Yb^{3+}, Tm^{3+} nanocrystals with upconversion/downconversion luminescence from visible to the near-infrared second window, Nano Res. 8 (2015) 636–648.

[45] X. Li, J. Zhu, Z. Man, Y. Ao, H. Chen, Investigation on the structure and upconversion fluorescence of Yb^{3+}/Ho^{3+} co-doped fluorapatite crystals for potential biomedical applications., Sci. Rep. 4 (2014) 4446.

[46] Q. Liu, W. Feng, T. Yang, T. Yi, F. Li, Upconversion luminescence imaging of cells and small animals., Nat. Protoc. 8 (2013) 2033–44.

[47] J. Zhang, C. Cao, S. Lu, W. Qin, Energy transition between Y b^{3+} - Tm^{3+} - Gd^{3+} in Gd^{3+}, Y b^{3+} and Tm^{3+} Co-doped fluoride nanocrystals, Phys. Procedia. 13 (2011) 9–13.

[48] F. Auzel, Compteur quantique par transfert d'energie de Yb $^{3+}$ ` aTm $^{3+}$ dans un tungstate mixte et dans un verre germanate, C.R. Acad. Sci. 262 (1966) 819–821.

[49] P. Zhang, W. Steelant, M. Kumar, M. Scholfield, Versatile photosensitizers for photodynamic therapy at infrared excitation, J. Am. Chem. Soc. 129 (2007) 4526–4527.

[50] D.K. Chatterjee, Z. Yong, Upconverting nanoparticles as nanotransducers for photodynamic therapy in cancer cells., Nanomedicine. 3 (2008) 73–82.

[51] M. Kamimura, D. Miyamoto, Y. Saito, K. Soga, Y. Nagasaki, Design of poly(ethylene glycol)/streptavidin coimmobilized upconversion nanophosphors and their application to fluorescence biolabeling, Langmuir. 24 (2008) 8864–8870.

[52] H.S. Qian, H.C. Guo, P.C. Ho, R. Mahendran, Y. Zhang, Mesoporous-silica-coated up-conversion fluorescent nanoparticles for photodynamic therapy., Small. 5 (2009) 2285–90.

[53] H. Guo, H. Qian, N.M. Idris, Y. Zhang, Singlet oxygen-induced apoptosis of cancer cells using upconversion fluorescent nanoparticles as a carrier of photosensitizer., Nanomedicine. 6 (2010) 486–95.

[54] C. Wang, L. Cheng, Z. Liu, Upconversion nanoparticles for photodynamic therapy and other cancer therapeutics, Theranostics. 3 (2013) 317–330.

[55] J. Shan, S.J. Budijono, G. Hu, N. Yao, Y. Kang, Y. Ju, Pegylated composite nanoparticles containing upconverting phosphors and meso-tetraphenyl porphine (TPP) for photodynamic therapy, Adv. Funct. Mater. 21 (2011) 2488–2495.

[56] N.M. Idris, M.K. Gnanasammandhan, J. Zhang, P.C. Ho, R. Mahendran, Y.

Zhang, In vivo photodynamic therapy using upconversion nanoparticles as remote-controlled nanotransducers, Nat. Med. 18 (2012) 1580–1585.

[57] Z. Zhao, Y. Han, C. Lin, D. Hu, F. Wang, X. Chen, Z. Chen, N. Zheng, Multifunctional core-shell upconverting nanoparticles for imaging and photodynamic therapy of liver cancer cells, Chem. - An Asian J. 7 (2012) 830–837.

[58] X. Qiao, J. Zhou, J. Xiao, Y. Wang, L. Sun, C. Yan, Triple-functional core–shell structured upconversion luminescent nanoparticles covalently grafted with photosensitizer for luminescent, magnetic resonance imaging and photodynamic therapy in vitro, Nanoscale. 4 (2012) 4611.

[59] A. Zhou, Y. Wei, B. Wu, Q. Chen, D. Xing, Pyropheophorbide A and c(RGDyK) comodified chitosan-wrapped upconversion nanoparticle for targeted near-infrared photodynamic therapy, Mol. Pharm. 9 (2012) 1580–1589.

[60] F. Chen, S. Zhang, W. Bu, Y. Chen, Q. Xiao, J. Liu, H. Xing, L. Zhou, W. Peng, J. Shi, A uniform sub-50nm-sized magnetic/upconversion fluorescent bimodal imaging agent capable of generating singlet oxygen by using a 980nm laser, Chem. - A Eur. J. 18 (2012) 7082–7090.

[61] Y. Wang, H. Wang, D. Liu, S. Song, X. Wang, H. Zhang, Graphene oxide covalently grafted upconversion nanoparticles for combined NIR mediated imaging and photothermal/photodynamic cancer therapy, Biomaterials. 34 (2013) 7715–7724.

[62] G. Tian, W. Ren, L. Yan, S. Jian, Z. Gu, L. Zhou, S. Jin, W. Yin, S. Li, Y. Zhao, Red-emitting upconverting nanoparticles for photodynamic therapy in cancer cells under near-infrared excitation, Small. 9 (2013) 1929–1938.

[63] L. Xia, X. Kong, X. Liu, L. Tu, Y. Zhang, Y. Chang, et al., An upconversion nanoparticle - Zinc phthalocyanine based nanophotosensitizer for photodynamic therapy, Biomaterials. 35 (2014) 4146–4156.

[64] H.J. Wang, R. Shrestha, Y. Zhang, Encapsulation of photosensitizers and upconversion nanocrystals in lipid micelles for photodynamic therapy, Part. Part. Syst. Charact. 31 (2014) 228–235.

[65] K. Nigoghossian, M.F.S. Peres, F.L. Primo, A.C. Tedesco, E. Pecoraro, Y. Messaddeq, S.J.L. Ribeiro, Infrared to Visible Up-conversion in Biocellulose–yttrium Vanadate Nanoparticle Composite Membranes. Demonstration of Chloroaluminum Phthalocyanine Light Emission Under Up-converted Light Excitation, Colloids Interface Sci. Commun. 2 (2014) 6–10.

[66] F. Ai, Q. Ju, X. Zhang, X. Chen, F. Wang, G. Zhu, A core-shell-shell nanoplatform upconverting near-infrared light at 808 nm for luminescence imaging and photodynamic therapy of cancer, Sci. Rep. 5 (2015) 10785.

[67] O.S. Wolfbeis, An overview of nanoparticles commonly used in fluorescent bioimaging., Chem. Soc. Rev. 44 (2015) 4743–4768.

[68] L. Stryer, Fluorescence energy transfer as a spectroscopic ruler, Ann. Rev. Biochem. 47 (1978) 819–846.

[69] J.R. Lakowicz, Principles of Fluorescence Spectroscopy, 3rd ed., Springer

Science & Business Media, New York, 2007.

[70] J.S. Hsiao, B.P. Krueger, R.W. Wagner, T.E. Johnson, J.K. Delaney, D.C. Mauzerall, G. R. Fleming, J. S. Lindsey, D. F. Bocian, R. J. Donohoe, Soluble synthetic multiporphyrin arrays. 2. Photodynamics of energy-transfer processes, J. Am. Chem. Soc. 118 (1996) 11181–11193.

[71] T.C. Mokhena, A review on electrospun bio-based polymers for water treatment, Express Polym. Lett. 9 (2015) 839–880.

[72] G. Gong, J. Wu, L. Jiang, Novel polyimide materials produced by electrospinning, Prog. Chem. 23 (2011) 750–759.

[73] J.-W. Jung, C.-L. Lee, S. Yu, I.-D. Kim, Electrospun nanofibers as a platform for advanced secondary batteries: A comprehensive review, J. Mater. Chem. A. (2015).

[74] A. Formhals, Process and apparatus for preparing artificial threads, (1934).

[75] Z.M. Huang, Y.Z. Zhang, M. Kotaki, S. Ramakrishna, A review on polymer nanofibers by electrospinning and their applications in nanocomposites, Compos. Sci. Technol. 63 (2003) 2223–2253.

[76] S. Agarwal, J.H. Wendorff, A. Greiner, Use of electrospinning technique for biomedical applications, Polymer (Guildf). 49 (2008) 5603–5621.

[77] Q. Ma, J. Wang, X. Dong, W. Yu, G. Liu, Electrospinning fabrication and characterization of magnetic-upconversion fluorescent bifunctional core–shell nanofibers, J. Nanoparticle Res. 16 (2014) 2239.

M. Park, H. Kim, S. Lee, S. Park, Electrospun ZnO hybrid nanofibers for photodegradation of wastewater containing organic dyes: A review, J. Ind. Eng. Chem. 21 (2015) 26–35.

[79] F. Li, Y. Zhao, Y. Song, Core-Shell Nanofibers : Nano Channel and Capsule by Coaxial Electrospinning, in: A. Kumar (Ed.), Core-Shell Nanofibers Nano Channel Capsul. by Coaxial Electrospinning, InTech, 2010: pp. 419–438.

[80] Ş. Sİrİn, S. Çetİner, A.S. Saraç, Elektro Çekim Yoluyla Polimer Nanolifler : Nanolif Kalitesini Etkileyen Faktörler Polymer Nanofibers Via Electrospinning : Factors Affecting Nanofiber Quality, KSU. J. Eng. Sci. 16 (2013) 1–12.

[81] Z. Pan, S.H. Morgan, a. Loper, V. King, B.H. Long, W.E. Collins, Infrared to visible upconversion in Er^{3+}-doped-lead-germanate glass: effects of Er^{3+} ion concentration, J. Appl. Phys. 77 (1995) 4688–4692.

[82] C.B. De Araújo, L.S. Menezes, G.S. Maciel, L.H. Acioli, A.S.L. Gomes, Y. Messaddeq, Infrared-to-visible CW frequency upconversion in Er^{3+}-doped fluoroindate glasses, Appl. Phys. Lett. 602 (1995) 602.

[83] S. Sivakumar, F.C.J.M. van Veggel, M. Raudsepp, Bright white light through up-conversion of a single NIR source from sol-gel-derived thin film made with Ln^{3+}-doped LaF_3 nanoparticles., J. Am. Chem. Soc. 127 (2005) 12464–5.

[84] F. Liu, E. Ma, D. Chen, Y. Yu, Y. Wang, Tunable red-green upconversion luminescence in novel transparent glass ceramics containing Er: $NaYF_4$ nanocrystals., J. Phys. Chem. B. 110 (2006) 20843–6.

[85] G. Wang, S. Dai, J. Zhang, L. Wen, J. Yang, Z. Jiang, Intense upconversion luminescence and effect of local environment for Tm^{3+}/Yb^{3+} co-doped novel TeO_2-$BiCl_3$ glass system, Spectrochim. Acta Part A. Mol. Biomol. Spectrosc. 64 (2006) 349–354.

[86] S. Sivakumar, F.C.J.M. Van Veggel, P.S. May, Near-infrared (NIR) to red and green up-conversion emission from silica sol-gel thin films made with $La_{0.45}Yb_{0.50}Er_{0.05}F_3$ nanoparticles, hetero-looping-enhanced energy transfer (hetero-LEET): A new up-conversion process, J. Am. Chem. Soc. 129 (2007) 620–625.

[87] D.M. da Silva, L.R.P. Kassab, S.R. Lüthi, C.B. de Araújo, A.S.L. Gomes, M.J.V. Bell, Frequency upconversion in Er^{3+} doped PbO–GeO_2 glasses containing metallic nanoparticles, Appl. Phys. Lett. 90 (2007) 081913.

[88] L.R.P. Kassab, F. a Bomfim, J.R. Martinelli, N.U. Wetter, J.J. Neto, C.B. Araújo, Energy transfer and frequency upconversion in Yb^{3+}–Er^{3}+-doped PbO-GeO_2 glass containing silver nanoparticles, Appl. Phys. B. 94 (2008) 239–242.

[89] B. Dong, H. Song, H. Yu, H. Zhang, R. Qin, X. Bai, G. Pan, S. Lu, F. Wang, L. Fan, Q. Dai, Upconversion Properties of Ln^{3+} Doped $NaYF_4$/Polymer Composite Fibers Prepared by Electrospinning, J. Phys. Chem. C. 112 (2008) 1435–1440.

[90] G. Dong, X. Liu, X. Xiao, B. Qian, J. Ruan, H. Yang, S. Ye, D. Chen, J. Qiu, Upconversion Luminescence of Er^{3+}–Yb^{3+} Codoped $NayF_4$-Pvp Electrospun Nanofibers, Photonics Technol. Lett. 21 (2009) 57 – 59.

[91] S.K. Singh, N.K. Giri, D.K. Rai, S.B. Rai, Enhanced upconversion emission in Er^{3+}-doped tellurite glass containing silver nanoparticles, Solid State Sci. 12 (2010) 1480–1483.

[92] F. a. Bomfim, J.R. Martinelli, L.R.P. Kassab, T.A.A. Assumpção, C.B. De Araújo, Infrared-to-visible upconversion in Yb^{3+}/Er^{3+} co-doped PbO-GeO_2 glass with silver nanoparticles, J. Non. Cryst. Solids. 356 (2010) 2598–2601.

[93] Y. Wu, X. Shen, S. Dai, Y. Xu, F. Chen, C. Lin, Silver Nanoparticles Enhanced Upconversion Luminescence in Er^{3+}/ Yb^{3+} Codoped Bismuth-Germanate Glasses, J. Phys. Chem. (2011) 25040–25045.

[94] R.J. Amjad, M.R. Sahar, S.K. Ghoshal, M.R. Dousti, S. Riaz, B.A. Tahir, Enhanced infrared to visible upconversion emission in Er^{3+} doped phosphate glass: Role of silver nanoparticles, J. Lumin. 132 (2012) 2714–2718.

[95] M. Reza Dousti, M.R. Sahar, R.J. Amjad, S.K. Ghoshal, A. Khorramnazari, A. Dordizadeh Basirabad, et al., Enhanced frequency upconversion in Er^{3+}-doped sodium lead tellurite glass containing silver nanoparticles, Eur. Phys. J. D. 66 (2012) 1–6.

[96] B. Yan, J.C. Boyer, D. Habault, N.R. Branda, Y. Zhao, Near infrared light triggered release of biomacromolecules from hydrogels loaded with upconversion nanoparticles, J. Am. Chem. Soc. 134 (2012) 16558–16561.

[97] Y. Bao, Q. Luu, Y. Zhao, H. Fong, P. May, C. Jiang, Upconversion polymeric nanofibers containing lanthanide-doped nanoparticles via electrospinning, Nanoscale. 4 (2012) 7369–75.

[98] P. Zou, X. Hong, Y. Ding, Z. Zhang, X. Chu, T. Shaymurat, C. Shao, Y. Liu, Up-Conversion Luminescence of $NaYF_4:Yb^{3+}/Er^{3+}$ Nanoparticles Embedded into PVP Nanotubes with Controllable Diameters, J. Phys. Chem. C. 116 (2012) 5787–5791.

[99] D. Li, X. Dong, W. Yu, J. Wang, G. Liu, Synthesis and upconversion luminescence properties of $YF_3:Yb^{3+}/Er^{3+}$ hollow nanofibers derived from $Y_2O_3:Yb^{3+}/Er^{3+}$ hollow nanofibers, J. Nanoparticle Res. 15 (2013) 1704 –1714.

[100] L. He, L. Feng, L. Cheng, Y. Liu, Z. Li, R. Peng, et al., Multilayer dual-polymer-coated upconversion nanoparticles for multimodal imaging and serum-enhanced gene delivery, ACS Appl. Mater. Interfaces. 5 (2013) 10381–10388.

[101] X. Li, Z. Hou, Y. Zhang, G. Zhang, J. Lian, J. Lin, New insight into modulated up-conversion luminescent silica nanotubes as efficient adsorbents for colored effluents., Dalton Trans. 43 (2014) 15457–64.

[102] Y. Chen, S. Liu, Z. Hou, P. Ma, D. Yang, C. Li, J. Lin, Multifunctional electrospinning composite fibers for orthotopic cancer treatment in vivo, Nano Res. 1 (2015) 1–15.

[103] N. Wiederkehr, The aggregation behavior of Zn tetracarboxy phthalocyanineand its spectral sensitization of titanium dioxide films, J. Braz. Chem. Soc. (1996).

[104] F. Wang, Y. Han, C.S. Lim, Y. Lu, J. Wang, J. Xu, H. Chen, C. Zhang, M. Hong, X. Liu, Simultaneous phase and size control of upconversion nanocrystals through lanthanide doping., Nature. 463 (2010) 1061–5.

[105] L. De Luca, G. Giacomelli, D. Chimica, V. Uni, An easy microwave-assisted synthesis of sulfonamides directly from sulfonic acids sulfonamides from sulfonic acids an easy and handy synthesis of sulfonamides directly from sulfonic acids or its sodium salts is reported . The reaction is performed under m, J. Org. Chemsitry. 73 (2008) 3967–3969.

[106] S. Sapra, D.D. Sarma, Simultaneous control of nanocrystal size and nanocrystal-nanocrystal separation in CdS nanocrystal assembly, Pramana - J. Phys. 65 (2005) 565–570.

[107] S. Fery-Forgues, D. Lavabre, Are fluorescence quantum yields so tricky to measure? A demonstration using familiar stationery products, J. Chem. Educ. 76 (1999) 1260.

[108] M. Idowu, T. Nyokong, Photophysical and photochemical properties of zinc and aluminum phthalocyanines in the presence of magnetic fluid, J. Photochem. Photobiol. A Chem. 188 (2007) 200–206.

[109] T. Tran-Thi, C. Desforge, C. Thiec, Singlet-Singlet and Triplet-Triplet intramolecular transfer processes in a covalently linked porphyrin-phthalocyanine heterodimer, J. Phys. Chem. 32 (1989) 290–296.

[110] M. Idowu, J.Y. Chen, T. Nyokong, Photoinduced energy transfer between water soluble CdTe Quantum Dots and Aluminium tetrasulfonated phthalocyanine, New J. Chem. 32 (2008) 290–296.

[111] G. Chen, H. Qiu, P.N. Prasad, X. Chen, Upconversion nanoparticles: Design, nanochemistry, and applications in Theranostics, Chem. Rev. 114 (2014) 5161–

5214.

[112] Y. Wu, X. Chu, Y. Cen, L. Huang, R. Yu, Upconversion fluorescence resonance energy transfer biosensor for sensitive detection of human immunodeficiency virus antibody in human serum, Chem. Commun. (2014) 4759–4762.

[113] A. Sedlmeier, H.H. Gorris, Chem Soc Rev Surface modification and characterization of photon-upconverting nanoparticles for bioanalytical applications, Chem. Soc. Rev. 44 (2014) 1526–1560.

[114] Z. Wang, S. Zheng, J. Yu, X. Ji, H. Zheng, S. Xin, Y. Wang, L. Sun, Size/morphology induced tunable luminescence in upconversion crystals: ultra-strong single-band emission and underlying mechanisms, Nanoscale, Press. (n.d.)

[115] J. Zhang, H. Tao, X. Zhao, Upconversion luminescence properties of Er^{3+} doped GeS_2-Ga_2S_3-KCl chalcohalide glasses, Rare Met. 30 (2011) 18–21.

[116] C.L. Takanishi, E. a. Bykova, W. Cheng, J. Zheng, GFP-based FRET analysis in live cells, Brain Res. 1091 (2006) 132–139.

[117] E. I Zenkevich, A.P. Stupak, D. Kowerko, C. Borczyskowski, Influence of single dye molecules on temperature and time dependent optical properties of CdSe/ZnS quantum dots: Ensemble and single nanoassembly detection, Chem. Phys. 406 (2012) 21–29.

[118] T. Blaudeck, E.I. Zenkevich, F. Cichos, C. Von Borczyskowski, Probing wave functions at semiconductor quantum-dot surfaces by non-FRET photoluminescence quenching, J. Phys. Chem. C. 112 (2008) 20251–20257.

[119] X.W. SUn, J. Chen, J.L. Song, D.W. Zhao, W. Deng, W. Lei, Ligand capping effect for dye solar cells with a CdSe quantum dot sensitizd ZnO nanorod photoanode, Opt. express1. 18 (2010) 1296–1301.

[120] B. Sikora, K. Fronc, I. Kaminska, K. Kopre, S. Szewczyk, B. Paterczyk, et al., Transport of $NaYF_4$:Er^{3+},Yb^{3+} up-converting nanoparticles into HeLa Cells, Nanotechnology. 24 (2013) 235702.

[121] M. Stillman, T. Nyokong, Phthalocyanines: Properties and Applications, in: C.. Leznoff, A.B.. Lever (Eds.), vol 1, VCH Publishers, New York, 1989: pp. 383–389.

[122] S. Senthilarasu, S. Velumani, R. Sathyamoorthy, a. Subbarayan, J. A. Ascencio, G. Canizal, P. J. Sebastian, J. a. Chavez, R. Perez, Characterization of zinc phthalocyanine (ZnPc) for photovoltaic applications, Appl. Phys. A Mater. Sci. Process. 77 (2003) 383–389.

[123] J.B. Lambert, H.F. Shurvell, D.A. Lightner, R.. Cooks, Introduction to Organic Spectroscopy, Macmillan, 1987.

[124] X. Cai, Y. Zhang, X. Zhang, J. Jiang, Structures and properties of 2,3,9,10,16,17,23,24-octasubstituted phthalocyaninato-lead complexes: The substitutional effect study on the basis of density functional theory calculations, J. Mol. Struct. THEOCHEM. 801 (2006) 71–80.

[125] B. Smith, Infrared Spectral Interpretation: A Systematic Approach, Second Edition, 2nd ed., CRC Press, 1998.

[126] M. Ben Haddada, J. Blanchard, S. Casale, J.-M. Krafft, A. Vallée, C. Méthivier, S. Boujday., Optimizing the immobilization of gold nanoparticles on functionalized silicon surfaces: amine- vs thiol-terminated silane, Gold Bull. 46 (2013) 335–341.

[127] J. Yu, M. Guan, F. Li, Z. Zhang, C. Wang, C. Shu, H. Wei, X. Zhang, Effects of fullerene derivatives on bioluminescence and application for protease detection., Chem. Commun. (Camb). 48 (2012) 11011–3.

[128] Z. Li, X. Huang, X. Zhang, L. Zhang, S. Lin, The synergistic effect of graphene and polyoxometalates enhanced electrocatalytic activities of Pt-{PEI-GNs/[PMo12O40]3−}n composite films regarding methanol oxidation, Journa Mater. Chem. 22 (2012) 23602–23607.

[129] Y. Liu, C. Tian, B. Yan, Q. Lu, Y. Xie, J. Chen, R. Gupta, Z. Xu, S. M. Kuznicki. Q. Liu, H. Zeng, Nanocomposites of graphene oxide, Ag nanoparticles, and magnetic ferrite nanoparticles for elemental mercury (Hg^0) removal, RSC Adv. 5 (2015) 15634–15640.

[130] C. Tao, J. Wang, S. Qin, Y. Lv, Y. Long, H. Zhua, Z. Jianga, Fabrication of pH-sensitive graphene oxide–drug supramolecular hydrogels as controlled release systems, J. Mater. Chem. (2012) 24856–24861.

[131] A. Dementjev, A. de Graaf, M. van de Sanden, K. Maslakov, A. Naumkin, A. Serov, X-Ray photoelectron spectroscopy reference data for identification of the C3N4 phase in carbon–nitrogen films, Diam. Relat. Mater. 9 (2000) 1904–1907.

[132] S. Christ, M. Schäferling, Chemical sensing and imaging based on photon upconverting nano- and microcrystals: a review, Methods Appl. Fluoresc. 3 (2015) 034004.

[133] T. Wu, D. Wilson, N.R. Branda, Fluorescent quenching of lanthanide-doped upconverting nanoparticles by photoresponsive polymer shells, Chem. Mater. 26 (2014) 4313–4320.